COPPE
Instituto Alberto Luiz Coimbra de Pós-Graduação e Pesquisa de Engenharia
UFRJ

FLOW ASSURANCE ANALYSIS: FLUID CHARACTERIZATION, VIRTUAL FLOW METERING, AND WAX PRECIPITATION

Maria Rosa Rocha Tenorio Goes

Tese de Doutorado apresentada ao Programa de Pós-graduação em Engenharia Química, COPPE, da Universidade Federal do Rio de Janeiro, como parte dos requisitos necessários à obtenção do título de Doutor em Engenharia Química.

Orientadores: Argimiro Resende Secchi
Frederico Wanderley Tavares

Rio de Janeiro

Fevereiro de 2023

FLOW ASSURANCE ANALYSIS: FLUID CHARACTERIZATION, VIRTUAL FLOW METERING, AND WAX PRECIPITATION

Maria Rosa Rocha Tenorio Goes

TESE SUBMETIDA AO CORPO DOCENTE DO INSTITUTO ALBERTO LUIZ COIMBRA DE PÓS-GRADUAÇÃO E PESQUISA DE ENGENHARIA (COPPE) DA UNIVERSIDADE FEDERAL DO RIO DE JANEIRO COMO PARTE DOS REQUISITOS NECESSÁRIOS PARA A OBTENÇÃO DO GRAU DE DOUTOR EM CIÊNCIAS EM ENGENHARIA QUÍMICA.

Orientadores: Argimiro Resende Secchi
Frederico Wanderley Tavares

Aprovada por: Prof. Frederico Wanderley Tavares, D.Sc.
Prof. Argimiro Resende Secchi, D.Sc.
Prof. Márcio Nele, D.Sc.
Prof. Paulo Couto, D.Sc.
Prof. Eduardo Rocha de Almeida Lima, D.Sc.

RIO DE JANEIRO, RJ – BRASIL

FEVEREIRO DE 2023

Goes, Maria Rosa Rocha Tenorio

Flow assurance analysis: fluid characterization, virtual flow metering, and wax precipitation/Maria Rosa Rocha Tenorio Goes. – Rio de Janeiro: UFRJ/COPPE, 2023.

XXIX, 137 p.: il.; 29, 7cm.

Orientadores: Argimiro Resende Secchi

Frederico Wanderley Tavares

Tese (doutorado) – UFRJ/COPPE/Programa de Engenharia Química, 2023.

Referências Bibliográficas: p. 80 – 88.

1. Flow assurance. 2. Offshore pipelines. 3. Multiphase flow. I. Secchi, Argimiro Resende *et al.* II. Universidade Federal do Rio de Janeiro, COPPE, Programa de Engenharia Química. III. Título.

To my father, Pedro Paulo Tenorio Goes (in memorian).

Acknowledgment

I would like to thank all the people who contributed to the progress of this work.

I am grateful for the patience and scientific contribution of my supervisors, Prof. Argimiro Secchi and Frederico Tavares. I will be eternally grateful.

This study was financed in part by the Coordenação de Aperfeiçoamento de Pessoal de Nível Superior - Brasil (CAPES) - Finance Code 001, Conselho Nacional de Pesquisas (CNPq) and Agência Nacional do Petróleo (ANP). We also thank Schlumberger and ESSS for providing the software OLGA® and ALFAsim®, respectively.

Resumo da Tese apresentada à COPPE/UFRJ como parte dos requisitos necessários para a obtenção do grau de Doutor em Ciências (D.Sc.)

ANÁLISE DE GARANTIA DE ESCOAMENTO: CARACTERIZAÇÃO DO FLUIDO, MEDIÇÃO VIRTUAL DA VAZÃO E PRECIPITAÇÃO DE PARAFINAS

Maria Rosa Rocha Tenorio Goes

Fevereiro/2023

Orientadores: Argimiro Resende Secchi
Frederico Wanderley Tavares

Programa: Engenharia Química

Na exploração de petróleo, existem inúmeros problemas relacionados à garantia de escoamento, como a precipitação e, consequente, deposição de parafinas que pode causar a obstrução das linhas de produção. Sabe-se que durante o escoamento do fluido, da cabeça do poço até os vasos separadores, a temperatura tende a cair, e quando a temperatura atinge a temperatura de início de aparecimento de ceras, as moléculas de parafina da mistura que estão em solução podem precipitar. Dentro deste contexto, neste trabalho são propostos procedimentos de análise da garantia de escoamento, especificamente dentro do contexto da precipitação de parafinas. Primeiro, uma análise da precipitação de parafinas durante o escoamento de um óleo hipotético em uma linha de produção de óleo e gás também hipotética é realizada. Em seguida, são propostos um método de medição de vazão virtual e uma melhoria no método de desagrupamento do óleo para que análises de garantia de escoamento possam ser realizadas em cenários reais. Por fim, é proposto um algoritmo iterativo para prever o comportamento do óleo durante o escoamento multifásico em linhas de produção offshore reais usando uma composição de fluido baseada nas propriedades de um óleo real. Esse trabalho propõe diretrizes para análise de garantia de escoamento e monitoria de fluido que podem ser aplicada a cenários reais. Adicionalmente, ao acoplar o modelo de escoamento multifásico e um algoritmo termodinâmico para precipitação de parafinas, é possível prever a seção da linha de produção onde inicia a deposição de parafinas.

Abstract of Thesis presented to COPPE/UFRJ as a partial fulfillment of the requirements for the degree of Doctor of Science (D.Sc.)

FLOW ASSURANCE ANALYSIS: FLUID CHARACTERIZATION, VIRTUAL FLOW METERING, AND WAX PRECIPITATION

Maria Rosa Rocha Tenorio Goes

February/2023

Advisors: Argimiro Resende Secchi
Frederico Wanderley Tavares

Department: Chemical Engineering

Petroleum exploitation generates numerous problems related to flow assurance, such as wax precipitation, which can cause the obstruction of the pipelines. It is known that during the fluid flow, from the wellhead to the separating vessels, the temperature tends to fall, and when the temperature reaches the wax appearance temperature, the components of the mixture may precipitate. Within this context, this work provides guidelines on flow assurance analysis, specifically on wax precipitation. First, a flow assurance analysis of wax precipitation in a hypothetical oil and gas production line is performed using a hypothetical oil composition. Then a virtual flow metering method and an improvement of the black oil delumping method are proposed to perform these analyses in real-case scenarios. Lastly, an iterative algorithm to predict the oil behavior during the multiphase flow in real offshore pipelines using a fluid composition based on black oil properties of a real oil is proposed. This works provide guidelines for flow assurance analysis and fluid flow monitoring that may be applied to real-case scenarios. Additionally, by coupling the multiphase flow modeling and a thermodynamic algorithm for wax precipitation, it is possible to predict the pipe section where the wax deposition begins.

Contents

Acknowledgment **v**

List of Figures **xii**

List of Tables **xv**

List of Symbols **xix**

List of Abbreviations **xxix**

1 Introduction **1**

1.1 Motivation and originality 3

1.2 Objectives 3

1.3 Text structure 4

2 Wax Appearance and Prevention in Two-Phase Flow using the Multi-Solid and Drift-Flux Model **6**

2.1 Introduction 7

2.2 Methodology 8

2.3 Results and Discussion 15

2.3.1 Validation of the Wax Precipitation Model. 15

2.3.2 Verification of the Drift-Flux Model 16

2.3.3 Case Studies 17

2.4 Partial Conclusions 22

3 Virtual Flow Metering of Oil Wells for a Pre-Salt Field 23

3.1 Introduction . . . 24

3.2 Method . . . 26

3.2.1 Determining the Valve Sizing Coefficient, C_v . . . 28

3.2.2 Determining the Real-Time Volumetric Flow Rates, Q_l and Q_g 35

3.3 Results and Discussion . . . 36

3.4 Partial Conclusions . . . 40

4 Improvement of Black Oil Delumping Method Applied to an Offshore Oil Field 42

4.1 Introduction . . . 42

4.2 Delumping Method . . . 44

4.3 Results and Discussion . . . 51

4.4 Partial Conclusions . . . 55

5 Multiphase Flow Simulation in Offshore Pipelines: An Accurate and Fast Algorithm Applied to Real-Field Data 56

5.1 Introduction . . . 56

5.2 Methodology . . . 59

5.2.1 Drift-Flux Model . . . 59

5.2.2 Two-Fluid Model . . . 61

5.2.3 Complementary Modeling . . . 62

5.3 Case Studies . . . 64

5.3.1 Model validation . . . 64

5.3.2 Case study - hypothetical gas and oil production pipeline . . . 64

5.3.3 Case study - real offshore gas and oil production pipeline . . . 66

5.4 Modeling with OLGA® and ALFAsim® . . . 68

5.5 Results and Discussion . . . 69

5.5.1 Model Validation . . . 69

5.5.2 Model application to an hypothetical oil pipeline 71
5.5.3 DFM simulation in a real offshore gas and oil production pipeline 74
5.6 Partial Conclusions 77

6 General Conclusions and Suggestions for Future Researches 78
6.1 Potential Future Researches 78

Bibliography 80

A Complementary Material 89

B Thermodynamic Modeling 94
B.1 Vapor-liquid Equilibrium (VLE) 94
B.2 Enthalpy 99
B.2.1 Enthalpy in the Ideal Gas State 99
B.2.2 Residual Enthalpy 101

C Physical Properties 103
C.1 Liquid Phase 103
C.1.1 Density 103
C.1.2 Viscosity 106
C.1.3 Superficial Tension 108
C.2 Vapor Phase 108
C.2.1 Density 109
C.2.2 Viscosity 109
C.2.3 Velocity 109
C.3 Mixture 110
C.3.1 Density 110
C.3.2 Enthalpy 110

D Drift-Flux Model Parameters 111

E Multiple Solid Solutions Model **114**

F Complementary Material **117**

G Supplementary Material **120**

List of Figures

2.1 Offshore oil production field where (T_0, P_0) and (T_e, P_e) are the inlet and outlet temperature and pressure of the pipeline, respectively. Adapted from NEMOTO *et al.* (2010). 12

2.2 Procedure to calculate the minimum inlet T such that no wax precipitation occurs during the fluid flow. 14

2.3 Procedure to verify in which section of the pipeline will occur wax precipitation if the initial conditions (T and P) favor this phenomenon. 14

2.4 Comparison between WAT calculation and experimental data from DAUPHIN *et al.* (1999) at 1 bar. 15

2.5 Comparison between WAT calculation and experimental data from RONNINGSEN *et al.* (1997) at 420 bar. 16

2.6 Comparison between the temperature profile in the pipeline obtained in this work with the simulation result from software OLGA. 17

2.7 Axial profile of (a) pressure and (b) temperature for the 4-components mixture flow in the pipeline. 18

2.8 WAT Calculation as function of pressure for the Cases 1, 2, 3, 4 e 5. . 19

2.9 WAT calculation during the fluid flow with T_0 equal to 311.15, 316.15, and 320.1 K. 20

2.10 Axial profile of (a) temperature and (b) mixture velocity. 21

3.1 Flow chart describing the (a) first and (b) second step of the method. 36

3.2 Comparison of total oil flow rate in different days of 2019. 37

3.3 Comparison of total gas flow rate in different days of 2019. 37

3.4 Comparison of total water flow rate in different days of 2019. 37

3.5 Total oil flow rate of a pre-salt plataform from November 1st at 5PM to November 2nd at 5PM at every second. 38

3.6 Total gas flow rate of a pre-salt plataform from November 1st at 5PM to November 2nd at 5PM at every second. 38

3.7 Individual gas flow rate of each well of a pre-salt plataform from November 1st at 5PM to November 2nd at 5PM at every second. . . 39

3.8 Percentual relative error between the predicted flow rates and the provided by fiscal meters, for a 24 hours period. 40

4.1 Proposed black oil delumping method. 48

4.2 Black oil delumping method proposed by HODA and WHITSON (2013). 49

4.3 Black oil delumping method proposed by HODA *et al.* (2017). 50

4.4 Flowchart of the offshore oil production field. 50

4.5 Comparison of γ_g for Wells 1, 2, and 3: measured vs. calculated using the method proposed in this work. 53

4.6 Comparison of GOR for Wells 1, 2, and 3: measured vs. calculated using the method proposed in this work. 54

4.7 Comparison of $^{\circ}API$ for Wells 1, 2, and 3: measured vs. calculated using the method proposed in this work. 54

5.1 Schematic of the hypothetical offshore oil pipeline. 64

5.2 Pipeline geometry. 66

5.3 Flowchart of the iterative algorithm proposed to first characterize the oil and then to fit a multiphase flow model to measured data from offshore oil field. The pipe wall roughness was used as the fitting parameter. 68

5.4 Vapor void fraction as a function of the vapor superficial velocities at (a) $\langle j_l \rangle = 0.1074\ m/s$ and $\theta = 50^{\circ}$, (b) $\langle j_l \rangle = 2.2311\ m/s$ and $\theta = 0^{\circ}$, and (c) $\langle j_l \rangle = 0.3139\ m/s$ and $\theta = 90^{\circ}$ for the kerosene as the liquid phase. 70

5.5 Vapor void fraction as a function of the vapor superficial velocities at (a) $\langle j_l \rangle = 0.1097\ m/s$ and $\theta = 0^{\circ}$ for the lube oil as the liquid phase. 70

5.6 Axial profile of (a) temperature and (b) pressure. 72

5.7 Axial profile of (a) liquid and (b) gas densities. 72

5.8 Axial profile of (a) liquid and (b) gas viscosities. 72

5.9 Axial profile of vapor void fraction. 72

5.10 Comparison of the axial temperature and pressure profile calculated by DFM and software OLGA®, and the data measured in real time for Well (a) 1 and (b) 2. 74

5.11 Comparison of the axial temperature and pressure profile calculated by DFM and software OLGA®, and the data measured in real time for Wells (a) 1 and (b) 2 using the optimum wall roughness. 76

List of Tables

2.1 Material properties and dimensions of the pipeline. 10

2.2 Physical properties of the fluid. 11

2.3 Physical properties of the pure components. 11

2.4 Physical properties of the pseudocomponent. 12

2.5 Pure component properties for the fluid given in WHITSON and BRULÉ (2000) (MULTIFLASH, 2014). 13

2.6 Global composition of the mixture and operational data. 18

2.7 Global composition of the 4-component mixtures for the Cases 1, 2, 3, 4 e 5. 19

2.8 Operational data for fluid flow simulations. 20

2.9 Operational data to analyze the effect of inlet flow rate. 21

3.1 Statistical summary of the input data describing the minimum, maximum and mean values of the input variables. 27

4.1 Correlations for pseudocomponent properties 46

4.2 Volume-shift parameter of the pure components (WHITSON and BRULÉ, 2000) 47

4.3 PRE for the results of Well 1 using the method presented in HODA and WHITSON (2013) and HODA *et al.* (2017) when calculating $M_{C_{11+}}$ using the correlation given by STANDING (1974), and the method proposed in this work 51

4.4 PRE for the results of Well 2 using the method presented in HODA and WHITSON (2013) and HODA *et al.* (2017) when calculating $M_{C_{11+}}$ using the correlation given by STANDING (1974), and the method proposed in this work 52

4.5 PRE for the results of Well 3 using the method presented in HODA and WHITSON (2013) and HODA *et al.* (2017) when calculating $M_{C_{11+}}$ using the correlation given by STANDING (1974), and the method proposed in this work 52

5.1 Pipeline geometry. 65

5.2 Pipeline section dimensions. 65

5.3 Pipeline material properties. 65

5.4 U_{heat} of the pipeline sections. 65

5.5 Mass flow rate produced by Wells 1 and 2. 67

5.6 MPRE between the experimental and calculated vapor void fraction for the models and softwares. 71

5.7 Measured CPU time of simulation 73

5.8 Comparison between real time data and calculated values at wellhead and inlet of the choke valve. 75

5.9 Comparison between real time data and calculated values at wellhead and inlet of the choke valve using the optimum wall roughness. 76

5.10 Optimum wall roughness for Wells 1 and 2. 76

A.1 Global composition of the mixtures available in DAUPHIN *et al.* (1999). 90

A.2 Global composition of the mixture (Oil 10) available in RONNINGSEN *et al.* (1997). 91

A.3 Physical properties of the pseudocomponent from "Oil 10" available in RONNINGSEN *et al.* (1997). 91

A.4 Global composition of the mixture ("Oil 11") available in RONNINGSEN *et al.* (1997). 92

A.5 Physical properties of the pseudocomponent from "Oil 11" available in RONNINGSEN *et al.* (1997). 92

A.6 Global composition of the mixture available in WHITSON and BRULÉ (2000). 92

A.7 Physical properties of the pseudocomponent from volate oil available in WHITSON and BRULÉ (2000). 93

B.1 EOS PR parameters. 96

B.2 Binary interaction parameter (k_{ij}). 97

B.3 Binary interaction parameter (k_{ij}). 97

B.4 Parameters to calculate the enthalpy in the ideal gas state. 100

C.1 Values of the parameters 104

F.1 Global composition of the volate oil adapted from WHITSON and BRULÉ (2000) and pure component properties. 117

F.2 Global composition of the oil obtained from GÓES *et al.* (2022) and its pure component properties. 118

F.3 Dimensions and thermal properties of Well 1 for the real offshore gas and oil production pipeline. 118

G.1 Data given in the Well Test Reports of Well 1. 120

G.2 Data given in the Gas Chromatographic Analysis of Well 1. 121

G.3 Initial estimate for the wellstream composition of the mixture when using correlation given by LASATER (1958) for calculating $M_{C_{11+}}$ of Well 1. 122

G.4 Molar mass of the mixture components when using correlation given by LASATER (1958) for calculating $M_{C_{11+}}$ of Well 1. 123

G.5 Initial estimate for the wellstream composition of the mixture when using correlation given by STANDING (1974) for calculating $M_{C_{11+}}$ of Well 1. 124

G.6 Molar mass of the mixture components when using correlation given by STANDING (1974) for calculating $M_{C_{11+}}$ of Well 1. 125

G.7 Wellstream composition of the mixture when using correlation proposed by LASATER (1958) for calculating $M_{C_{11+}}$ of Well 1 given by HODA and WHITSON's method 126

G.8 Wellstream composition of the mixture when using correlation proposed by STANDING (1974) for calculating $M_{C_{11+}}$ of Well 1 given by HODA and WHITSON's method 127

G.9 Wellstream composition of the mixture when using correlation proposed by LASATER (1958) for calculating $M_{C_{11+}}$ of Well 1 given by HODA *et al.*'s method after applying the Gamma Distribution Function 128

G.10 Mass molar of the components when using correlation proposed by LASATER (1958) for calculating $M_{C_{11+}}$ of Well 1 given by HODA *et al.*'s method after applying the Gamma Distribution Function . . . 129

G.11 Final wellstream composition of the mixture when using correlation proposed by LASATER (1958) for calculating $M_{C_{11+}}$ of Well 1 given by HODA *et al.*'s method 130

G.12 Wellstream composition of the mixture when using correlation proposed by STANDING (1974) for calculating $M_{C_{11+}}$ of Well 1 given by HODA *et al.*'s method after applying the Gamma Distribution Function 131

G.13 Mass molar of the components when using correlation proposed by STANDING (1974) for calculating $M_{C_{11+}}$ of Well 1 given by HODA *et al.*'s method after applying the Gamma Distribution Function . . . 132

G.14 Final wellstream composition of the mixture when using correlation proposed by STANDING (1974) for calculating $M_{C_{11+}}$ of Well 1 given by HODA *et al.*'s method 133

G.15 PRE for the results of Well 1 using the method proposed in HODA and WHITSON (2013) and HODA *et al.* (2017) when calculating $M_{C_{11+}}$ given by LASATER (1958) 134

G.16 Optimum initial wellstream composition of the mixture of Well 1 predicted using the method proposed in this work 135

G.17 Final wellstream composition of the mixture of Well 1 calculated using the method proposed in this work 136

G.18 Molar mass of the components calculated using the method proposed in this work 137

List of Symbols

Chapter 1

$^{\circ}API$	degree API [-]
ρ_{oil}	oil density $[kg/m^3]$
ρ_{water}	water density $[kg/m^3]$

Chapter 2

w	acentric factor [-]
w_{SRK}	acentric factor calculated using the EOS SRK [-]
ω_i	acentric factor of component i [-]
ω_j	acentric factor of component j [-]
$w_{SRK\,m}$	acentric factor of the mixture [-]
$(w)_{C+}$	acentric factor of the pseudocomponent [-]
k_{ij}	binary interaction parameter between components i and j [-]
V°	characteristic volume [-]
$V_m{}^{\circ}$	characteristic volume of the mixture [-]
$(V^{\circ})_{C+}$	characteristic volume of the pseudocomponent $[m^3/kg]$
Z	compressibility factor [-]
Z_f	compressibility factor of phase f [-]
$Z_{RA\,m}$	compressibility factor of the mixture [-]
Z_{RA}	compressibility factor of the modified Rackett equation [-]
R	constant of real gases $[J/(mol\,K)]$
h_{viz}	convective heat transfer coefficient of the neighborhood $[W/(m^2\,K)]$
V_i°	COSTALD characteristic volume of component i [-]
V_j°	COSTALD characteristic volume of component j [-]
P_c	critical pressure $[Pa]$

P_{ci}	critical pressure of component i $[Pa]$
P_{cj}	critical pressure of component j $[Pa]$
P_{cl}	critical pressure of the liquid phase $[Pa]$
P_{cm}	critical pressure of the mixture $[Pa]$
$(P_c)_{C+}$	critical pressure of the pseudocomponent $[Pa]$
T_c	critical temperature $[K]$
T_{ci}	critical temperature of component i $[K]$
T_{cj}	critical temperature of component j $[K]$
T_{cl}	critical temperature of the liquid phase $[K]$
T_{cm}	critical temperature of the mixture $[K]$
$(T_c)_{C+}$	critical temperature of the pseudocomponent $[K]$
V_c	critical volume $[m^3/kg]$
V_{ci}	critical volume of the component i $[m^3/kg]$
V_{cl}	critical volume of the liquid phase $[m^3/kg]$
$(V_c)_{C+}$	critical volume of the pseudocomponent $[m^3/kg]$
$V_{cC_{7+}}$	critical volume of the pseudocomponent $[m^3/kg]$
A	cross-sectional area $[m^2]$
ρ^L	density of liquid phase $[kg/m^3]$
ρ^m	density of mixture $[kg/m^3]$
ρ^k	density of phase k $[kg/m^3]$
$\rho_{C_{7+}}$	density of the pseudocomponent $[kg/m^3]$
ρ_{H_2O}	density of the water $[kg/m^3]$
ρ^V	density of vapor phase $[kg/m^3]$
$\left\langle \hat{v}_v^{des} \right\rangle_\alpha$	drift-flux model parameter $[m/s]$
C_0	drift-flux model parameter [-]
h	enthalpy $[J/mol]$
h_f^{gi}	enthalpy in the ideal gas state of phase f $[J/mol]$
$h_{fC_{7+}}^{gi}$	enthalpy of pseudocomponent in phase f in the ideal gas state $[J/mol]$
a_i, α_i, and b_i	EOS PR mixture parameters of component i [-]
u_1 and u_2	EOS PR parameters [-]
a_j and b_j	EOS PR parameters of component j [-]
A_f and B_f	EOS PR parameters of phase f [-]
β_{new}	estimate for the value of β [-]
F_{mw}	frictional loss of pressure $[kg/(m^2\, s^2)]$
$\phi_{i\,pure}^L$	fugacity coefficient of pure component i in the liquid phase [Pa]
ϕ_{fi}	fugacity coefficient of the component i in phase f [-]

ϕ_{li}	fugacity coefficient of the component i in the liquid phase [-]
ϕ_{vi}	fugacity coefficient of the component i in the vapor phase [-]
f_i^L	fugacity of component i in the liquid phase [Pa]
$f_{i\,pure}^S$	fugacity of pure component i in the solid phase [Pa]
$f_{i\,pure}^L$	fugacity of pure component i in the solid phase [Pa]
z_i	global molar composition of the component i [-]
g	gravity of earth $[m/s^2]$
C_{pfi}	heat capacity of component i of phase f $[J/mol]$
$\dot{Q}_{tw}$	heat exchange rate $[W/m^3]$
A_v^R	Helmholtz residual energy of phase f $[J/mol]$
θ	inclination angle of the pipeline [degree]
$K_i^{initial}$	initial estimate of the equilibrium constant of the component i [-]
P_e	inlet pressure [Pa]
T_e	inlet temperature [K]
D_{int}	inner diameter of the pipe [m]
h^L	liquid enthalpy $[J/mol]$
W^L	liquid mass flow rate $[kg/(m^2\,s)]$
μ_{ol}	liquid mixture viscosity at atmospheric pressure $[Pa.s]$
α^L	liquid void fraction [-]
G^k	mass flow of phase k $[kg/s]$
G^V	mass flow of vapor phase $[kg/s]$
h^m	mixture enthalpy $[J/mol]$
a_f^{mist} and b_f^{mist}	mixture EOS PR parameters in phase f [-]
$\langle j \rangle$	mixture superficial velocity $[m/s]$
v^m	mixture velocity $[m/s]$
ϵ_m	mixture viscosity parameter in the liquid phase $[K^{1/6}/\sqrt{g/mol}/Pa^{2/3}]$
ϵ_i	mixture viscosity parameter of component i $[K^{1/6}/\sqrt{g/mol}/Pa^{2/3}]$
$phase_{C_{7+}}$	molar composition of the pseudocomponent in the liquid or vapor phase [-]
Δh_i^f	molar enthalpy of fusion of component i $[J/mol]$
x_i	molar fraction of component i in the liquid phase [-]
y_i	molar fraction of component i in the vapor phase [-]
x_i^L	molar fraction of component i in vapor phase [-]
$phase_i$	molar fraction of the component i in phase f [-]
$phase_j$	molar fraction of the component j in phase f [-]
MM	molar mass $[kg/mol]$

MM_i	molar mass of component i $[kg/mol]$
MM_l	molar mass of the liquid phase $[kg/mol]$
$MM_{C_{7+}}$	molar mass of the pseudocomponent $[g/mol]$
MM_v	molar mass of the vapor phase $[kg/mol]$
V	molar volume $[m^3/mol]$
T_{viz}	neighborhood temperature [K]
K_i^{new}	new estimate for the equilibrium constant [-]
D_{out}	outer diameter of the pipe [m]
D_{iso}	outer diameter plus isolation thickness of the pipe [m]
P_0	outlet pressure [Pa]
T_0	outlet temperature [K]
U_{heat}	overall heat transfer global coefficient $[W/(m^2\,^\circ C)]$
$Parachor$	Parachor number [-]
PAR_i	Parachor value of component i [-]
$(P_{ch})_{C+}$	parachor value of the pseudocomponent $[m^3/kg]$
$P_{rm}^{(1)}$ and $P_{rm}^{(0)}$	parameters used to calculate the mixture density in the liquid phase [-]
$\hat{\alpha}$ and $\hat{\beta}$	parameters used to calculate the mixture density in the liquid phase [-]
K, X, and Y	Parameters used to calculate the viscosity of the vapor phase [-]
A_i, B_i, C_i, D_i, and E_i	parametes to calculate the enthalpy of each phase [-]
x	pipeline length [m]
P	pressure [Pa]
P_i^f	pressure of fusion [Pa]
ρ_{rl}	reduced density of the liquid phase [-]
T_{ri}	reduced temperature of component i [-]
T_{rm}	reduced temperature of the mixture [-]
T_0	reference temperature $[^\circ R]$
h_f^R	residual enthalpy of phase f $[J/mol]$
s_v^R	residual entropy of phase f $[J/mol/K]$
V_{sat_m}	saturation volume of the liquid mixture $[m^3/mol]$
v_v^{des}	slip velocity of vapor phase $[m/s]$
σ_l	surface tension of the liquid phase $[kg/s^2]$
T	temperature [K]
T_i^f	temperature of fusion [K]
k_i	thermal conductivity of the isolation $[W/(m\,K)]$

k_t	thermal conductivity of the pipe $[W/(m\,K)]$
Δh_i^{tr}	transition molar enthalpy of component i in the solid phase $[J/mol]$
T_i^{tr}	transition temperature of component i in the solid phase [K]
$\hat{a}$, $\hat{b}$, $\hat{d}$, $\hat{f}$, $\hat{g}$, $\hat{h}$, $\hat{j}$, and $\hat{k}$	values of the parameters to calculate the liquid phase density [-]
h^V	vapor enthalpy $[J/mol]$
W^V	vapor mass flow rate $[kg/(m^2\,s)]$
Γ^V	vapor mass transfer rate $[kg/(m^2\,s)]$
P_{sm}	vapor pressure of the mixture $[Pa]$
α^V	vapor void fraction [-]
β_W	vaporized mass fraction [-]
β	vaporized molar fraction [-]
Δc_{Pi}	variation of heat capacity $[J/(kg\,K)]$
Δv_i	variation of molar volume $[m^3/mol]$
v^k	velocity of phase k $[m/s]$
μ_{oi}	viscosity of component i at atmospheric pressure $[Pa.s]$
μ_l	viscosity of the liquid phase$[Pa.s]$
μ_v	viscosity of the vapór phase $[Pa.s]$
α^k	void fraction of phase k [-]
Fr_{sg}	Froude number [-]
$\langle j_m \rangle$	mixture superficial velocity $[m/s]$
$C_{0,1}$	Parameter used to calculate the parameters of the Drift-Flux Model [-]
Re_{tp}	Reynolds Number of the two-phase fluid [-]
$\langle j_l \rangle$	superficial velocities of the liquid phase $[m/s]$
$\langle j_v \rangle$	superficial velocities of the vapor phase $[m/s]$
χ_{tp}	two phase flow quality [-]
f_{tp}	two phase friction factor [-]
La	variable used to calculate the parameters of the Drift-Flux Model [-]
C_2, C_3, and C_4	variables used to calculate the parameters of the Drift-Flux Model [-]
β_{tp}	volumetric flow fraction of the vapor phase [-]

Chapter 3

P_{us}	upstream pressure $[kPa]$
P_{ds}	downstream pressure $[kPa]$
T_{us}	upstream temperature $[K]$
Q_{gi}	gas lift injection flow rate $[m^3/d]$
u	choke valve opening percentage [-]
ρ_w^{SC}	water density at standard conditions $[kg/m^3]$
P^{SC}	standard condition of pressure $[kPa]$
T^{SC}	standard condition of temperature $[K]$
M_{air}	air molar mass $[kg/kmol]$
R	constant of real gases $[J/\,(kmol\,K)]$
γ_{wf}	produced water specific gravity [-]
GOR	gas oil ratio at standard conditions $[Nm^3/Nm^3]$
γ_o	oil specific gravity [-]
BSW	water cut at standard conditions [-]
M_g	gas molar mass $[kg/kmol]$
C_v	valve sizing coefficient $[gpm]$
W_m	mass flow rate $[kg/d]$
F_c	correction factor [-]
ρ_m	mixture density $[kg/m^3]$
W_g	gas mass flow rate $[kg/d]$
W_l	liquid mass flow rate $[kg/d]$
V_m	volumetric flow rate $[m^3/d]$
V_g	gas volumetric flow rate $[m^3/d]$
V_l	liquid volumetric flow rate $[m^3/d]$
Q_g^{SC}	gas volumetric flow rate at standard conditions $[Nm^3/d]$
ρ_g^{SC}	gas density at standard conditions $[kg/m^3]$
Q_{gi}^{SC}	gas lift injection flow rate at standard conditions $[Nm^3/d]$
Q_o^{SC}	oil mass flow rate at standard conditions $[Nm^3/d]$
Rs	gas solubility ratio [-]
B_g	gas formation volume factor $[m^3/Nm^3]$
γ_g	gas specific gravity [-]
ρ_w	water density $[kg/m^3]$
ρ_g	gas density $[kg/m^3]$
ρ_g^{SC}	gas density at standard conditions $[kg/m^3]$
ρ_{air}^{SC}	air density at standard conditions $[kg/m^3]$
Y	gas expansion factor [-]
ΔP	pressure drop across the choke valve $[kPa]$
W_o	oil mass flow rate $[kg/d]$

W_w	water mass flow rate $[kg/d]$
Q_w^{SC}	water volumetric flow rate at standard conditions $[Nm^3/d]$
ρ_o^{SC}	oil density at standard conditions $[kg/m^3]$
Q_l^{SC}	liquid volumetric flow rate at standard conditions $[Nm^3/d]$
Q_l	liquid volumetric flow rate $[m^3/d]$
B_w	water formation volume factor $[m^3/Nm^3]$
B_o	oil formation volume factor $[m^3/Nm^3]$
c_w	water compressibility $[kPa^{-1}]$
P_b	bubble point pressure $[kPa]$
ΔW_T and ΔW_P	parameters used to calculate B_w [-]
y_g	gas mole fraction [-]
M_o	oil mass molar $[kg/kmol]$
c_o	oil compressibility $[kPa^{-1}]$
API	degree API of the oil [-]
X_{co}	parameter used to calculate c_o [-]
ρ_l	liquid density $[kg/m^3]$
WC	water cut [-]
ρ_o	oil density $[kg/m^3]$
ρ_{ob}	oil density at bubble point $[kg/m^3]$
A_{cw}, B_{cw} and C_{cw}	parameters used to calculate c_w [-]
P_{us}^{rt}	pressure measured in real time $[kPa]$
P_{us}^{test}	pressure provided in the production test $[kPa]$

Chapter 4

API	degree API of the oil [-]
b_i	EOS pure component constant component i [-]
B_o	oil formation volume factor $[m^3/Sm^3]$
F	mixture flow rate $[kg/m^3]$
GOR	gas-oil ratio at standard conditions $[Nm^3/Nm^3]$
L	liquid stream flow rate $[kg/m^3]$
$M_{C_{11+}}$	average molar mass of the pseudocomponents $[g/mol]$
$M_{C_{11+i}}$	molar mass composition of the pseudocomponent i $[g/mol]$
M_i	molar mass of component i $[g/mol]$
N	number of components [-]

N_p	number of pseudocomponents [-]
n_i	molar flowrate of component i $[mol/d]$
n_{gi}	molar flowrate of component i in gas phase $[mol/d]$
n_{oi}	molar flowrate of component i in oil phase $[mol/d]$
$P^{ci}_{C_{11+}}$	critical pressure of the pseudocomponent i $[Pa]$
P^{SC}	standard pressure $[kPa]$
Q_g^{SC}	gas volumetric flowrate at standard conditions $[Nm^3/d]$
Q_o^{SC}	oil volumetric flowrate at standard conditions $[m^3/d]$
s_i	volume-shift parameter of component i [-]
$T^{bi}_{C_{11+}}$	boiling temperature of the pseudocomponent i $[K]$
$T^{ci}_{C_{11+}}$	critical temperature of the pseudocomponent i $[K]$
T^{SC}	standard temperature $[K]$
V	vapor stream flow rate $[kg/m^3]$
v_i	vapor composition of component i [-]
$v^{ci}_{C_{11+}}$	critical volume of the pseudocomponent i $[m^3/kg]$
v_g^{SC}	gas molar volume at standard conditions $[Nm^3/mol]$
v_o^{SC}	oil molar volume at standard conditions $[m^3/mol]$
v_o^{EOS}	oil molar volume calculated by the EOS model $[m^3/mol]$
x_i	molar fraction of component i in oil phase [-]
x_i	liquid composition of component i [-]
x_i^{SC}	molar fraction of component i in oil phase at standard conditions [-]
y_i^{SC}	molar fraction of component i in gas phase at standard conditions [-]
z_i	global molar composition of component i [-]
$z_{C_{11+i}}$	molar composition of the pseudocomponent i [-]
α_o^{SC}	oil molar fraction at standard conditions [-]
α_g^{SC}	gas molar fraction at standard conditions [-]
β	Gamma-Distribution Function parameter [-]
γ_g	gas specific gravity [-]
η	Gamma Distribution Function parameter [-]
$\omega^i_{C_{11+}}$	acentric factor of the pseudocomponent i [-]
Ω_i^{pred}	predicted value of the variable Ω in the Well Test Report i [-]
Ω_i^{meas}	measured value of the variable Ω in the Well Test Report i [-]
λ	Gamma-Distribution Function parameter [-]
ρ_{air}^{SC}	air density at standard conditions $[kg/m^3]$
ρ_g^{SC}	gas density at standard conditions $[kg/m^3]$
ρ_o^{SC}	oil density at standard conditions $[kg/m^3]$

ρ_w^{SC}	water density at standard conditions $[kg/m^3]$
Γ	Gamma Distribution Function [-]

Chapter 5

C_0	drift-flux model parameter [-]
F_i	frictional and interfacial drag force $[kg/(m^2\,s^2)]$
F_{MV}	virtual mass force $[kg/(m^2\,s^2)]$
F_{lw}	friction volumetric force of liquid phase $[kg/m^2/s^2]$
F_{mw}	frictional loss of pressure $[kg/(m^2\,s^2)]$
F_{vw}	friction volumetric force of vapor phase $[kg/m^2/s^2]$
g	gravity of earth $[m/s^2]$
h_l	liquid enthalpy $[J/mol]$
h_m	mixture enthalpy $[J/mol]$
h_v	vapor enthalpy $[J/mol]$
ID	inner diameter of the pipe [m]
$\langle j \rangle$	mixture superficial velocity $[m/s]$
MM	molar mass $[kg/mol]$
n	number of experiments [-]
P	pressure [Pa]
P_c	critical pressure $[Pa]$
P_{calc}^{wh}	pressure calculated by the DFM at the wellhead [bar]
P_{ch}	Parachor value $[-]$
P_e	inlet pressure [Pa]
P_{exp}^{wh}	pressure collected in real time at the wellhead [bar]
P_0	outlet pressure [Pa]
Q_{lw}	heat exchange with the liquid phase $[W/m^3]$
$\dot{Q}_{tw}$	heat exchange rate $[W/m^3]$
Q_{vw}	heat exchange with the vapor phase $[W/m^3]$
T	temperature [K]
T_c	critical temperature $[K]$
T_{calc}^{choke}	temperature calculated by the DFM at the inlet of the choke valve [K]
T_e	inlet temperature [K]
T_{calc}^{choke}	temperature collected in real time at the inlet of the choke valve [K]
T_{neigh}	neighborhood temperature [K]

T_0	outlet temperature [K]
U_{heat}	overall heat transfer global coefficient $[W/(m^2\,^\circ C)]$
V_c	critical volume $[m^3/kg]$
v_i	interfacial velocity $[m/s]$
v_l	velocity of liquid phase $[m/s]$
v_{li}	liquid interfacial velocity $[m/s]$
v_m	mixture velocity $[m/s]$
v_v	velocity of vapor phase $[m/s]$
v_v^{dft}	slip velocity of vapor phase $[m/s]$
$\left\langle \hat{v}_v^{dft} \right\rangle_\alpha$	drift-flux model parameter $[m/s]$
v_{vi}	vapor interfacial velocity $[m/s]$
x	pipeline length [m]
w	acentric factor $[-]$
W_l	liquid mass flow rate $[kg/s]$
W_l	vapor mass flow rate $[kg/s]$
α_i^{exp}	experimental value of experiment i [-]
α_i^{calc}	calculated value of experiment i [-]
α_l	liquid void fraction [-]
α_v	vapor void fraction [-]
γ_l	fraction of the heat exchange with the liquid phase [-]
γ_v	fraction of the heat exchange with the vapor phase [-]
Γ_l	liquid mass transfer rate $[kg/(m^2\,s)]$
Γ_v	vapor mass transfer rate $[kg/(m^2\,s)]$
β_w	vaporized mass fraction [-]
ρ_l	density of liquid phase $[kg/m^3]$
ρ_v	density of vapor phase $[kg/m^3]$
ρ_m	density of mixture $[kg/m^3]$
θ	inclination angle of the pipeline [degree]

List of Abbreviations

EM	Equilibrium Model, p. 79
FMT	Film Mass Transfer Theory, p. 79
DAE	differential-algebraic equations, p. 11
DFM	Drift-Flux Model, p. 3
EOS PR	cubic equation of state Peng-Robinson, p. 94
TFM	Two Fluid Model, p. 3
VLE	vapor-liquid equilibrium, p. 94
WAT	Wax appearance temperature, p. 2

Chapter 1

Introduction

Petroleum is flammable and less dense than water, with a particular smell and color ranging from black to light brown. Hydrocarbons basically constitute this mixture of chemical compounds. The other constituents appear as organic compounds that contain different chemical elements, such as nitrogen, sulfur, and oxygen. In a few cases, there is also the presence of salts of organic acids (THOMAS, 2001).

Hydrocarbons present hydrogen and carbon in their chemical structure and are classified according to the organization of these components. THOMAS (2001) cites that petroleum can be divided into five groups: normal, branched, cyclic, unsaturated, and aromatic paraffin.

An arbitrary scale created by the American Institute of Petroleum classifies the oil according to its degree API as a function of the oil density. On this scale, the higher the value of the $^{\circ}API$, the lighter the oil. The API degree is calculated according to Eq. 1.1.

$$^{\circ}API = \frac{141.5}{\rho_{oil}/\rho_{water}} - 131.5 \tag{1.1}$$

There is a term in the oil industry called flow assurance, first used by the Brazilian oil company Petrobras in the early 1990s, which refers to a set of strategies that assure oil production without interruption (VALENTE *et al.*, 2022). One of the main problems is the wax precipitation and consequent deposition on the pipeline wall, which can cause, in extreme cases, total pipeline obstruction. In these cases, the oil companies may choose to remove the obstructed pipe section, but the economic loss of the downtime process[1] and section removal can cost up to 30 million dollars

[1]Time interval during which an item is in a non-working state.

(VENKATESAN, 2004).

In certain cases, it is necessary to use mitigation methods to deal with this problem. For example, the British company Lasmo had to abandon an oil platform, which cost 100 million dollars, due to the recurring problem of wax precipitation (SINGH *et al.*, 2000). For cases like this to be avoided, models need to predict this phenomenon, so prevention methods can be applied at a suitable time.

According to PEDERSEN *et al.* (1991), the solid phase formed during oil production is mainly composed of normal paraffin molecules. Iso-paraffins, naphthas, and aromatics compounds do not precipitate in a mixture free of asphaltenes and water. Paraffinic hydrocarbons are also called alkanes, whose chemical formula is C_nH_{2n+2}.

Thermodynamic models were developed to predict the wax appearance temperature (WAT) and solubility curve using temperature, pressure, and fluid composition as input data. In the literature, three models can predict the formation of solid phases: Solid Solution, Multisolid, and Multiple Solid Solutions. The Solid Solution Model was first proposed by WON (1986) and is based on the theory that the paraffin molecules precipitate, forming a single homogeneous solid phase. LIRA-GALEANA *et al.* (1996) stated that the Multisolid Model predicts the formation of multiple solid phases, each composed of one pure component. The Multiple Solid Solutions Model, proposed by COUTINHO (1998), is based on the theory that the paraffin molecules precipitate, forming multiple solid solutions. This last model is accurate and comprehensive according to the deviations between experimental and calculated WAT and solubility curves presented by SILVA *et al.* (2017).

After the wax precipitation, the paraffin molecules may deposit on the pipeline wall if two conditions are satisfied: 1) the pipe wall temperature is below the WAT and 2) a negative radial temperature gradient is present (SVENDSEN, 1993). According to HUANG *et al.* (2015), the paraffin molecules begin to deposit on the pipe wall through the molecular diffusion mechanism. As a transient process, the wax growth depends on the radial diffusion of the wax particles dissolved in the bulk oil phase. These authors state that the growth process is initially fast and reaches a steady state.

In addition to the wax deposition models, it is necessary to predict the pressure and temperature profiles of the fluid inside the pipeline, given by hydrodynamic models. The most well-known hydrodynamic models in the literature are the Drift-Flux Model (DFM) and Two Fluid Model (TFM) (BEGGS and BRILL, 1973; HIBIKI and ISHII, 2003). According to TEIXEIRA and SECCHI (2017), these models predicted with satisfactory accuracy the fluid behavior when compared with

experimental data, the former having a lower computational cost.

There are mitigation and prevention methods to deal with the wax precipitation and, consequently, deposition. The most effective way to deal with this phenomenon is to avoid it by applying prevention methods, for example, insulation material along the pipeline to keep the temperature above the WAT. Prevention methods have limited effectiveness, so mitigation methods such as pigging and induction heating have significance. Generally, the latter is used to remove wax deposits stuck on the pipe wall, as pigging is less economically feasible (AIYEJINA *et al.*, 2011).

1.1 Motivation and originality

There is a lack of work on coupling thermodynamic and multiphase flow modeling in the literature. The papers found in the literature discuss either thermodynamic models (COUTINHO *et al.* (2006); LIRA-GALEANA *et al.* (1996); SILVA *et al.* (2017); WON (1986)) or multiphase flow modeling (ISHII and HIBIKI (2011); TEIXEIRA and SECCHI (2017)). Another gap in the literature is the application of those models to real-case scenarios, which is one of the main contributions of this work. Regarding fluid flow monitoring, the pressure and temperature sensors, in real scenarios, are installed at a few locations in the pipeline, for example, the wellhead and upstream choke. So it is important to predict in detail the pressure and temperature profiles inside a production line to perform flow assurance analysis. Besides it, a thermodynamic model coupled to the multiphase flow model would be essential to predict solid formation under real-case scenarios.

1.2 Objectives

In this context, this work aims to provide flow assurance analysis procedures, specifically on wax precipitation. By coupling the multiphase flow and thermodynamics, it is possible to predict what pipe section wax may form as solid phase, for example, in offshore pipelines. Moreover, with the proposed procedures, it is possible to simulate different flow scenarios and insulation setups to analyze their effect on the wax appearance temperature.

The specific objectives of this work are:

1. Provide a procedure to calculate a minimum inlet temperature to avoid wax

precipitation in a hypothetical oil and gas production line performed using a hypothetical oil composition;

2. Develop a methodology to predict the individual liquid and gas flow rates of each well;

3. Propose a method to convert black oil data into compositional wellstream;

4. Propose an algorithm to predict pressure and temperature drop in real fields.

1.3 Text structure

First, a flow assurance analysis of wax precipitation in a hypothetical oil and gas production line is performed using a hypothetical oil composition. Chapter 2 shows the paper entitled "Wax Appearance and Prevention in Two-Phase Flow using the Multi-Solid and Drift-Flux Model". In this paper, an algorithm was developed and applied to a case study useful for defining operational conditions to prevent wax precipitation. The proposed algorithm predicts the minimum inlet temperature of the pipeline that avoids the wax precipitation; besides that the effect of the flow rate on the minimum inlet temperature was studied. The paper is cited as follows: "GOES, M. R. R., TEIXEIRA, R. G., TAVARES, F. W., SECCHI, A. R., 2019, Wax appearance and prevention in two-phase flow using the multi-solid and drift-flux model, *Journal of Petroleum Science and Engineering*, v. 177 (jun), pp. 374–383. doi: 10.1016/j.petrol.2019.02.057"

In order to perform flow assurance analysis in real scenarios, a virtual flow metering method and an improvement of the black oil delumping method are proposed. Those methodologies provide tools for fluid simulation of real case scenarios. Chapter 3 shows the paper entitled "Virtual flow metering of oil wells for a pre-salt field." The installation of flow measuring equipment in each well is not feasible in practice, due to the high cost of equipment and installation. This work proposed a method to predict the liquid and gas flow rate of each independent well of a platform as a function of plant data collected in real time, choke valve specification, and fluid properties. Relative errors between the predicted flow rates and the provided by fiscal meters were below 3.5% and 3% for the total oil and gas flow rates, respectively. Therefore, the results provided by virtual flow meter proposed in this work are in good agreement with the DOR (Daily Operation Report) and fiscal measurement data. The paper is cited as follows: "GÓES, M. R. R., GUEDES, T. A., D'AVILA, T. C., VIEIRA, B. F., RIBEIRO, L. D., DE CAMPOS, M. C., SECCHI, A. R., 2021,

Virtual flow metering of oil wells for a pre-salt field, *Journal of Petroleum Science and Engineering*, v. 203. doi: 10.1016/j.petrol.2021.108586"

Chapter 4 shows the paper entitled "Improvement of black oil delumping method applied to an offshore oil field". In this work, an improvement in converting black oil data into a compositional wellstream is proposed and evaluated using data from three wells from an offshore oil field. Unlike the literature, the proposed method fully describes how to obtain an initially estimated composition. Also, the molar mass of the pseudocomponent of the oil stream as the fitting parameter significantly increased the accuracy of the method. The efficiency of the proposed method was tested by comparing with measured GOR, $^{\circ}API$, and γ_g given in Well Test Reports, PVT Analysis, and Gas Chromatographic Analysis of three wells from an offshore oil production field, showing a high degree of accuracy. The paper is cited as follows: "GÓES, M. R. R., GUEDES, T. A., D'AVILA, T., RIBEIRO, L. D., DE CAMPOS, M. C. M., SECCHI, A. R., TAVARES, F. W., 2022, Improvement of black oil delumping method applied to an offshore oil field, *Journal of Petroleum Science and Engineering*, v. 214. doi: 10.1016/j.petrol.2022.110514"

Chapter 5 shows the paper entitled "Multiphase flow simulation in offshore pipelines: an accurate and fast algorithm applied to real-field data". In this paper, an iterative algorithm to predict the oil behavior during the multiphase flow in real offshore pipelines using a fluid composition based on the black oil properties of real oil is proposed. The pipe wall roughness was used as a fitting parameter. The goal is to calculate an optimum pipe wall roughness, so whenever applying it to fluid flow monitoring or flow assurance analysis, the pressure drop along the pipeline is adequately predicted, for example, since this parameter affects it directly. The paper is cited as follows: "GÓES, M. R. R., GUEDES, T. A., TEIXEIRA, R. G., MELO, P. A., TAVARES, F. W., SECCHI, A. R., 2023, Multiphase flow simulation in offshore pipelines: An accurate and fast algorithm applied to real-field data, *Chemical Engineering Science*, v. 268. ISSN: 00092509. doi: 10.1016/j.ces.2022.118438"

Chapter 6 shows the general conclusions and suggestions for future researches.

Appendix A, B, C, D, E, F, and G show complementary materials.

Chapter 2

Wax Appearance and Prevention in Two-Phase Flow using the Multi-Solid and Drift-Flux Model

Wax precipitation may lead to the obstruction of pipelines generating significant economic losses. Oil reservoirs, especially in the deepwater sea, are found in extreme conditions of pressure and, during the fluid flow inside the pipelines, the fluid temperature may decrease due to heat transfer to the surrounding (seawater) and phase change, tending to deposit solid particles on the pipeline walls. Within this context, it is important to develop a model that calculates the WAT of a fluid with known composition and then determines the point where the first paraffin crystal will appear inside a pipeline. The objective here is to provide a two-phase flow model coupled with a paraffin precipitation model to calculate WAT inside the pipeline. We used the Drift-Flux Model to describe the two-phase flow in a steady state and the Multi-Solid Theory to calculate the WAT. The results for a paraffinic mixture of four components show that the effect of the pressure can be considered negligible on WAT calculation for low-pressure systems (< 10MPa). Analyzing the effect of the fluid composition, the larger the number of light compounds in the mixture, the smaller will be the WAT, at constant pressure. For two different cases, it was determined the point inside the pipeline where the solid particles may deposit. We proposed an algorithm to find the minimum inlet temperature that does not occur wax precipitation along the pipeline. The algorithm was successfully applied to a case study and maybe useful for defining operational conditions to prevent solid blockage of pipelines.

2.1 Introduction

The petroleum is, basically, a mixture of light and heavy hydrocarbons composed of paraffinic, naphthenic, and aromatic compounds. It is known that paraffinic oils with high molecular weight are found in a solid state under standard conditions (LIRA-GALEANA *et al.*, 1996).

Petroleum reservoirs are found thousands of meters below the surface, mainly those located in the deepwater sea. In the ultra-deep water sea, several reservoirs are found at 7,000 meters deep at temperatures of 423 K and pressures around 60 MPa. In this scenario, the temperature decreases in the pipeline due to (1) the heat transfer between the fluid and its neighborhood (seawater) and (2) the phase change (vaporization) due to the pressure drop. Thus, as the fluid temperature reaches the WAT, solid particles may precipitate on the pipe walls (PASO *et al.*, 2009). This phenomenon decreases the oil flow rate due to the partial blockage of the pipeline (COUTINHO *et al.*, 1995; LIRA-GALEANA *et al.*, 1996). In extreme cases, the companies must remove the pipe section because of the total or partial blockage, and this procedure costs around 30 million dollars (VENKATESAN, 2004). Another alternative is the removal of the wax by mechanical or chemical methods, but these methods have limited efficiency (AIYEJINA *et al.*, 2011).

The wax precipitation can be explained by three theories: (1) Solid Solution Model, (2) Multi-Solid Model and (3) Multiple Solid Solutions Model. The Solid Solution Model is based on the fact that the precipitated paraffins form a unique homogeneous solid phase in which its components are miscible with one another (WON, 1986). The theory based on the Multi-Solid Model affirms that the paraffins precipitate, forming multiple solid phases that are independent and immiscible with one another (LIRA-GALEANA *et al.*, 1996). LIRA-GALEANA *et al.* (1996) introduced the multi-solid precipitation model, in which the WAT can be determined by a simple stability test, and stated that this method is both simple and accurate, requiring no adjustable mixture parameters for the solid phase. NICHITA *et al.* (2001) introduced into the LIRA-GALEANA *et al.*'s model a term that accounts for the transition of phases in the solid state for the calculation of the fugacity of the solid. In contrast to the Multi-Solid Model, the Multiple Solid Solutions Model proposes that the paraffins precipitate, forming multiple solid phases in which each of them are composed of a solid solution (COUTINHO, 1998). It was used here the Multi-Solid Model.

In fact, two conditions must be met in order to occur this phenomenon: (1) the temperature of the pipe wall must be below the WAT, and (2) the temperature

gradient must be negative along the pipeline (PASO *et al.*, 2009).

TEIXEIRA and SECCHI (2017) implemented two methods to study the behavior of the fluid flow inside a pipe: (1) Drift-Flux Model and (2) Two-Fluid Model. Taking into account the accuracy and computational cost of the models compared with experimental data, these authors proved the higher performance of the Drift-Flux Model. This model was used here to describe the fluid flow.

The objective here is to provide a model to simulate the two-phase fluid flow augmented with the wax precipitation calculations at pipeline conditions. We studied the effects of composition, pressure, and temperature of the fluid on the WAT and developed an algorithm that calculates minimum inlet temperature such that does not occur wax precipitation inside the pipeline.

2.2 Methodology

In order to verify the wax precipitation of a fluid at certain temperature, pressure, and composition, FIROOZABADI (1999) used the stability analysis based on Eq. 2.1.

$$f_i^L\left(P,\, T,\, x_i^L\right) - f_{i\,pure}^S\left(P,\, T\right) \geq 0 \tag{2.1}$$

where $f_{i\,pure}^S$ is the fugacity of pure component i in the solid phase, f_i^L is the fugacity of component i in the liquid phase, P and T are the pressure and temperature of the system, respectively.

In order to calculate the thermodynamic properties at vapor, liquid, and solid phases, at the equilibrium conditions, the liquid phase can be described either by activity coefficients and equations of state (EOS). Here, we used the Peng-Robinson equation of state (PR-EOS) to calculate thermodynamic properties of the liquid and vapor phases. For the solid phases, each fugacity is calculated by the modified expression provided by NICHITA *et al.* (2001), as shown in Eq. 2.2.

$$f^{S}_{i\,pure}\left(P,T\right) = f^{L}_{i\,pure}\left(P,T\right) \times \exp\left[-\frac{\Delta h^{f}_{i}}{RT^{f}_{i}}\left(\frac{T^{f}_{i}}{T}-1\right)+\frac{\Delta h^{tr}_{i}}{RT}\left(\frac{T}{T^{tr}_{i}}-1\right)\right.$$
$$+\frac{1}{R}\int_{T}^{T^{f}_{i}}\frac{\Delta c_{Pi}}{T}dT-\frac{1}{RT}\int_{T}^{T^{f}_{i}}\Delta c_{Pi}dT \qquad (2.2)$$
$$\left.+\frac{\Delta v_{i}}{RT}\left(P^{f}_{i}-P\right)\right]$$

$$f^{L}_{i\,pure}\left(P,T\right) = \phi^{L}_{i\,pure}(P,T) \times P \qquad (2.3)$$

where $f^{L}_{i\,pure}$ is the fugacity of pure component i in the liquid phase; T^{tr}_{i} e Δh^{tr}_{i} are the solid-solid transition temperature and transition molar enthalpy, respectively, of component i in the solid phase; Δv_i and Δc_{Pi} are the variation of molar volume and heat capacity, respectively, of component i; Δh^{f}_{i} is the molar enthalpy of fusion of component i; T^{f}_{i} and P^{f}_{i} are the fusion temperature and pressure, respectively, of component i; R is the real gases constant; and $\phi^{L}_{i\,pure}$ is the fugacity coefficient of pure component i in the liquid phase. The last term on the right side of Eq. 2.2 is the Poyting Factor, which accounts for the effect of pressure on the solid fugacity.

The Drift-Flux Model was chosen, based on the conclusions made by TEIX-EIRA and SECCHI (2017), to describe the two-phase fluid flow inside the pipeline, which was proposed by HIBIKI and ISHII (2003). This model is composed by 4 differential equations and one constitutive equation, which are described in Eqs. 5.1 - 5.4 and 5.5, respectively.

$$\frac{d\left(\rho^{m}v^{m}\right)}{dx} = 0 \qquad (2.4)$$

$$\frac{d\left[\rho^{m}(v^{m})^{2}\right]}{dx} = -\frac{dP}{dx} - F_{mw} - \rho^{m} g\, sin(\theta) - \frac{d}{dx}\left(\frac{\alpha^{V}\rho^{L}\rho^{V}}{\alpha^{L}\rho^{m}}\hat{v}^{des^{2}}_{v}\right) \qquad (2.5)$$

$$\begin{aligned}\frac{d\left(\rho^{m}v^{m}h^{m}\right)}{dx} =& \dot{Q}_{tw} - \frac{d}{dx}\left[\frac{\alpha^{V}\rho^{V}\rho^{L}}{\rho^{m}}\left(h^{V}-h^{L}\right)\hat{v}^{des}_{v}\right] \\ &+\left[v^{m}+\frac{\alpha^{V}\left(\rho^{L}-\rho^{V}\right)}{\rho^{m}}\hat{v}^{des}_{v}\right]\frac{dP}{dx}\end{aligned} \qquad (2.6)$$

$$\frac{d\left(\alpha^{V}\rho^{V}v^{m}\right)}{dx} = \Gamma^{V} - \frac{d}{dx}\left(\frac{\alpha^{V}\rho^{V}\rho^{L}}{\rho^{m}}\hat{v}^{des}_{v}\right) \qquad (2.7)$$

$$\hat{v}^{des}_{v} = \left\langle \hat{v}^{des}_{v}\right\rangle_{\alpha} + \left(C_0 - 1\right)\left\langle j\right\rangle \qquad (2.8)$$

where ρ^m, ρ^L and ρ^V are the mixture, liquid phase, and vapor phase density, respectively; F_{mw} is the frictional loss of pressure; v^m is the mixture velocity; θ is the

inclination angle of the pipeline; α^V is the vapor void fraction; h^m, h^V and h^L are the mixture, vapor and liquid enthalpies, respectively; $\dot{Q}_{tw}$ is the heat exchange rate; Γ^V is the vapor mass generation rate, $\hat{v}_v^{des}$ is the slip velocity of the vapor phase, $\langle j \rangle$ is the mixture superficial velocity; $\left\langle \hat{v}_v^{des} \right\rangle$ and C_0 are model parameters.

The heat exchange between the fluid and its neighborhood is described by Eq. 5.24.

$$\dot{Q}_{tw} = 4\frac{U_{heat}(T_{viz} - T)}{D_{int}} \tag{2.9}$$

where U_{heat} is the overall heat transfer global coefficient calculated from Eq. 2.10, D_{int} is the inner diameter of the pipe and T_{viz} is the neighborhood (seawater) temperature. In this work, T_{viz} was estimated as 6°C.

$$U_{heat} = \frac{2}{D_{int}}\left[\frac{ln(D_{out}/D_{int})}{k_t} + \frac{\ln(D_{iso}/D_{out})}{k_i} + \frac{2}{h_{viz}D_{iso}}\right]^{-1} \tag{2.10}$$

where D_{out} is the outer diameter of the pipe, D_{iso} is the outer diameter plus the insulation thickness of the pipe, h_{viz} is the convective heat transfer coefficient of the neighborhood, k_t is the thermal conductivity of the pipe and k_i is the thermal conductivity of the insulation. The values of these properties are described in Table 2.1.

Table 2.1: Material properties and dimensions of the pipeline.

k_t	50 $W/(m\,K)$
k_i	0.1350 $W/(m\,K)$
h_{viz}	6.5 $W/(m^2\,K)$
	Flowline
D_{int}	0.14 m
D_{out}	0.1550 m
D_{iso}	0.1850 m
	Riser
D_{int}	0.1016 m
D_{out}	0.1166 m
D_{iso}	0.1166 m

The vapor mass generation rate is evaluated by Eq. 2.11. This expression is shown in Appendix A.

$$\Gamma^V = \rho^m v^m \frac{d\beta_W}{dx} \tag{2.11}$$

where β_W is the vaporized mass fraction.

In order to calculate the parameters of the Drift-Flux Model, it was used the correlations provided by BHAGWAT and GHAJAR (2014) which are independent of the fluid flow regime. Details of this set of correlations are given in Appendix D.

The calculation of liquid and vapor phase enthalpies was performed using the residual properties, which is recommended by DAUBERT and DANNER (1997), as detailed in Appendix B. The physical properties of the fluids were calculated using the correlations provided by the literature shown in Table 2.2. The details of these correlations are described in Appendix C.

Table 2.2: Physical properties of the fluid.

Liquid phase		Vapor phase	
Density	THOMSON *et al.* (1982)	Density	RIAZI (2005)
Viscosity	LOHRENZ *et al.* (1964)	Viscosity	LEE *et al.* (1966)
Surface tension	DAUBERT and DANNER (1997)		

The properties of the pure components were obtained from the literature, as described in Table 2.3, where P_c, T_c, and V_c are the critical pressure, temperature and volume, respectively; MM is the molar mass; w is the acentric factor; Z_{RA} is the compressibility factor; $Parachor$ is used to evaluate the liquid surface tension; V° is the characteristic volume and w_{SRK} is the acentric factor calculated using the EOS SRK (Soave-Redlich-Kwong Equation of State).

Table 2.3: Physical properties of the pure components.

P_c, T_c, V_c, w and MM	DAUBERT and DANNER (1997)
w_{SRK} and V°	HANKINSON and THOMSON (1979)
Z_{RA}	SPENCER and DANNER (1972)
$Parachor$	QUAYLE (1953)

The Drift-Flux Model was implemented in the computational environment MATLAB R2008, with the differential-algebraic equations (DAE) solved by DASSLC extension for MATLAB provided by SECCHI (2012). The absolute and relative tolerances for the DAE were set to 10^{-8} and 10^{-6}, respectively.

The pipeline of the offshore oil production well used for the simulations is

described in Fig. 2.1. This well is considered to be producing by primary recovery.

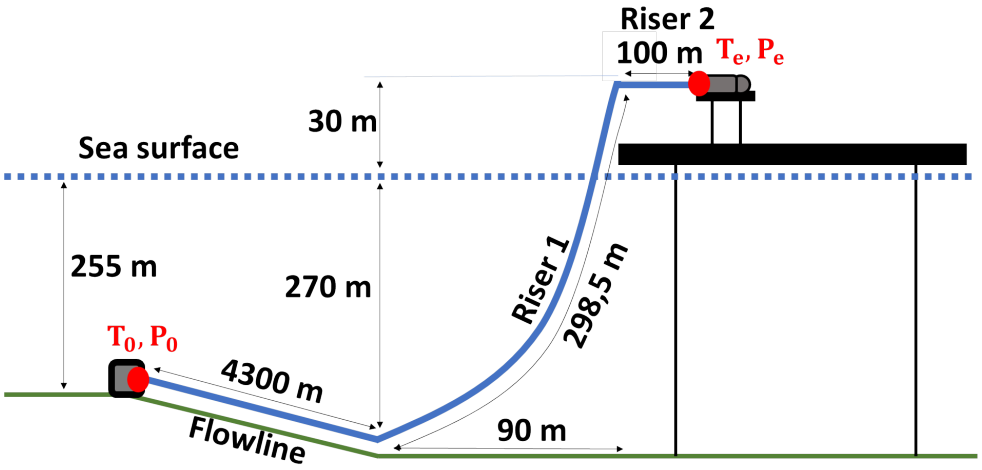

Figure 2.1: Offshore oil production field where (T_0, P_0) and (T_e, P_e) are the inlet and outlet temperature and pressure of the pipeline, respectively. Adapted from NEMOTO *et al.* (2010).

The material properties and the dimensions of the pipeline were the same as used by NEMOTO *et al.* (2010), which are shown in Table 2.1. A catenary shape was used to describe the section Riser 1.

In order to validate the Drift-Flux Model, it was used the fluid shown in WHITSON and BRULÉ (2000) and the software OLGA to describe the fluid flow. The fluid contains 10 components and 1 pseudocomponent. The physical properties of the pseudocomponent were calculated using the correlations listed in Table F.1, where $(T_c)_{C+}$, $(P_c)_{C+}$ and $(V_c)_{C+}$ are the critical temperature, pressure, and volume of the pseudocomponent; $(w)_{C+}$, $(V^\circ)_{C+}$ and $(P_{ch})_{C+}$ are the acentric factor, the characteristic volume, and the parachor value of the pseudocomponent. The pure component properties for this fluid were obtained from software Multiflash, as shown in Table 2.5. According to the manual, the software Multiflash is system for modelling physical properties and phase equilibria MULTIFLASH (2014).

Table 2.4: Physical properties of the pseudocomponent.

$(T_c)_{C+}$	732.07 K
$(P_c)_{C+}$	1.6682×10^6 Pa
$(w)_{C+}$	0.9679
$(V_c)_{C+}$	0.0040 m^3/kg
$(V^\circ)_{C+}$	0.9349
$(P_{ch})_{C+}$	575.98

Table 2.5: Pure component properties for the fluid given in WHITSON and BRULÉ (2000) (MULTIFLASH, 2014).

Component	MM $[kg/mol]$	P_c $[Pa]$	T_c $[K]$	V_c $[m^3/kg]$	w [-]	PAR [-]
CO_2	0.0440	7377300	304.7280	0.0021	0.2230	72.2
N_2	0.0280	3395800	126.1922	0.0032	0.0372	60.1
Methane	0.0160	4599200	190.5639	0.0061	0.0104	72.6
Ethane	0.0301	4871800	305.3300	0.0048	0.0991	110
Propane	0.0441	4247660	369.8500	0.0045	0.1520	150.8
i-Butane	0.0581	3640000	407.8500	0.0045	0.1844	191.7
n-Butane	0.0581	3796000	425.1600	0.0044	0.1985	190.3
i-Pentane	0.0721	3377000	460.4500	0.0042	0.2270	229.4
n-Pentane	0.0721	3366500	469.7000	0.0043	0.2513	231
n-Hexane	0.0862	3018100	507.8200	0.0043	0.2979	271
C_{7+}	0.2280	1668194	732.0743	0.0040	0.6740	575.98

Here, two procedures were proposed: (1) calculating the minimum inlet temperature of the pipeline so that it does not occur wax precipitation during the fluid flow, and (2) verifying in which section of the pipeline the fluid begins to deposit solid particles, if the inlet temperature and pressure of the pipeline favor this phenomenon. These procedures are illustrated in Figs. 2.2 and 2.3, respectively.

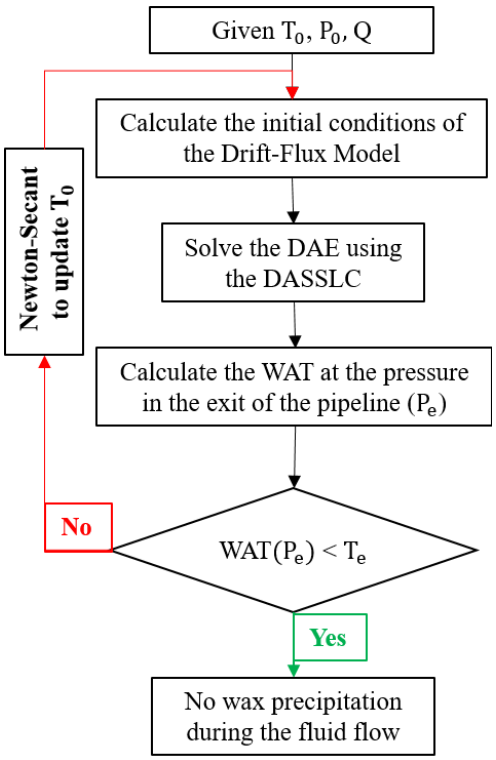

Figure 2.2: Procedure to calculate the minimum inlet T such that no wax precipitation occurs during the fluid flow.

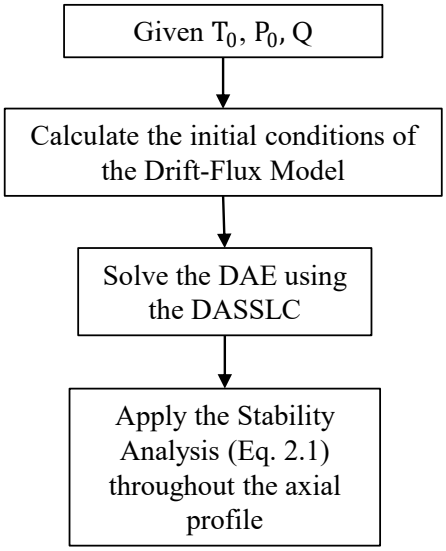

Figure 2.3: Procedure to verify in which section of the pipeline will occur wax precipitation if the initial conditions (T and P) favor this phenomenon.

2.3 Results and Discussion

2.3.1 Validation of the Wax Precipitation Model.

The WAT calculation was compared with the experimental data provided by DAUPHIN *et al.* (1999) at low pressure (1 bar), as shown in Fig. 2.4. DAUPHIN *et al.* (1999) divided the model oil in 5 types: 'BIM 0', 'BIM 3', 'BIM 5', 'BIM 9', and 'BIM 13'. These oil types are basically composed by paraffins with the number of carbons between 10 and 36 as shown in Appendix A.

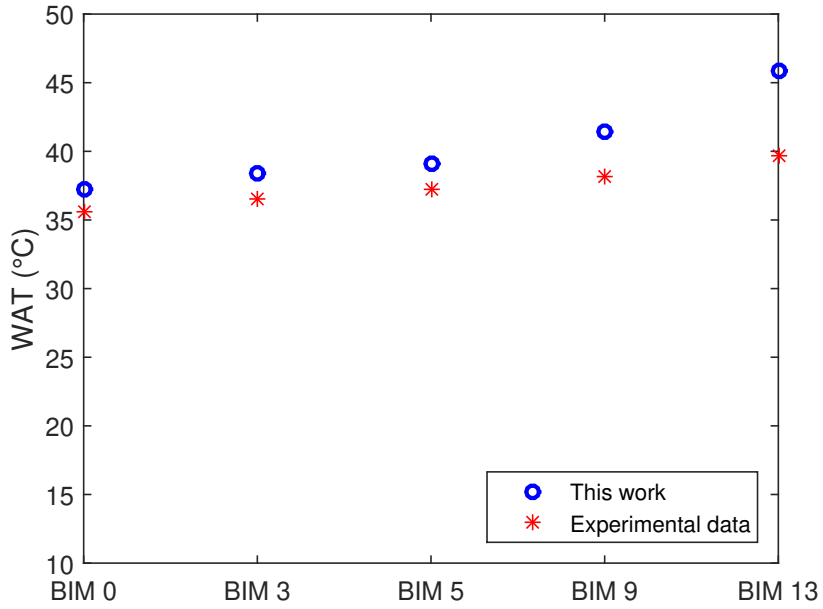

Figure 2.4: Comparison between WAT calculation and experimental data from DAUPHIN *et al.* (1999) at 1 bar.

Figure 2.4 shows that the first paraffin of oil 'BIM 13' appears at higher temperatures than the other oils. It happens because the fugacity of the pure component i, $f^S_{ipure}(P,T)$, depends upon physical properties, for example, molar mass, fusion temperature, and molar enthalpy of fusion, therefore the heaviest component of the mixture will have the greatest influence on the WAT calculation. Thus, the wax of oil 'BIM 13' precipitates at higher temperature when compared to the other oils, because the heaviest compound, n-hexatriacontane, is present in the greatest amount in this mixture.

The WAT calculations were, also, carried out at high pressure (420 bar) comparing with experimental data from RONNINGSEN *et al.* (1997) as shown in Figs. 2.5a and 2.5b. The two types of live oil: 'Oil10' and 'Oil11' were characterized by 5

components with number of carbons between 1 and 9, two iso-paraffins with 4 and 5 carbons, nitrogen, carbon dioxide and 1 pseudocomponent as shown in Appendix A. The density and molar mass of the pseudocomponents of 'Oil10' and 'Oil11' are different.

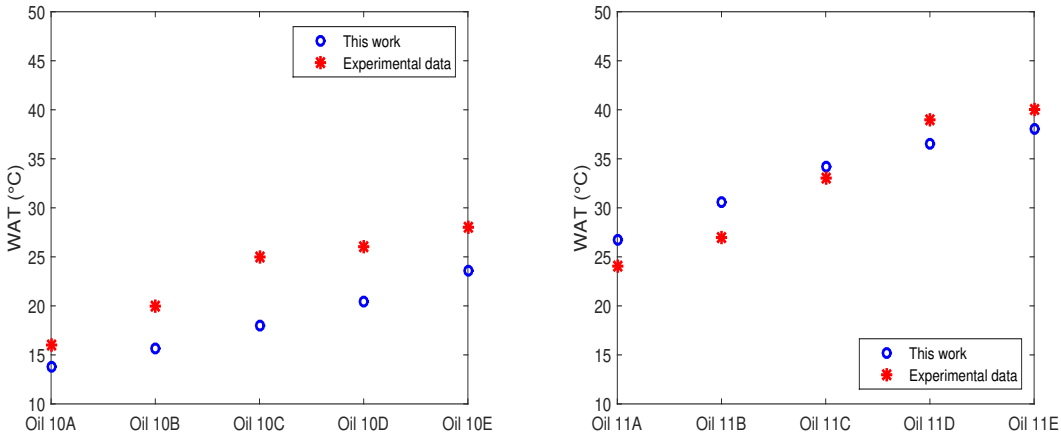

(a) (b)

Figure 2.5: Comparison between WAT calculation and experimental data from RONNINGSEN *et al.* (1997) at 420 bar.

Fig. 2.5 shows that the oils 'Oil 11' precipitate at higher temperature, except the oil 'Oil 11A' when compared to the oils 'Oil 10'. It happens because the molar mass of the heaviest compound of the oils 'Oil 11' is greater than 'Oil 10'. Although the molar mass of the heaviest compound of the oil 'Oil 11A' is greater than the molar mass of the heaviest compound of the oil 'Oil 10E', the molar fraction of the heaviest compound of the oil 'Oil 10E' is greater. For these oils, the mole fraction of the heaviest compound of the oils 'Oil 10E' and 'Oil 11A' are equal to 0.6264 and 0.1342, respectively.

Analyzing Figs. 2.5a and 2.5b separately, it is observed that paraffins from the oils 'Oil 10E' and 'Oil 11E' precipitate at higher temperatures when compared to the other oils. It happens because the mole fractions of the heaviest compounds of these oils are greater than the mole fractions of these compounds in the other oils.

2.3.2 Verification of the Drift-Flux Model

The axial temperature profile of the mixture used by WHITSON and BRULÉ (2000) using the methodology here presented was obtained and, then, the results were compared with the results obtained by software OLGA as shown in Fig. 2.6. WHITSON and BRULÉ (2000) used a mixture composed by carbon dioxide, ni-

trogen, two iso-paraffins with 4 and 5 carbons, paraffins with number of carbons between 1 and 6, and 1 pseudocomponent as shown in Appendix A. Fig. 2.6 indicates that the proposed model are capable to describe the fluid flow inside the pipeline with good agreement with the result from the software OLGA. The difference observed between the results can be attributed to the different models used, these being the Drift-Flux Model, in this work, and Two Fluid Model, in the software OLGA.

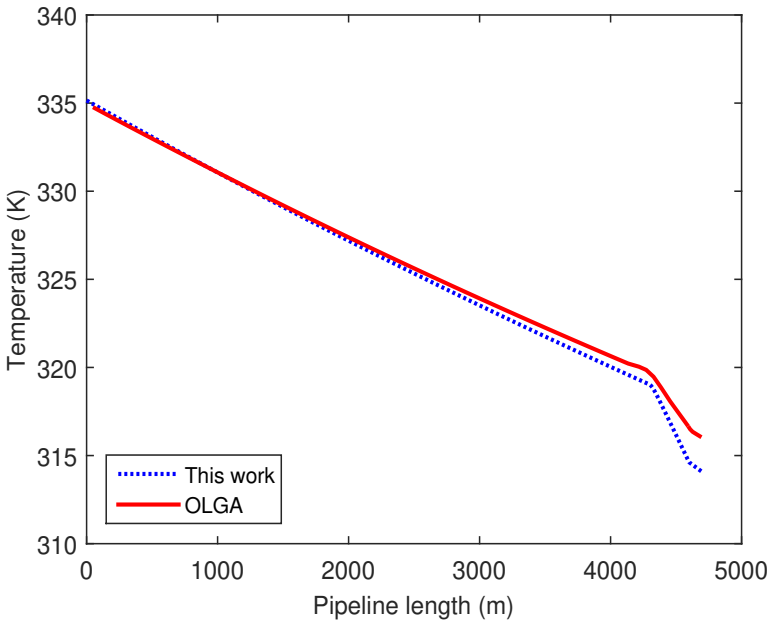

Figure 2.6: Comparison between the temperature profile in the pipeline obtained in this work with the simulation result from software OLGA.

2.3.3 Case Studies

The following simulations were carried out using a fluid composed by 4 components: (1) methane, (2) n-pentane, (3) n-decane and (4) n-eicosane. Since here the objective is to study wax precipitation, this mixture was chosen because is composed by light, medium and heavy paraffins. The global composition of the mixture and the operational data used to simulate the fluid flow is shown in Table 2.6.

Table 2.6: Global composition of the mixture and operational data.

Methane	0.50
n-Pentane	0.10
n-Decane	0.10
n-Eicosane	0.30
T_0	373.15 K
P_0	7 MPa
Q	20 kg/s

All the simulations were carried out using the dimensions of the pipeline described in Table 2.1 and the offshore oil production well illustrated in Fig. 2.1. The physical properties of the components were provided by the references described in Table 2.2. The axial profiles of pressure and temperature are illustrated in Figs. 2.7a and 2.7b, respectively.

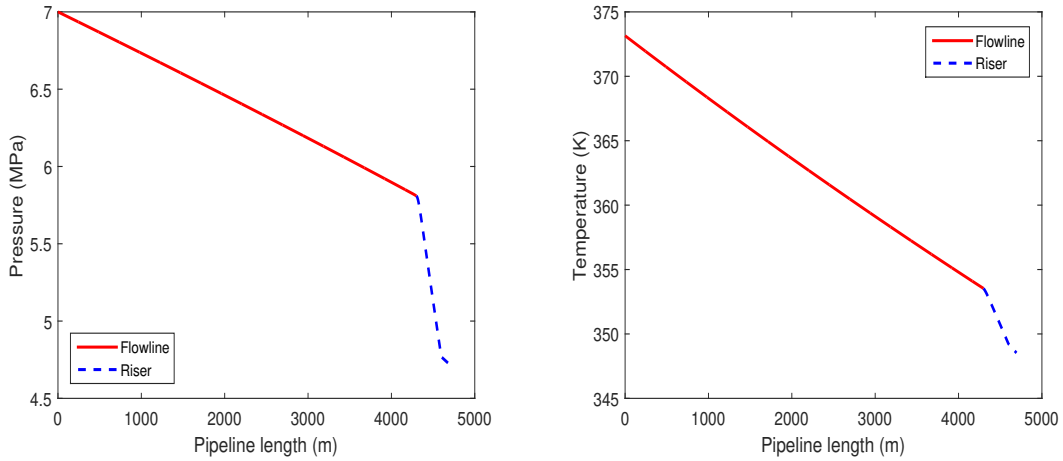

(a) (b)

Figure 2.7: Axial profile of (a) pressure and (b) temperature for the 4-components mixture flow in the pipeline.

The axial profiles of temperature and pressure are in accordance with the theory provided in the literature. As BRILL and MUKHERJEE (1999) stated, the fluid temperature tends to decrease due to the heat exchange with the neighborhood and, also the vaporization favored by the pressure drop, as can be seen in Fig. 2.7b. These authors also stated that the pressure tends to decrease due to friction loss and, consequently, the gas that is in solution is liberated.

The effect of temperature, pressure, and global composition of the mixture on the WAT was also investigated. Fig. 2.8 shows five different cases, which are described in Table 2.7.

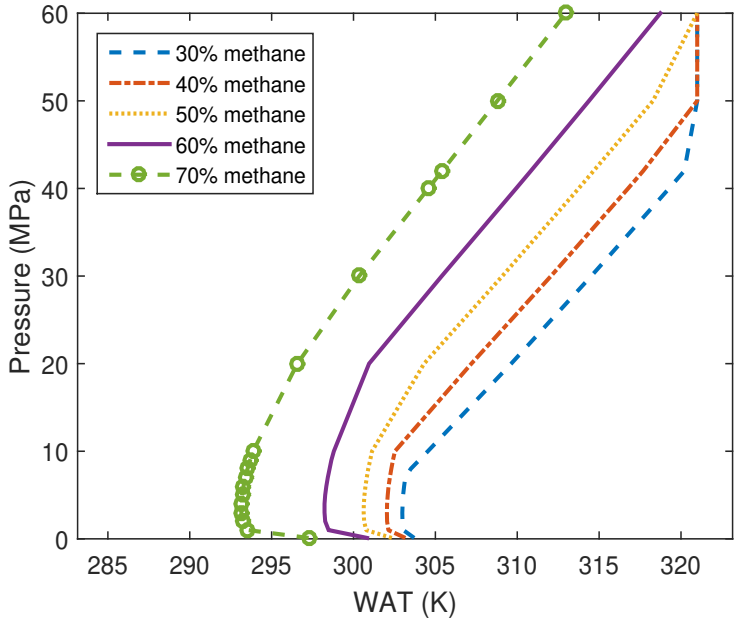

Figure 2.8: WAT Calculation as function of pressure for the Cases 1, 2, 3, 4 e 5.

Table 2.7: Global composition of the 4-component mixtures for the Cases 1, 2, 3, 4 e 5.

Case	Methane	n-Pentane	n-Decane	n-Eicosane
1	0.30	0.10	0.10	0.50
2	0.40	0.10	0.10	0.40
3	0.50	0.10	0.10	0.30
4	0.60	0.10	0.10	0.20
5	0.70	0.10	0.10	0.10

Analyzing Fig. 2.8, it can be noted that the larger the amount of light compounds in the mixture, the less the WAT. For example, the "Case 5" has the largest and least amount of methane and n-eicosane, respectively, thus at certain P this mixture has the lowest WAT compared to the other cases. In contrast, the "Case 1" has the least and largest amount of methane and n-eicosane, respectively, thus its WAT at certain P will be highest. This behavior can be attributed to the fact that the molar mass of the mixture with larger amounts of heavy components are higher when compared to mixtures with less amount of light components.

In order to study the effect of pressure, it was analyzed Cases 1 and 3. Fig. 2.8 shows that when the pressure is between 0.1 and 10 MPa, the WAT is almost constant varying from 304.35 to 304.05 K, for Case 1. The variation becomes significant when the pressure is above 10 MPa, varying about 15 K from 10 to 60 MPa. The same behavior can be observed in Case 3 which can be explained by the fact that

the term related to the Poynting Factor becomes important resulting in an increase of the WAT. In this work, the effect of pressure is negligible because the range of interest is between 5 and 10 MPa. It can also be noted that at low pressures, as the pressure increases, the WAT decreases, then the WAT increases . This behavior is noted for all the cases and, possibly, happen due to the two-phase region (liquid and vapor phase) at low pressures and one-phase region (liquid phase) at high pressures.

For the fluid flow, we performed the procedures presented in Figs. 2.2 and 2.3. The operational data used for these simulations are described in Table 2.8.

Table 2.8: Operational data for fluid flow simulations.

P_0	7 MPa
Q	20 kg/s
Fluid composition	Case 3

The results for the procedure described in Figs. 2.2 and 2.3 are shown in Fig. 2.9. Two simulations were carried out with T_0 set to 311.15 K and 316.15 K. Here, it was considered a safety temperature departure from WAT of +5 K on the simulations of WAT calculation.

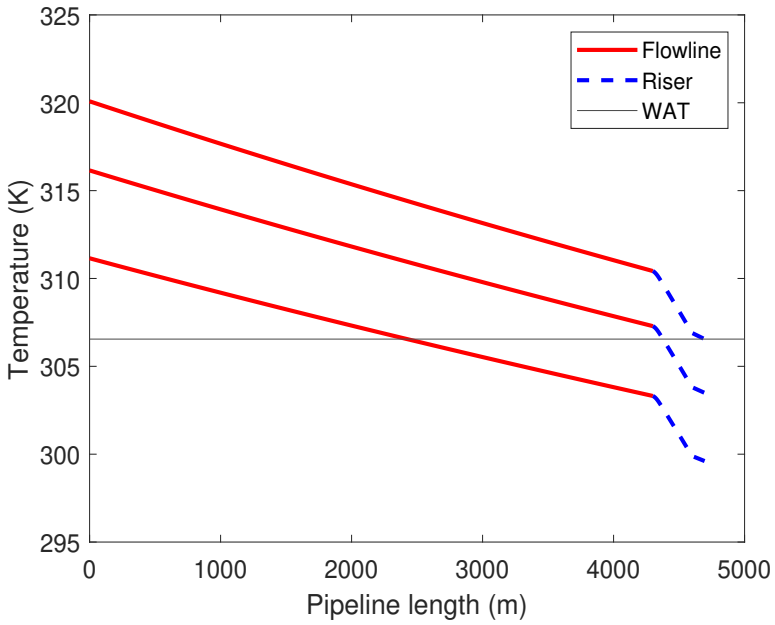

Figure 2.9: WAT calculation during the fluid flow with T_0 equal to 311.15, 316.15, and 320.1 K.

Fig. 2.9 shows that the wax precipitation will occur in the flowline for T_0 equal to 311.15 K and in the riser for T_0 equal to 316.15 K. As stated before, the stability analysis depends strongly on the temperature. Fig. 2.9 also shows the result of

the procedure described in Fig. 2.2, in which it was calculated the minimum inlet temperature such that no wax precipitation occurs during the fluid flow. This result indicates that the minimum inlet temperature must be greater than 320.1 K such that no wax precipitation occurs inside the pipeline.

The effect of the flow rate on the inlet temperature such that no wax precipitation occurs inside the pipeline was also analyzed. The operational data used in these simulations are described in Table 2.9. The results are shown in Figs. 2.10a and 2.10b.

Table 2.9: Operational data to analyze the effect of inlet flow rate.

P_0	7 MPa
Q	10, 15, and 20 kg/s

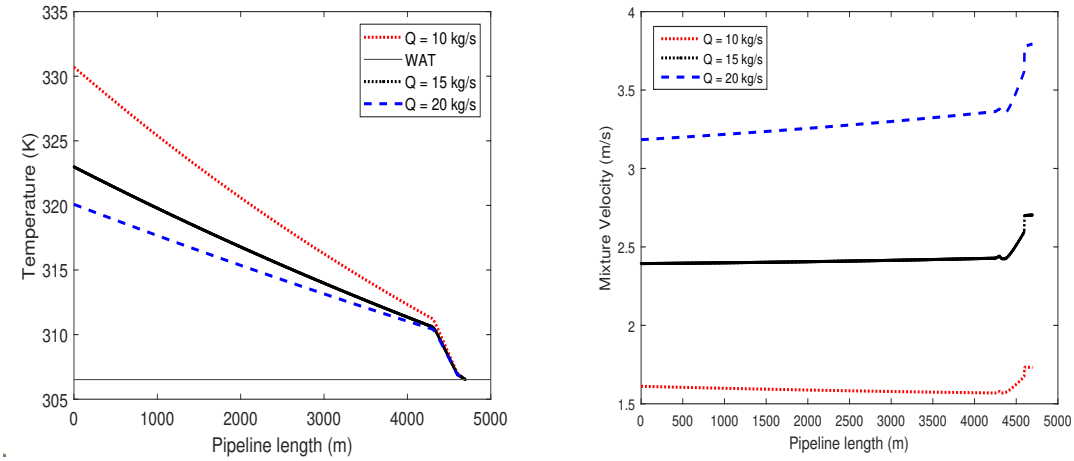

(a) (b)

Figure 2.10: Axial profile of (a) temperature and (b) mixture velocity.

Fig. 2.10a shows that for cases in which Q are equal to 10, 15, and 20 kg/s, the minimum inlet temperatures are 330.7, 323, and 320.1 K, respectively. It can be noted that the increase of flow rate caused a decrease on the minimum inlet temperature such that no wax precipitation occurs inside the pipeline. Fig. 2.10b shows that the mixture velocity is greater for the case in which Q is equal to 20 kg/s, therefore, the residence time is smaller when compared to the other cases. Consequently, the amount of heat exchanged with the neighborhood is lower. Thus, the minimum inlet temperature for the case in which Q is equal to 20 kg/s is the lowest. Also, the T_e equals the WAT, which is 306.5 K.

2.4 Partial Conclusions

In this chapter, it was studied the wax appearance and prevention during the two-phase flow of oil and gas mixtures for flow assurance. It used the Drift-Flux Model to describe the fluid flow and the Multi-Solid Theory to calculate the WAT.

The effect of pressure can be considered negligible in the WAT calculation for pressure in the range of 0.1 - 10 MPa. Using the information about the temperature at which the first paraffin crystal will appear, the WAT, it is possible to know in which section of the pipeline the paraffin crystal will start to grow. Depending on the inlet temperature, the wax precipitation may occur in different pipeline sections.

The algorithm proposed here to find the minimum inlet temperature of the pipeline that avoids the wax precipitation was successfully applied to a case study. Analyzing the effect of the flow rate on the minimum inlet temperature such that it does not occur wax precipitation during the fluid flow, the greater the inlet flow rate, the lower the minimum inlet temperature.

Chapter 3

Virtual Flow Metering of Oil Wells for a Pre-Salt Field

The flow rate values reported in real time for an oil and gas production unit refer to the total amount produced by that unit. On the other hand, data referring to the flow rate of each producing well in real time are usually not available due to the difficulty in implementing flow measurement devices. These individual flows are determined by production tests that are generally performed every two months and are important for production planning and optimization. Therefore, there is a need to generate models capable of predicting the flow of each well in the period between tests to identify possible issues during production. In this context, it is proposed in this chapter a method to predict the liquid and gas flow rates of each well as a function of measured variables available in plant data collected in real time. Choke valve specifications and fluid properties are also required as model input data. Since there is no flow measurement device, it is not possible to directly validate the model results against plant data. In this case, the model validation is performed using the total liquid and gas flow rates presented in the Daily Operation Report (DOR) and those provided by fiscal meters. Relative errors below 3.5% were observed, showing good agreement between the calculated flow rates and the provided by fiscal meters. The proposed method was implemented in the computational environment EMSO, which presents as advantages of the low simulation time and robustness over a wide range of input data. These advantages become important as the model is used for monitoring platforms in real time. The range of applicability of this model can be attributed to the Gas-Oil Rate (GOR). In this work, the lowest and highest values of GOR considering all the wells are 207.58 and 393.97, respectively.

3.1 Introduction

Mathematical models, used for the purpose of replacing measuring devices, are known either as virtual sensors, soft sensors, or inferential models. These virtual sensors are capable of estimate any system variable by using mathematical models, substituting physical sensors and using data acquired from other available variables (FORTUNA *et al.*, 2007).

Process variables such as temperature, pressure, differential pressure and single-phase flow rate are easy to measure with conventional sensor. The use of virtual sensors should be taken into consideration to infer on-line variables for which hardware sensors are not available or are very expensive (CHU *et al.*, 1998).

Concerning multiphase flow meters, these were developed in the early 1990s and increased the capability to monitor individual wells in real time in addition to offer a minimal loss of production through well tests shutdowns. These flow meters work as tools for achieving optimal operation and control of wells by delivering real time information. The reliability of multiphase flow meters installed in subsea locations is a key goal for oil and gas operators, as the cost of repairing or replacing failed subsea equipment is excessive. Moreover, multiphase flow meters are either expensive, innacurate, or can not be used downhole due to harsh conditions (GRAHAM, 2015; LESKENS *et al.*, 2008).

In this scenario, a new area of focus over recent years has been about virtual flow metering, which can be integrated into existing infrastructure eliminating the need for additional hardware and allowing real time modelling and optimization of production. For example, the pressure drop across a choke, wellhead temperature and the downhole pressure could be used as inputs to derive flow rate (GRAHAM, 2015). CARBONE (2007) used temperature and pressure values measured by the surface sensors of a platform as input variables of the virtual sensor, which estimates individual wells flow rates. LESKENS *et al.* (2008) evaluated some possibilities and limitations of such multiphase soft sensors, concluding that downhole pressure and temperature measurements alone are not sufficient to accurately estimate well flow rates in real time. The results are based on simulation and do not consider real well data. GARCÍA *et al.* (2010) presented an strategy for estimating individual well oil production based on a neural network and on-line correlation logic using data from sensors, well tests, and simulations. Prediction errors were calculated based on data from the most recent well test to feed the neural network training. Comparing the predictions with the fiscal meter, the approach presented results with errors below 4%. The study of AMIM (2015) evaluated the implementation and performance of

commercially available virtual flow meters, using real production data from a subsea well. These virtual sensors provided robust flow rate estimation over extended time periods. However, the challenging aspect of the study was the variation in the gas-oil ratio (GOR), which was not predicted by the PVT model defined for the virtual sensor.

QUTAMI *et al.* (2017) proposed a soft sensor based on neural networks for multiphase flow rates estimation in oil and gas production pipes. The developed sensor provides estimations between well tests if a common flow meter or test separator is installed. The soft sensor can also act as a backup when multiphase flow meters fail. URSINI *et al.* (2019) developed a real-time virtual flow meter by integrating commercial software packages and optimization algorithms, which can combine information from production network and reservoir. The virtual meter approach was successfully applied in an offshore gas field to estimate only gas production flow rates of each well in real time, using upstream choke and bottomhole pressure and temperature data. The work of SANZO *et al.* (2020) proposed a machine learning algorithm based on neural networks for multiphase flow rate estimation, considering the process parameters and the performance of installed equipment. Flow rates prediction is based on process parameters upstream and downstream the choke (i.e., pressure and temperature) and the choke opening. As the work of QUTAMI *et al.* (2017), this virtual flow meter can also act as a backup when multiphase flow meters fail.

The recent work of BIKMUKHAMETOV and JASCHKE (2020) presented a review of the state-of-art of virtual flow metering methods, the applied numerical methods, field experience and current research activity. This study suggested that future research should focus on developing auto-tuning and calibration methods. Moreover, the review concluded that the use of machine learning in virtual flow metering could improve the accuracy, but further research is required to make them robust.

The total flow rate produced, including all the wells, by a Production and Exploration Unit (PEU) can be reported in real time. However, the liquid and gas flow rate produced by each well are usually determined by a production test, which in some PEUs is performed every two months. In the period between tests, it is assumed that each well is producing as presented by the most recent Well Test Report. This may cause delays in identifying problems and it is not possible to track the production of each well during this period.

Regarding the works previously cited, LESKENS *et al.* (2008) presented case studies based on simulations, they did not consider real well data. GARCÍA *et al.*

(2010) used data from well test to feed the neural network training. AMIM (2015) did not comment the use of well test data. BIKMUKHAMETOV and JASCHKE (2020) reviewed the virtual flow metering methods and commented that between the well tests, the individual flow rates are assumed to be constant. In this work, it is proposed a method to predict the individual flow rates between the well tests based on the data given in the most recent Well Test Report.

The installation of flow measuring equipment in each well is not feasible in practice, due to the high cost of equipment and installation. In this context, we propose a method to predict the liquid and gas flow rate of each independent well of a platform as function of plant data collected in real time (i.e., temperature and pressure at choke valve), choke valve specifications and fluid properties. This data collection is performed through a Plant Information (PI) system, which corresponds to a software server/client modules responsible by the data collection, storage and exhibition of a process. Since there is no multiphase measuring equipment in the PEU, the model validation was done using the liquid and gas flow rates information presented in the Daily Operation Report and those provided by fiscal meters.

3.2 Method

In this work, the liquid and gas flow rates of individual wells were correlated with the pressure drop through the production choke valve and upstream temperature. The first step of the proposed method is to calculate the valve sizing coefficient, C_v, using the liquid (Q_l^{SC} in Nm^3/d) and gas (Q_g^{SC} in Nm^3/d) standard volumetric flow rates given in the production test of each well and the fluid analysis given in the Well Test and Gas Chromatography Report. The variables across the choke, such as upstream and downstream pressure of the choke valve (P_{us} and P_{ds} in kPa), upstream temperature of the choke valve (T_{us} in K), gas-lift injection rate (Q_{gi} in m^3/d), and valve opening percentage (u in %), are monitored in real time during the period of the production test. These analyses are performed every two months on average. Table 3.1 describes the mean, maximum and minimum values of the input data. The range values for this model can be considered as the minimum and maximum values.

Table 3.1: Statistical summary of the input data describing the minimum, maximum and mean values of the input variables.

Input variable	**min**	**max**	**mean**
P_{us}^{test} (kPa)	2,747.25	3,888.70	3,097.70
P_{us}^{rt} (kPa)	2,614.55	13,392.12	4,989.32
GOR (Nm^3/Nm^3)	207.58	393.97	271.29
ρ_o^{SC} (kg/m^3)	857.8	889	873.4
BSW $(-)$	0.0001	0.0178	0.0022
M_g $(kg/kmol)$	24.7	29.2	25.83
P_{us} (kPa)	2,747.25	3,888.70	3,173.08
P_{ds} (kPa)	2,038.61	2,475.03	2,205.66
T_{us} (K)	21.34	34.03	27.30
u $(\%)$	16.02	100	78.94
Q_{gi} (Nm^3/d)	0	165.22	22.97
Q_g^{SC} (Nm^3/d)	740,935	1,549,271	1,026,475.4
Q_w^{SC} (Nm^3/d)	0.48	60.48	6,55
Q_o^{SC} (Nm^3/d)	3,103.1	4,038.6	3,671.65

In the period between these production tests, the C_v calculated in the first step of the proposed method is used to calculate the individual flow rates of the producing wells. In this way, the gas and liquid volumetric flow rates may be monitored between the production tests in real time.

The parameters of the model are presented below:

- Standard condition of pressure $\left(P^{SC}\right)$ set equal to 101.325 kPa;
- Standard condition of temperature $\left(T^{SC}\right)$ set equal to 288.706 K;
- Water density at standard condition $\left(\rho_w^{SC}\right)$ set equal to 948.252 kg/m^3;
- Air molar mass (M_{air}) set equal to 28.97 $kg/kmol$;
- Constant of real gases (R) set equal to $8,314.462$ $J/\left(kmol\,K\right)$;
- Produced water specific gravity (γ_{wf}) set equal to 1.04.

The following parameters are found in the analysis performed during the production test. These parameters may change at every production test:

- Gas-oil ratio at standard condition (GOR in Nm^3/Nm^3);

- Oil specific gravity (γ_o);
- Water cut at standard condition (BSW);
- Gas molar mass (M_g in $kg/kmol$) which is calculated through a gas chromatographic analysis.

3.2.1 Determining the Valve Sizing Coefficient, C_v

The variable C_v is defined as the water volumetric flow rate in m^3/d at 288.706 K (60 $^\circ F$) that flows through the valve and causes a pressure drop equal to 1 kPa using Equation 3.1.

$$C_v = \frac{1}{F_c} \frac{W_m}{\sqrt{\rho_w^{SC} \rho_m \left(P_{us} - P_{ds}\right)}} \tag{3.1}$$

where W_m is the mass flow rate through the valve in kg/d, ρ_m is the mixture density in kg/m^3, and F_c is a correction factor.

The correction factor, F_c, was proposed by CARBONE (2007), which is applied to adjust the upstream pressure, since the pressure provided in the production test (P_{us}^{test} in kPa) is different from the pressure measured in real time (P_{us}^{rt} in kPa). Therefore, this correction factor is set to 1 during the production test and is calculated as shown in Equation 3.2.

$$F_c = \frac{P_{us}^{test}}{P_{us}^{rt}} \tag{3.2}$$

The total mass flow rate (W_m in kg/d) is calculated using Equation 3.3.

$$W_m = W_g + W_l \tag{3.3}$$

where W_g and W_l (in kg/d) are the gas and liquid mass flow rates of each well, respectively.

Equation C.44 is used to calculate ρ_m.

$$\rho_m = \frac{W_m}{V_m} \tag{3.4}$$

where V_m is the volumetric flow rate, in m^3/d, which is evaluated by Equation 3.5.

$$V_m = V_g + V_l \tag{3.5}$$

where V_g and V_l are the gas and liquid volumetric flow rates of each well, in m^3/d, respectively.

Gas properties

The gas mass flow rate of each well, W_g, is calculated as shown in Equation 3.6.

$$W_g = Q_g^{SC} \rho_g^{SC} \tag{3.6}$$

where ρ_g^{SC} is the gas density at standard condition, in kg/m^3, and Q_g^{SC} is the gas volumetric flow rate, in Nm^3/d, at standard condition, given by Equation 3.7.

$$Q_g^{SC} = Q_{gi}^{SC} + Q_o^{SC} \left(GOR - Rs\right) \tag{3.7}$$

where Q_{gi}^{SC} is the gas-lift injection flow rate at standard condition, in Nm^3/d, described in Equation 3.8, Q_o^{SC} is the oil volumetric flow rate, in Nm^3/d, at standard condition, and Rs is the gas solubility ratio, in m^3/m^3, at P_{us} and T_{us}.

$$Q_{gi}^{SC} = \frac{Q_{gi}}{B_g} \tag{3.8}$$

where Q_{gi} is the real-time measurement of the gas-lift injection flow rate and B_g is the gas formation volume factor, in m^3/m^3, given by Equation 3.9.

$$B_g = \frac{P^{SC} T_{us}}{T^{SC} P_{us}} \tag{3.9}$$

The gas solubility is calculated using Equation 3.10 according to STANDING (1981) correlation. This correlation is applicable at and below the bubble point pressure of the crude oil.

$$Rs = \frac{\gamma_g}{5.6146} \left[(0.7969 P_{us} + 1.4) \times 10^{0.0125 API - 0.0016 T_{us} + 0.4183} \right]^{1.2048} \tag{3.10}$$

where *API degree* is an arbitrary scale developed by the American Institute of Petroleum. According to BRILL and MUKHERJEE (1999), the API degree of the

oil is calculated using Equation 3.11; and γ_g is the gas specific gravity calculated using Equation 3.12 (RIAZI, 2005) as the ratio of the gas and air molar masses.

$$API = \frac{141.5}{\gamma_o} - 131.5 \tag{3.11}$$

$$\gamma_g = \frac{M_g}{M_{air}} \tag{3.12}$$

The gas density (ρ_g in kg/m^3) is given by Equation 3.13.

$$\rho_g = \frac{\rho_g^{SC}}{B_g} \tag{3.13}$$

The gas density at standard condition (ρ_g^{SC} in kg/m^3) is given by Equation 3.14.

$$\rho_g^{SC} = \gamma_g \rho_{air}^{SC} \tag{3.14}$$

where ρ_{air}^{SC}, in kg/m^3, is the air density at standard condition and assuming an ideal gas, given by Equation 3.15.

$$\rho_{air}^{SC} = \frac{M_{air} P^{SC}}{R T^{SC}} \tag{3.15}$$

The gas volumetric flow rate (V_g in m^3/d) is given by Equation 3.16.

$$V_g = \frac{R T_{us} W_g}{M_{air} \gamma_g P_{us} Y^2} \tag{3.16}$$

where Y is the gas expansion factor described by Equation 3.17 (CARBONE, 2007).

$$Y = 1 - \frac{\Delta P / P_{us}}{2.25} \tag{3.17}$$

where ΔP is the pressure drop, in kPa, across the choke valve given by Equation 3.18. The value of Y must be between 2/3 and 1, otherwise the flow is considered critical.

$$\Delta P = P_{us} - P_{ds} \tag{3.18}$$

Liquid properties

The liquid mass flow rate of each well, W_l, is given by Equation 3.19.

$$W_l = W_o + W_w \tag{3.19}$$

where W_o and W_w are the oil and water mass flow rate, in kg/d, respectively, given by Equations 3.20 and 3.21.

$$W_o = Q_o^{SC} \rho_o^{SC} \tag{3.20}$$

$$W_w = Q_w^{SC} \rho_{wf}^{SC} \tag{3.21}$$

where Q_o^{SC} and Q_w^{SC} are the oil and water volumetric flow rates, in Nm^3/d, respectively, and ρ_{wf}^{SC} is the water density at standard condition, in kg/Nm^3.

Q_o^{SC} is evaluated by Equation 3.22.

$$Q_o^{SC} = Q_l^{SC} \left(1 - BSW\right) \tag{3.22}$$

where Q_l^{SC} is the liquid volumetric flow rate at standard condition, in Nm^3/d, given by Equation 3.23.

$$Q_l^{SC} = \frac{Q_l}{BSW\, B_w + \left(1 - BSW\right) B_o} \tag{3.23}$$

where B_w and B_o are the water and oil formation volume factor, in m^3/m^3, respectively.

The variable B_w is calculated as shown in Equation 3.24 (BRILL and MUKHERJEE, 1999; MCCAIN, 1990).

$$B_w = \begin{cases} \left(1 + \Delta W_P\right) \times \left[1 - \Delta W_T \left(P_b\right)\right] \exp\left[c_w \left(P_b - P_{us}\right)\right] & P_{us} \geq P_b \\ \left(1 + \Delta W_P\right) \times \left[1 - \Delta W_T \left(P_{us}\right)\right] & \text{otherwise} \end{cases} \tag{3.24}$$

where c_w is the water compressibility for gas-free water systems, in $1/kPa$, given by Equation 3.25 (MEEHAN, 1980), P_b is the bubble point pressure, in kPa, and ΔW_T and ΔW_P are parameters used to calculate B_w.

$$\begin{aligned} c_w =& 14.5037744 \times 10^{-6} \left[A_{cw} + B_{cw}(1.8T_{us} - 459.67) \right. \\ & \left. + C_{cw}(1.8T_{us} - 459.67)^2 \right] \end{aligned} \tag{3.25}$$

where A_{cw}, B_{cw}, and C_{cw} are parameters used to calcule the water compressibility, which are given by Equations 3.26-3.28 (MEEHAN, 1980).

$$A_{cw} = 3.8546 - 0.0019 P_{us} \tag{3.26}$$

$$B_{cw} = -0.01052 + 6.9183 \times 10^{-6} P_{us} \tag{3.27}$$

$$C_{cw} = 3.9267 \times 10^{-13} - 1.2763 \times 10^{-8} P_{us} \tag{3.28}$$

The bubble point pressure, P_b, is calculated through Equation 3.29 (LASATER, 1958). This correlation may be applied at temperature, and gas specific gravity in the range of 274.26 - 314.26K, and 0.574 - 1.223, respectively.

$$P_b = \left[0.679 \exp\left(2.786 \gamma_g\right) - 0.323 \right] \frac{1.8 T_{us}}{y_g \gamma_g} \tag{3.29}$$

where y_g is the gas mole fraction calculated using Equation 3.30 (LASATER, 1958). The latter may be applied for GOR in the range of 0.53 - 515.40 m^3/m^3.

$$y_g = \frac{0.0148 GOR}{0.0148 GOR + 350 \gamma_o / M_o} \tag{3.30}$$

where M_o is the oil mass molar, in $kg/kmol$, given by Equation 3.31 available in LASATER (1958). This correlation may be applied for $^\circ API$ in the range from 17.9 to 51.1.

$$M_o = 630 - 10 API \tag{3.31}$$

The parameters ΔW_T and ΔW_P are calculated using Equations 3.32 and 3.33, respectively (MCCAIN, 1990). These correlations are valid for temperature and pressure up to 399.81K and 34.47MPa, respectively.

$$\begin{aligned}\Delta W_T(P) = &-5.0987\times10^{-8}(1.8T_{us}-459.67)P \\ &-6.5443\times10^{-11}(1.8T_{us}-459.67)P^2 \\ &+7.8153\times10^{-6}P-3.0691\times10^{-8}P^2\end{aligned} \tag{3.32}$$

$$\begin{aligned}\Delta W_P = &-1.0001\times10^{-2}+1.33391\times10^{-4}(1.8T_{us}-459.67) \\ &+5.50654\times10^{-7}(1.8T_{us}-459.67)^2\end{aligned} \tag{3.33}$$

The oil formation volume factor, B_o, is calculated as shown in Equation 3.34 (BRILL and MUKHERJEE, 1999; STANDING, 1981).

$$B_o = \begin{cases} 0.9759+0.00012\left(5.6146GOR\sqrt{\gamma_g/\gamma_o}+2.25T_{us}\right. & \\ \left.-574.5875\right)^{1.2}\exp\left[c_o\left(P_b-P_{us}\right)\right] & P_{us}\geq P_b \\ 0.9759+0.00012\left(5.6146Rs\sqrt{\gamma_g/\gamma_o}+2.25T_{us}\right. & \\ \left.-574.5875\right)^{1.2} & \text{otherwise} \end{cases} \tag{3.34}$$

where c_o is the oil compressibility, in $1/kPa$, calculated as shown in Equation 3.35, respectively (FRASHAD *et al.*, 1996; STANDING, 1981).

$$c_o = 14.5037744\times10^{(-5.4531+5.03\times10^{-4}\times X_{co}-3.5\times10^{-8}\times X_{co}^2)} \tag{3.35}$$

where X_{co} is a parameter used to calculate c_o, given by Equation 3.36 (FRASHAD *et al.*, 1996).

$$\begin{aligned}X_{co} = &(5.6146Rs)^{0.1982}\left(1.8T_{us}-459.67\right)^{0.6685}\gamma_g^{-0.21435}API^{1.0116} \\ &(14.5037744P_{us})^{-0.1616}\end{aligned} \tag{3.36}$$

The variables ρ_o^{SC}, Q_w^{SC} and ρ_{wf}^{SC} are calculated as described in Equations 3.37, 3.38 and 3.39, respectively.

$$\rho_o^{SC} = \rho_w^{SC}\gamma_o \tag{3.37}$$

$$Q_w^{SC} = Q_l^{SC}BSW \tag{3.38}$$

$$\rho_{wf}^{SC} = \rho_w^{SC}\gamma_{wf} \tag{3.39}$$

The liquid volumetric flow rate, V_l, is given by Equation 3.40.

$$V_l = \frac{W_l}{\rho_l} \tag{3.40}$$

where ρ_l is the liquid density, in kg/m^3, calculated as shown by Equation 3.41.

$$\rho_l = \rho_o\left(1 - WC\right) + \rho_w WC \tag{3.41}$$

where ρ_o and ρ_w are the oil and water density, respectively, in kg/m^3, at fluid condition, and WC is the water cut.

The oil density, ρ_o, at fluid condition is given by Equation 3.42 (BRILL and MUKHERJEE, 1999).

$$\rho_o = \begin{cases} \frac{62.4\gamma_o + 0.076359GOR\gamma_g}{0.0624B_{ob}} \exp\left[c_o\left(P_{us} - P_b\right)\right] & P_{us} \geq P_b \\ \left(62.4\gamma_o + 0.076359Rs\gamma_g\right)/0.0624B_o & \text{otherwise} \end{cases} \tag{3.42}$$

The water density, ρ_w, can be calculated using Equation 3.43.

$$\rho_w = \frac{\rho_{wf}^{SC}}{B_w} \tag{3.43}$$

The water cut, WC, is given by Equation 3.44.

$$WC = \frac{Q_w^{SC}}{Q_l^{SC}} \tag{3.44}$$

	Range of applicability
Eq. 3.29	$0.574 < \gamma_g < 1.223$
	$300.93 < T_{us} < 406.98$

3.2.2 Determining the Real-Time Volumetric Flow Rates, Q_l and Q_g

In this part of the proposed method, the real-time volumetric flow rates of each well, Q_l and Q_g, are determined using the procedure described in the previous step using the C_v, calculated at the production test, as a model input. Therefore the variables of interest are calculated implicitly using Equation 3.1 and the subsequent model equations.

Figure 3.1 shows the flow chart describing the two steps of the proposed method.

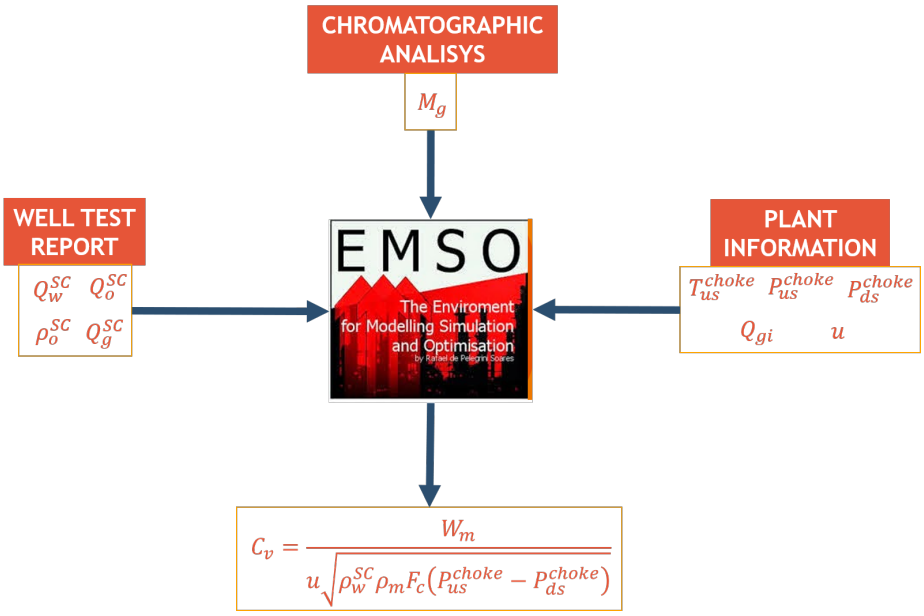

(a) Determining C_v.

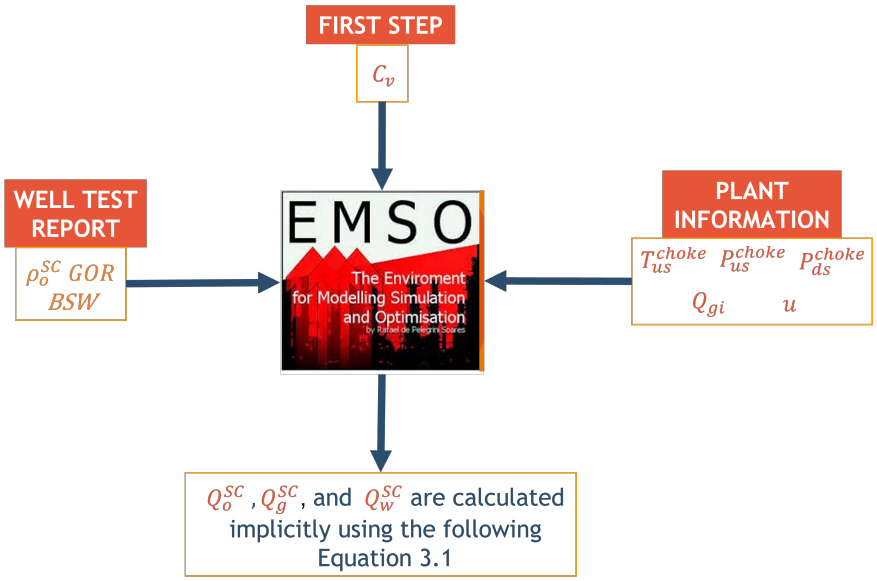

(b) Determining the real-time volumetric flow rates.

Figure 3.1: Flow chart describing the (a) first and (b) second step of the method.

3.3 Results and Discussion

The individual well flow rates were predicted according to the proposed method for all wells of a platform from the pre-salt field. Then, the total oil and gas flow rates produced in the platform were calculated and compared to the total oil and gas flow rates provided in the DOR and fiscal measurement data. Fiscal measurement data were collected at every second and the daily average, for each period, was calculated for comparison purpose. This last procedure was required because the

data given by the DOR are reported as daily results. Nine different daily period of DOR were selected. Figures 3.2 and 3.3 show the results of the comparison between the data.

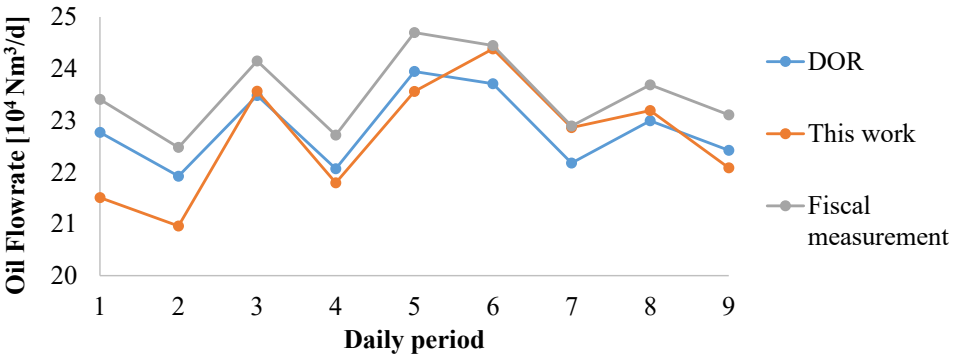

Figure 3.2: Comparison of total oil flow rate in different days of 2019.

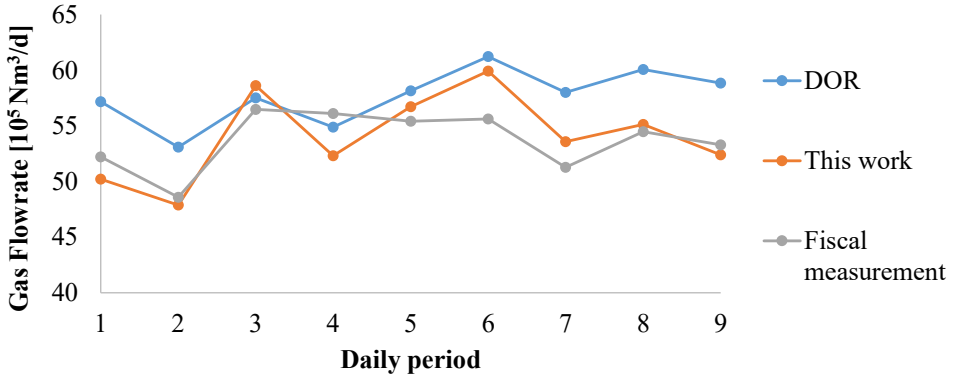

Figure 3.3: Comparison of total gas flow rate in different days of 2019.

The results obtained with the proposed method for the total oil and gas flow rates, shown in Figures 3.2 and 3.3, are in good agreement with the DOR and fiscal measurement data. Moreover, the water flow rate available in the DOR were compared with the results obtained using the proposed method. The results for this variable are shown in Figure 3.4.

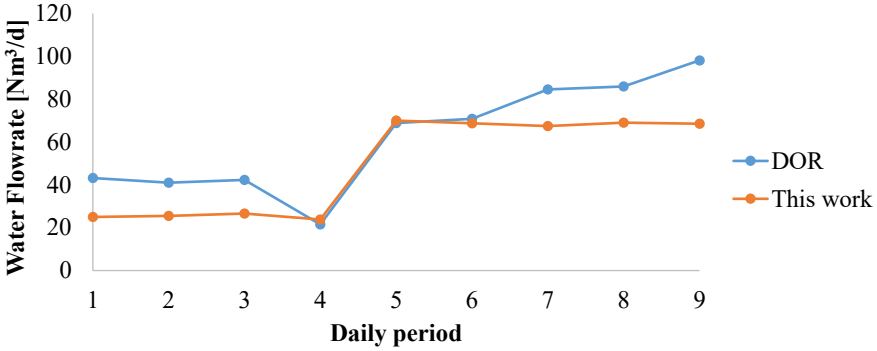

Figure 3.4: Comparison of total water flow rate in different days of 2019.

The total oil and gas flow rates were compared to those presented by fiscal meters from a specific daily period. The results comparing these values are presented in Figures 3.5 and 3.6. An hourly moving average due to the oscillations of the fiscal measurement data was plotted.

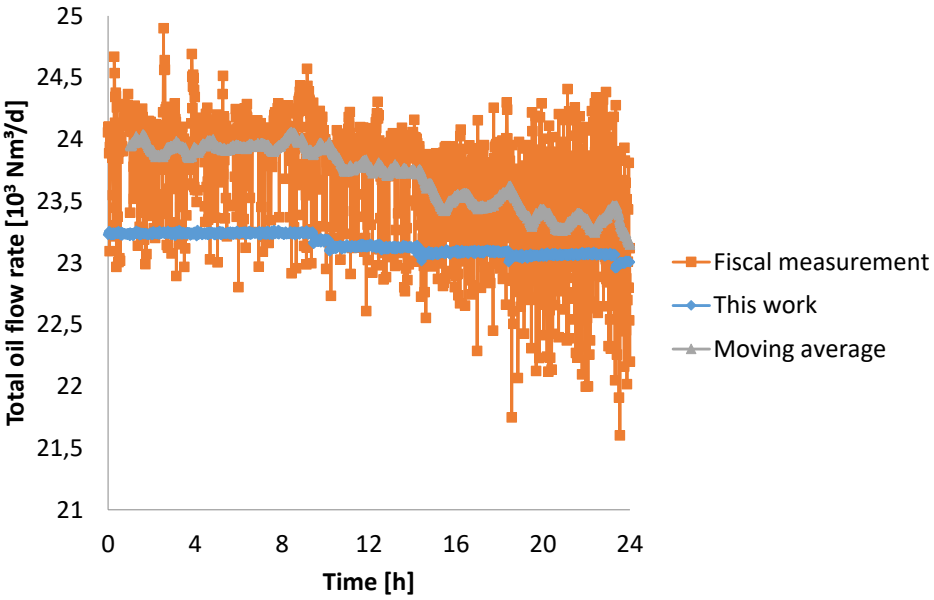

Figure 3.5: Total oil flow rate of a pre-salt plataform from November 1st at 5PM to November 2nd at 5PM at every second.

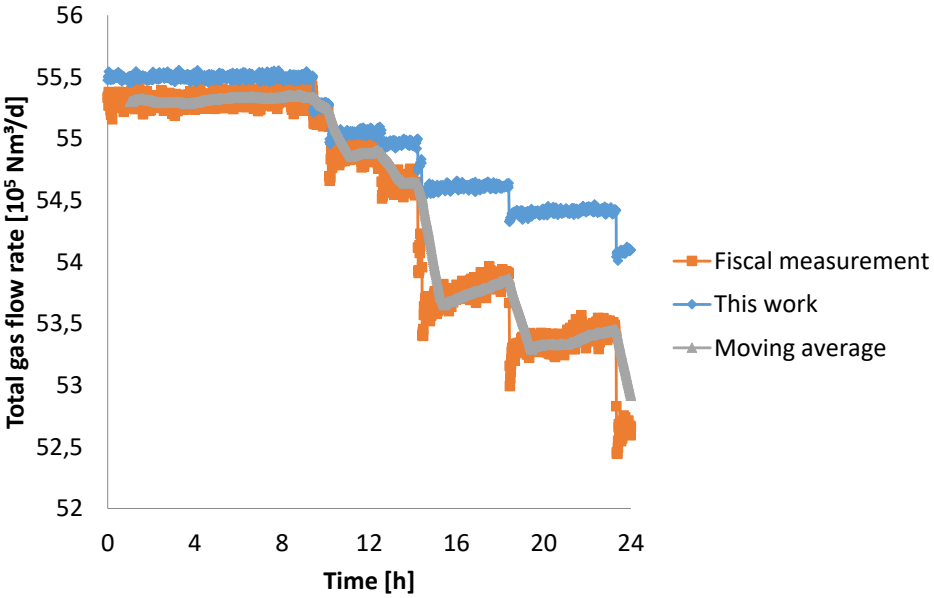

Figure 3.6: Total gas flow rate of a pre-salt plataform from November 1st at 5PM to November 2nd at 5PM at every second.

The results obtained with the proposed method showed good agreement with the fiscal measurement data for both oil and gas flow rates. In Figure 3.6, there is

a notable decrease of the total gas flow rate along the hours, which is compatible with the behavior of one well of this platform at this period, as shown in Figure 3.7.

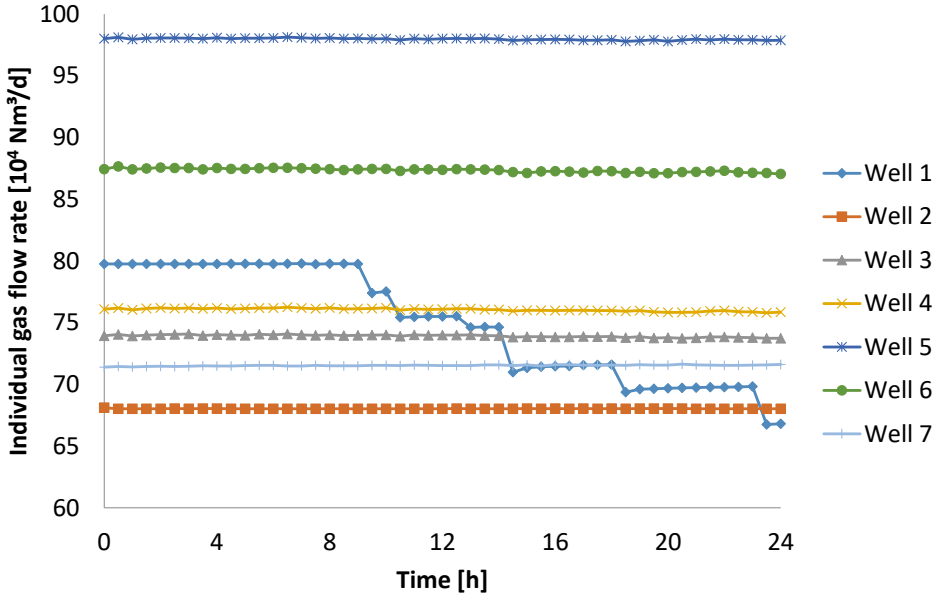

Figure 3.7: Individual gas flow rate of each well of a pre-salt plataform from November 1st at 5PM to November 2nd at 5PM at every second.

The relative error between the results of this work and the flow rates provided by fiscal meters is also evaluated, using Equation 5.29. Figure 3.8 shows the results of this evaluation.

$$PRE = \frac{Q^{meas} - Q^{pred}}{Q^{meas}} \times 100 \tag{3.45}$$

where Q^{meas} is the total flow rate given by the fiscal meters and Q^{pred} is the total flow rate calculated by the proposed method.

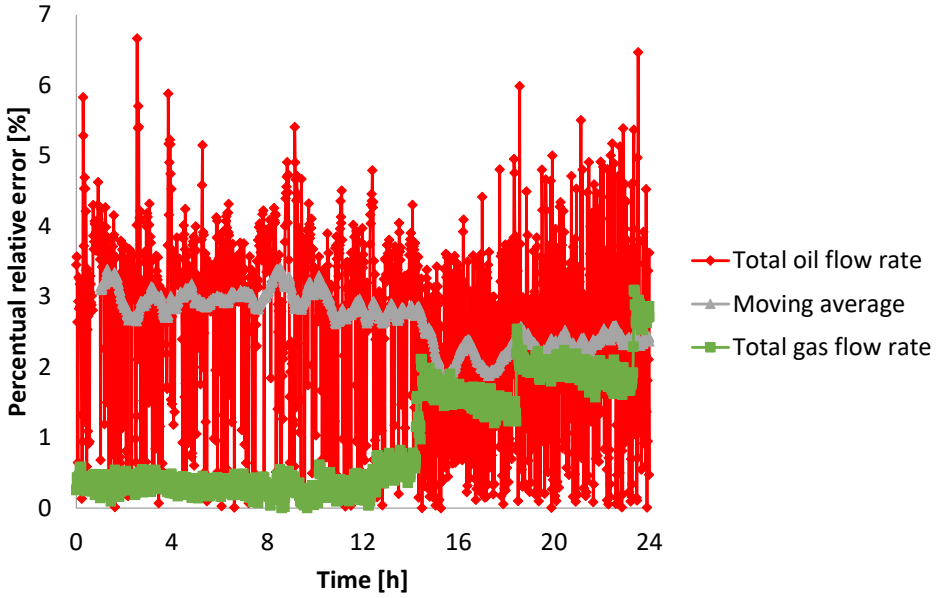

Figure 3.8: Percentual relative error between the predicted flow rates and the provided by fiscal meters, for a 24 hours period.

As presented in Figure 3.8, the percentual relative errors are below 3% for the total gas flow rate. Regarding the errors for the total oil flow rate, there are oscillations throughout the period of the data, which do not exceed 7%. An hourly moving average for the error related to the total oil flow rate was plotted in Figure 3.8, which is below 3.5%.

Also, it was calculated the square of the Pearson product moment correlation coefficient that indicates how accurate is the model prediction using Equation 3.46.

$$R^2 = \left(\frac{\sum \left(Q^{meas} - \overline{Q^{meas}}\right)\left(Q^{pred} - \overline{Q^{pred}}\right)}{\sqrt{\sum \left(Q^{meas} - \overline{Q^{meas}}\right)^2 \sum \left(Q^{pred} - \overline{Q^{pred}}\right)^2}} \right)^2 \tag{3.46}$$

where $\overline{Q^{pred}}$ is the mean of the total flow rate given by the fiscal meters and $\overline{Q^{meas}}$ is the mean of the total flow rate calculated by the proposed method.

In this work, R^2 is equal to 0.97, which means that the model can accurately predict the plant data.

3.4 Partial Conclusions

This chapter presented a method capable of calculating the individual flow rates of producing wells, to replace flow measuring devices by virtual flow meters.

With the flow rate of each well, it is possible to calculate the total flow rate produced by the platform. Since plant data information about individual wells flow rates were not available due to the absence of measuring devices, the model validation of the proposed method was performed by comparing the calculated total field flow rate calculated and the total flow rate provided by Daily Operation Reports and fiscal meters.

In the periods selected for validation purposes, the results obtained by the mathematical model were able to follow the variations observed in the DOR and fiscal meters. For a period of 24 hours, relative errors between the predicted flow rates and the provided by fiscal meters were below 3.5% and 3% for the total oil and gas flow rates, respectively. Therefore, it is possible to conclude that the results provided by the virtual flow meter proposed in this work are in good agreement with the DOR and fiscal measurement data.

Chapter 4

Improvement of Black Oil Delumping Method Applied to an Offshore Oil Field

Black oil delumping, also known as a stream conversion method, converts a black oil wellstream into a compositional wellstream. This procedure ensures consistent flowrate allocations and monitoring of the well's performance. This method requires volumetric oil and gas flowrates given in well-test reports, an equation of state model, and additional black oil information reported in the Well Test, PVT Analysis, and Gas Chromatographic Analysis. In this chapter, an improvement on the method to convert black oil data into compositional wellstream is proposed. The method's performance was tested using data of three wells of a platform from an offshore oil field. This improvement significantly increased the accuracy of the method by decreasing the maximum percentage relative error from 16.50% to 4.44% when comparing the calculated and measured oil and gas properties for Well 1, for example. The method also preserves the gas and oil ratio reported in the well tests.

4.1 Introduction

The black oil delumping converts black oil wellstream into a compositional one providing accurate information needed for surface industrial processes. This procedure ensures consistent flowrate allocations and monitoring the well's performance (HODA *et al.*, 2017; HODA and WHITSON, 2013; HOFFMANN *et al.*, 2017). However, black oil data are still important because it requires less computational effort in multiphase flow simulations (GHORAYEB and HOLMES, 2005).

The first delumping method that uses an appropriate equation of state (EoS) and well test data was suggested by WHITSON and SUNJERGA (2012). The method requires the gas composition from the three-phase separator, API measurements, an accurate initial estimate of the separator's feed composition, well test data, and temperature and pressure at which volumetric flowrates were measured. A gamma distribution model was used to fit the oil API gravity reported in the Well Test Report.

HODA and WHITSON (2013) presented a method to convert surface volumetric flowrates of oil and gas given in well tests into compositional wellstreams. The method requires an EoS, an initial estimate of composition (called "seed composition" by the authors), volumetric flowrates (given in the Well Tests), and temperature and pressure at which volumetric flowrates were measured. The authors did not describe how to obtain the initial composition, but they stated that the seed composition is not crucial to the method's accuracy if the Gas-Oil Ratio (GOR) does not change significantly over time. Otherwise, seed composition needs to be updated. The method was applied to Liquid-Rich Shale Reservoirs found in North America.

HODA *et al.* (2017) stated that the seed composition becomes important when wellstream composition presents a significant amount of light and intermediate components that vary over time due to gas-lift injection or processes that require an accurate estimate of wellstream composition, for example. The authors proposed the compositional reservoir for the initial estimate of composition, an iterative method to fit the oil API gravity measured in the field to a gamma function, and a linear model to match the gas specific gravity measured in the field.

HOFFMANN *et al.* (2017) slightly modified the procedure described in HODA and WHITSON (2013) because the available Well Test Report informed neither the volumetric oil flowrate at separator conditions nor the shrinkage factor. The authors computed the oil molar flowrates at standard conditions and modeled the depressurization process accounting for the gas molar flowrates at standard and separator conditions. HOFFMANN *et al.* (2017) also presented the results of applying the delumping method in the oil field called Nile Delta Complex.

CARLSEN *et al.* (2019) used the methods presented in WHITSON and SUNJERGA (2012) and HODA and WHITSON (2013) to predict wellstream compositions based on the available data: GOR, separator temperature and pressure, $^{\circ}API$, and gas and oil composition at separator conditions. The EoS-based methods were successfully used to predict the wellstream composition of a large set of PVT experiments performed on the fluid produced in the Eagle Ford Field with GORs ranging

from 200 to 300 scf/bbl. The objective of that work was to develop a tool to optimize EOR (enhanced oil recovery) strategies in the Eagle Ford Field.

CARLSEN *et al.* (2020b) compared three black oil delumping methods described by WHITSON and SUNJERGA (2012), HODA and WHITSON (2013), and HOFFMANN *et al.* (2017). In conclusion, the authors stated that the accuracy of the different methods relies on the amount and quality of the well-test data and how accurate the EoS describes the phases at defined temperature, pressure, and composition conditions. Afterward, CARLSEN and WHITSON (2020) used the methods summarized in CARLSEN *et al.* (2020b) to calculate the daily wellstream composition and then quantify the daily separator shrinkage factor because the reports did not provide this information. CARLSEN *et al.* (2020a) summarized the black oil delumping methods by characterizing them as a function of the regression variables and available data. Then these authors used the method proposed by HOFFMANN *et al.* (2017) as the first step of a method to normalize the condensate-gas ratio (CGR).

Here, an improvement in converting black oil data into a compositional wellstream is proposed and evaluated using data of three wells from an offshore oil field. The method requires an EoS and accurate well-test data (including GOR, °API, gas specific gravity, and temperature and pressure separator conditions). The volume translation method was applied to the EoS for the liquid phase to enhance the method's accuracy. There are two main differences between the method proposed in this work and the previous methods. Firstly, the proposed method fully describes how to obtain the initial estimate of composition, different from the methods of WHITSON and SUNJERGA (2012), HODA and WHITSON (2013), HODA *et al.* (2017), and HOFFMANN *et al.* (2017). Also, in this work, the fitting parameter is the molar mass of the pseudocomponents of the oil stream used to estimate the initial estimate of composition. In the method proposed by HODA *et al.* (2017) the fitting parameter is the mass molar of the pseudocomponent of the initially estimated composition. It was proven that this improvement on the method significantly increased its accuracy by decreasing maximum relative errors from 16.50% to 4.44% for Well 1, for example.

4.2 Delumping Method

In order to use real plant data for fluid flow compositional simulation, an improved method to transform a black oil wellstream into a compositional wellstream is proposed. The first step of this method is to estimate an initial composition

for the mixture. The composition of the vapor stream that comes out from the separator is given by the Gas Chromatographic Analysis, and the oil properties given in the PVT Analysis were used to calculate the oil stream that comes out from the separator through the Gamma-Distribution Model. Given the vapor and oil stream composition, the global mass balance and the mass balance of each component i at the separator, as shown by Equations 4.1 and 4.2, were used to calculate the global composition of the mixture.

$$F = L + V \tag{4.1}$$

$$Fz_i = Lx_i + Vy_i \tag{4.2}$$

where F, L, and V are the mass flow rates of the mixture, liquid stream, and vapor stream, respectively, z_i is the global composition of component i, and x_i and y_i are liquid and vapor compositions, respectively, of component i.

Equation 4.2 can be rearranged as shown by Equation 4.3.

$$z_i = x_i \frac{L}{F} + y_i \frac{V}{F} \tag{4.3}$$

The Gamma-Distribution Model with three parameters (η, λ, and $M_{C_{11+}}$) is used to describe the distribution of the pseudocomponents, as shown by Equation 4.4, and detailed in WHITSON and BRULÉ (2000). The continuous distribution $P(M)$ is transformed into pseudocomponents mole fractions by dividing the area under the $P(M)$ curve into N_p sections, where N_p is the number of pseudocomponents.

$$P(M) = \frac{(M-\eta)^{\lambda-1} \exp\{-[(M-\eta)/\beta]\}}{\beta^{\lambda}\Gamma(\lambda)} \tag{4.4}$$

where Γ is the gamma function, and β is given by Equation C.22.

$$\beta = \frac{M_{C_{11+}} - \eta}{\lambda} \tag{4.5}$$

According to WHITSON and BRULÉ (2000), η can be considered the lowest value of molar mass among the pseudocomponents, and $M_{C_{11+}}$ is the average molar mass of the pseudocomponents. The value of the parameter λ ranges from 0.5 to 2.5. In this work, λ was chosen to be equal to 0.5 since its value does not significantly affect the results. η was chosen equal to 142.28, which is the value of the molar

mass of the heaviest component among the light and intermediate components. The parameter $M_{C_{11+}}$ was used to fit the measured $^{\circ}API$ using the bisection algorithm.

The second step of the method starts with the calculation of the pure component properties of each pseudocomponent, given the molar mass of each component using the correlations given in Table 4.1. For the light and intermediate components, the properties of the pure components given by DAUBERT and DANNER (1997) were used.

Table 4.1: Correlations for pseudocomponent properties

$P^c_{C_{11+_i}}$	KESLER and LEE (1976)
$T^c_{C_{11+_i}}$	KESLER and LEE (1976)
$T^b_{C_{11+_i}}$	SOREIDE (1989)
$\omega_{C_{11+_i}}$	EDMISTER (1958)
$v^c_{C_{11+_i}}$	HALL and YARBOROUGH (1971)

Next, using the estimate of the initial composition of the mixture from the previous step, a flash calculation, using the Peng-Robinson EoS (PR EoS) (ROBINSON *et al.*, 1985) is carried out at standard condition. Then, the molar flowrate of each component i in the oil and gas phases at standard condition, respectively, n_{oi} and n_{gi}, are calculated as shown by Equations 4.6 and 4.7.

$$n_{oi} = x_i^{SC} \frac{Q_o^{SC}}{v_o^{SC}} \tag{4.6}$$

$$n_{gi} = y_i^{SC} \frac{Q_g^{SC}}{v_g^{SC}} \tag{4.7}$$

where the superscript SC hereafter means at standard conditions, x_i^{SC} and y_i^{SC} are the mole fractions of component i in the oil and gas phases, respectively; Q_o^{SC} and v_o^{SC} are the oil volumetric flowrate and molar volume, respectively; and Q_g^{SC} and v_g^{SC} are the gas volumetric flowrate and molar volume, respectively.

MARTIN (1979) showed that the volume translation method improves the volumetric capabilities of the cubic EoS. This method consists of applying a correction term to the molar volume of the liquid phase calculated by the EoS, as shown by Equation 4.8.

$$v_o^{SC} = v_o^{EoS} - \sum_{i=1}^{N} x_i b_i s_i \tag{4.8}$$

where v_o^{EoS} is the oil molar volume calculated by the EoS, x_i is the oil mole fraction of component i, b_i is the EoS repulsion parameter of the pure component i, and s_i is the volume-shift parameter of component i.

The volume-shift parameter for the pure components is shown in Table 4.2 (WHITSON and BRULÉ, 2000) and is evaluated by Equation 4.9 for the pseudo-components (JHAVERI and YOUNGREN, 1988).

Table 4.2: Volume-shift parameter of the pure components (WHITSON and BRULÉ, 2000)

Component	s_i
Nitrogen	-0.1927
Carbon dioxide	-0.0817
Methane	-0.1595
Ethane	-0.1134
Propane	-0.0863
i-Butane	-0.0844
n-Butane	-0.0675
i-Pentane	-0.0608
n-Pentane	-0.0390
n-Hexane	-0.0080
n-Heptane	0.0033
n-Octane	0.0314
n-Nonane	0.0408
n-Decane	0.0655

$$s_i = 1 - 2.258/M_i^{0.1823} \tag{4.9}$$

where M_i is the molar mass of the pseudocomponent i.

The total molar flowrate of each component i (n_i), given by Equation 4.10, is used to restore the molar composition of the mixture, as shown in Equation 4.11.

$$n_i = n_{oi} + n_{gi} \tag{4.10}$$

$$z_i = \frac{n_i}{\sum_{i=1}^{N} n_i} \tag{4.11}$$

Given this adjusted molar composition of the mixture, the following variables

of interest (GOR, $^{\circ}API$, and γ_g) are calculated, as shown in Equations 4.12-4.14, for comparison with experimental data.

$$^{\circ}API = \frac{141.5}{\rho_o^{SC}/\rho_w^{SC}} - 131.5 \tag{4.12}$$

$$GOR = \frac{v_g^{SC}\alpha_g^{SC}}{v_o^{SC}\alpha_o^{SC}} \tag{4.13}$$

$$\gamma_g = \frac{\rho_g^{SC}}{\rho_{air}^{SC}} \tag{4.14}$$

where ρ_o^{SC} and ρ_w^{SC} are the oil and water densities; v_o^{SC} is the oil molar volume; ρ_{air}^{SC} is the air density; $\alpha_g^{SC} = V/F$ and $\alpha_o^{SC} = L/F$ are the gas and oil phase mole fractions.

The proposed method is fully described in the workflow shown in Figure 4.1.

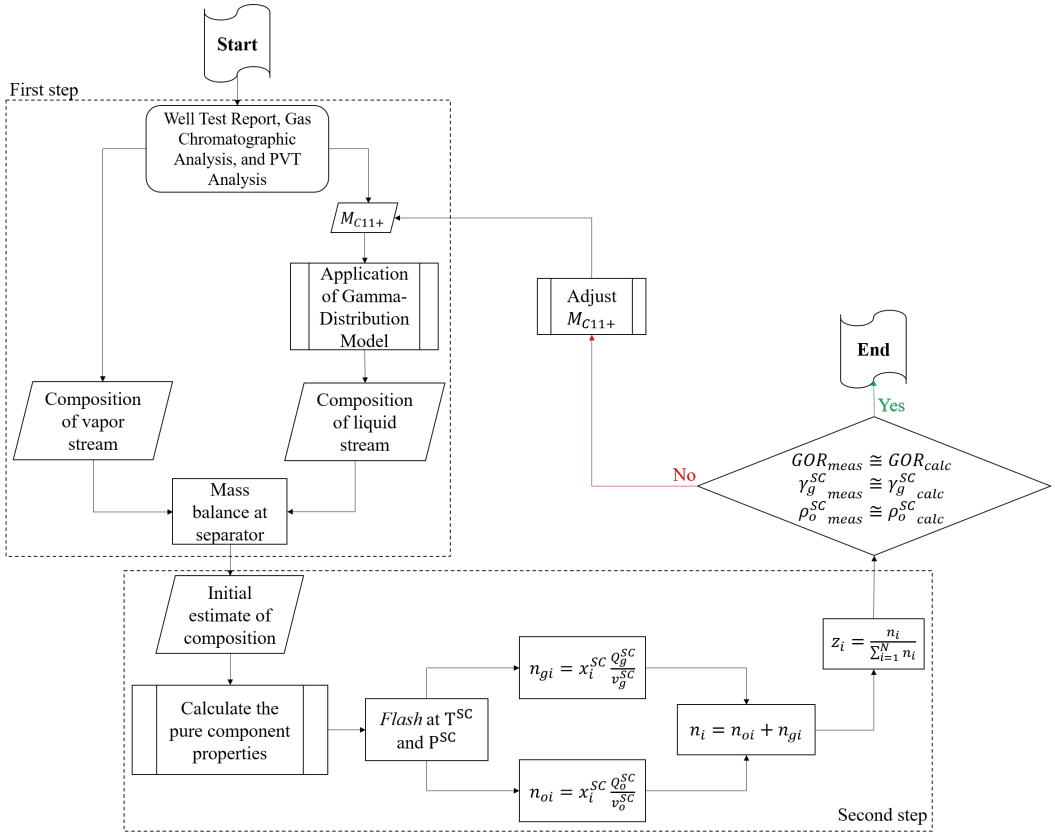

Figure 4.1: Proposed black oil delumping method.

The proposed black oil delumping method results are shown in Section 4.3.

For comparison, the first step of the proposed workflow, shown in Figure 4.1, was used to calculate the initial estimate of composition used for the methods proposed by HODA and WHITSON (2013) and HODA *et al.* (2017). Because the

parameter $M_{C_{11+}}$ is needed in the first step of the workflow to predict the initial estimate of composition, this parameter was calculated using four different correlations proposed by: (1) LASATER (1958), (2) CRAGOE (1929), (3) STANDING (1974), and (4) EILERTS (1947). The correlations 1 and 3 calculated the initial estimate of composition that showed the highest and lowest percentual relative errors, respectively, when comparing the measured and calculated GOR, $^{\circ}API$, and γ_g. Therefore, two initial estimates of composition, composed of 14 light and intermediate components and 8 pseudocomponents, were generated for each set of data given in the Well Test Reports for the correlations 1 and 3 used to calculate $M_{C_{11+}}$.

In the method proposed by HODA and WHITSON (2013), the wellstream composition is calculated following Equations 4.6, 4.7, 4.10, and 4.11. This methodology does not require any iterative method. HODA and WHITSON's method is described in the workflow shown in Figure 4.2. In this case, there is no adjusting parameter.

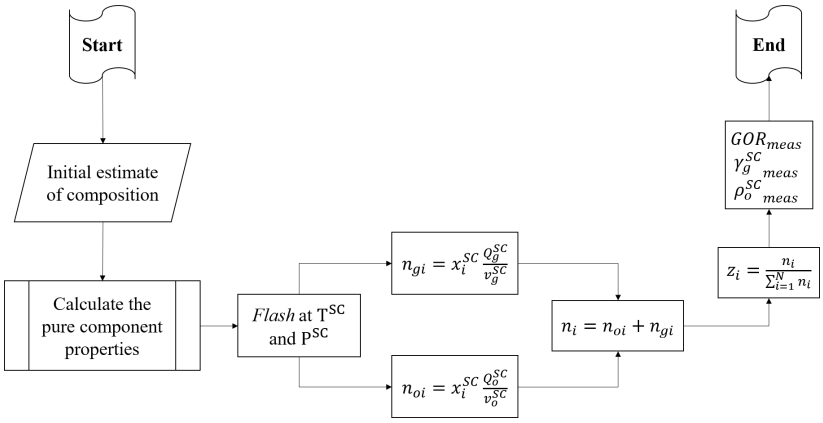

Figure 4.2: Black oil delumping method proposed by HODA and WHITSON (2013).

HODA *et al.* (2017) proposed the application of the Gamma Distribution Model, given by Equations 4.4 and C.22, the initial estimate composition and the average molar mass of the pseudocomponents adjusted to fit the measured $^{\circ}API$ using the bisection algorithm. η was considered the lowest value of molar mass among the pseudocomponents, and $M_{C_{11+}}$ was calculated using Equation 4.15. The authors state that the application of this iterative method approximates the calculated $^{\circ}API$ with those reported in the Well Test Reports. Then, the wellstream composition is calculated following Equations 4.6, 4.7, 4.10, and 4.11. The method proposed by HODA *et al.* (2017) is described in the workflow shown in Figure 4.3.

$$M_{C_{11+}} = \sum_{i=1}^{N_p} z_{C_{11+i}} M_{C_{11+i}} \tag{4.15}$$

where $z_{C_{11+}i}$ and $M_{C_{11+}i}$ are the mole fraction and molar mass of the pseudocomponent i, respectively.

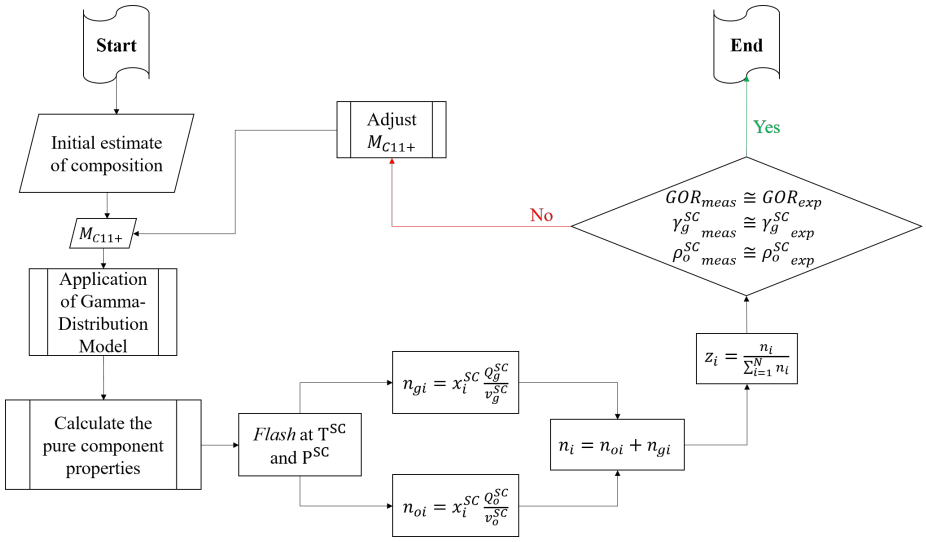

Figure 4.3: Black oil delumping method proposed by HODA *et al.* (2017).

Figure 4.4 shows the flowchart of the offshore oil production field used in this work. The test manifold line is used to perform the Well Test Report of each well. In this case, just the well that will be tested is directed to the test manifold line using the 3-way ball valve. The other wells keep flowing through the production manifold line. The gas and oil flow meter of the test manifold line is used to measure each well flow rate provided in the Well Test Report.

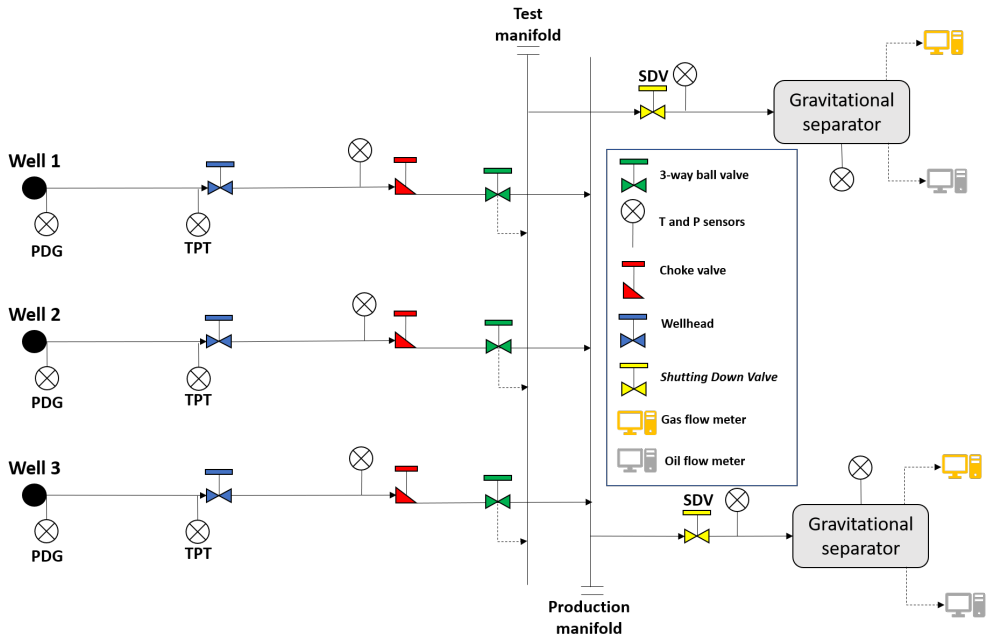

Figure 4.4: Flowchart of the offshore oil production field.

4.3 Results and Discussion

The black oil data were converted into a compositional wellstream using the proposed improved delumping method. Then the results were compared with those presented by the method described in HODA and WHITSON (2013) and HODA *et al.* (2017). It was used the black oil data given in Well Test Reports, PVT Analysis, and Gas Chromatographic Analysis of three wells from different days from an offshore oil production field. The API of the oil samples, considering all the wells, ranges from 28 to 35. Thus, the improvement on the black oil delumping method proposed is applicable for light and medium oils.

Tables 4.3, 4.4, and 4.5 shows the results of PRE (percentual relative error) between the measured and calculated γ_g, GOR, and $^\circ API$ for Well 1, 2, and 3, respectively, for different samples of oil collected during the Well Tests using the method presented in HODA and WHITSON (2013) and HODA *et al.* (2017) when calculating $M_{C_{11+}}$ using the correlation given by STANDING (1974), and the method proposed in this work.

The percentage relative error (PRE) is calculated by Equation 5.29.

$$PRE = \frac{\Omega_i^{meas} - \Omega_i^{calc}}{\Omega_i^{meas}} \times 100 \tag{4.16}$$

where Ω_i^{meas} and Ω_i^{calc} are the measured and calculated values of the variable Ω, respectively, in the Well Test Report i.

Table 4.3: PRE for the results of Well 1 using the method presented in HODA and WHITSON (2013) and HODA *et al.* (2017) when calculating $M_{C_{11+}}$ using the correlation given by STANDING (1974), and the method proposed in this work

	PRE (%)								
	HODA and WHITSON (2013)			HODA *et al.* (2017)			This work		
	STANDING (1974)								
	γ_g	GOR	$^\circ API$	γ_g	GOR	$^\circ API$	γ_g	GOR	$^\circ API$
1	-0.73	-8.02×10^{-7}	10.80	-1.56	-3.08×10^{-5}	16.20	-0.90	-2.70×10^{-7}	0.15
2	1.01	-7.05×10^{-7}	6.13	0.17	-4.45×10^{-5}	10.90	1.00	-1.96×10^{-7}	-0.44
3	-0.58	-1.01×10^{-6}	11.10	-1.45	-3.89×10^{-5}	16.50	-0.75	-3.08×10^{-7}	-0.16
4	1.22	-7.37×10^{-7}	10.08	0.19	-5.21×10^{-5}	14.50	1.10	-7.63×10^{-8}	-0.86
5	-0.12	-8.74×10^{-7}	9.89	-0.96	-3.79×10^{-5}	15.10	-0.23	-2.61×10^{-7}	-0.12
6	0.45	-7.60×10^{-7}	10.72	-0.48	-4.04×10^{-5}	15.51	0.30	-1.70×10^{-7}	-0.18
7	4.33	4.46×10^{-6}	5.85	2.71	-2.83×10^{-4}	8.97	4.44	4.33×10^{-6}	1.03
8	-0.54	-9.57×10^{-7}	9.50	-1.34	-3.83×10^{-5}	15.05	-0.75	-1.81×10^{-7}	-4.25
9	-0.97	-8.47×10^{-7}	9.56	-1.66	-3.03×10^{-5}	15.38	-1.07	-2.96×10^{-7}	-0.35
MPRE	0.45	-2.48×10^{-7}	9.29	-0.49	-6.63×10^{-5}	14.24	0.35	-2.86×10^{-7}	-0.57

Table 4.4: PRE for the results of Well 2 using the method presented in HODA and WHITSON (2013) and HODA *et al.* (2017) when calculating $M_{C_{11+}}$ using the correlation given by STANDING (1974), and the method proposed in this work

	PRE (%)								
	HODA and WHITSON (2013)			HODA *et al.* (2017)			This work		
	STANDING (1974)								
	γ_g	GOR	$^\circ API$	γ_g	GOR	$^\circ API$	γ_g	GOR	$^\circ API$
1	-1.53	-1.90×10^{-6}	13.97	-3.20	-6.82×10^{-5}	18.61	-1.75	-5.22×10^{-5}	4.36
2	3.02	-5.15×10^{-7}	1.42	1.40	-1.52×10^{-4}	5.54	3.06	1.87×10^{-8}	-0.92
3	-0.61	-1.53×10^{-6}	2.66	-1.75	-5.09×10^{-5}	7.52	-0.62	-1.16×10^{-6}	-0.28
4	5.46	3.49×10^{-6}	-3.92	4.03	-1.28×10^{-4}	-1.02	5.35	2.77×10^{-6}	2.23
5	-0.51	-1.34×10^{-6}	2.98	-1.58	-4.73×10^{-5}	7.88	-0.52	-1.03×10^{-6}	0.23
6	0.41	-1.28×10^{-6}	0.72	-0.70	-6.10×10^{-5}	5.25	0.42	-7.82×10^{-7}	-3.03
7	-0.15	-1.63×10^{-6}	2.04	-1.31	-6.26×10^{-5}	6.84	-0.14	-1.16×10^{-6}	-1.12
MPRE	0.87	-6.72×10^{-7}	2.84	-0.45	-8.15×10^{-5}	7.23	0.83	-7.65×10^{-6}	0.21

Table 4.5: PRE for the results of Well 3 using the method presented in HODA and WHITSON (2013) and HODA *et al.* (2017) when calculating $M_{C_{11+}}$ using the correlation given by STANDING (1974), and the method proposed in this work

	PRE (%)								
	HODA and WHITSON (2013)			HODA *et al.* (2017)			This work		
	STANDING (1974)								
	γ_g	GOR	$^\circ API$	γ_g	GOR	$^\circ API$	γ_g	GOR	$^\circ API$
1	5.06	2.12×10^{-6}	1.39	3.42	-1.89×10^{-4}	4.94	5.02	1.71×10^{-6}	3.24
2	-1.33	-1.62×10^{-6}	5.27	-2.43	-4.58×10^{-5}	10.55	-1.39	-7.14×10^{-7}	-3.85
3	-1.39	-1.58×10^{-6}	4.74	-2.46	-4.80×10^{-5}	10.05	-1.44	-6.23×10^{-7}	-4.73
4	1.63	-8.90×10^{-7}	2.75	0.46	-6.48×10^{-5}	7.13	1.64	-6.14×10^{-7}	0.56
5	3.26	-1.83×10^{-7}	2.10	1.82	-1.16×10^{-4}	6.07	3.29	1.13×10^{-7}	0.20
6	-2.47	-1.64×10^{-6}	6.89	-3.53	-4.13×10^{-5}	12.54	-2.55	-8.35×10^{-7}	-1.38
7	-2.49	-1.64×10^{-6}	6.97	-3.53	-4.18×10^{-5}	12.72	-2.57	-8.29×10^{-7}	-1.31
MPRE	0.33	-7.67×10^{-7}	4.30	-0.89	-7.81×10^{-5}	9.14	0.28	-2.56×10^{-7}	-1.04

For comparison, the initial estimate of composition was predicted using two correlations for $M_{C_{11+}}$: LASATER (1958) and STANDING (1974). The correlation proposed by LASATER (1958) provided a higher average molar mass of the pseudo-components when compared to the one proposed by STANDING (1974). The higher the $M_{C_{11+}}$, the heavier the oil, and the lower the $^\circ API$. This lower $^\circ API$ deviated the predicted value from the measured value when using the correlation proposed by LASATER (1958) to calculate the initially estimated composition. The PREs between the measured and calculated $^\circ API$ for Wells 1, 2, and 3 using the correlation given by LASATER (1958) are higher when compared to the one given by STANDING's correlation using both the method proposed by HODA and WHITSON (2013) and HODA *et al.* (2017), presenting a significant systematic deviation from experimental data. Regarding the percentual relative errors between the measured and calculated γ_g and GOR, HODA and WHITSON and HODA *et al.*'s methods showed good accuracy for both correlations, LASATER (1958) and STANDING (1974), and for Wells 1, 2, and 3. The PRE for the results of Well 1 using the method presented

in HODA and WHITSON (2013), and HODA *et al.* (2017) when calculating $M_{C_{11+}}$ using the correlation given by LASATER (1958) is given in Appendix G, Table G.15. This step of the method is important because it can affect the final stream composition when calculating the molar mass of the pseudocomponent of the oil stream for the initial estimate of composition using two different correlations. For example, when using the method proposed by HODA and WHITSON (2013) and the correlation proposed by STANDING (1974) to calculate the molar mass of the pseudocomponent, the PRE between the measured and calculated fluid properties for Well 1 was around 10%, as shown by Table 4.3, yet when using the correlation proposed by LASATER (1958) the PRE was around 50%, as shown in Appendix G, Table G.15.

As observed in Tables 4.3, 4.4, and 4.5, the calculated GOR matches the measured GOR reported in the Well Test Reports when using the proposed method. Figures 4.5, 4.6, and 4.7 show the results of the method proposed here by comparing the measured and calculated γ_g, GOR, and $^\circ API$ for Wells 1, 2, and 3. From Tables 4.3-4.5 and Figures 4.5-4.7, it can be concluded that the composition of the mixture calculated using the improved method reproduced with higher accuracy the measured $^\circ API$ and γ_g given in the Well Test Reports, showing PREs below 5% for all wells, when comparing to the methods proposed by HODA and WHITSON (2013) and HODA *et al.* (2017). Thus it can be stated that the improvement on the black oil delumping method significantly increased its accuracy.

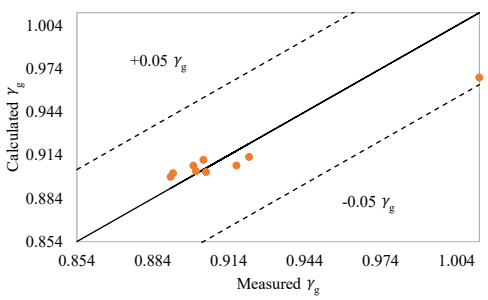

(a) Well 1

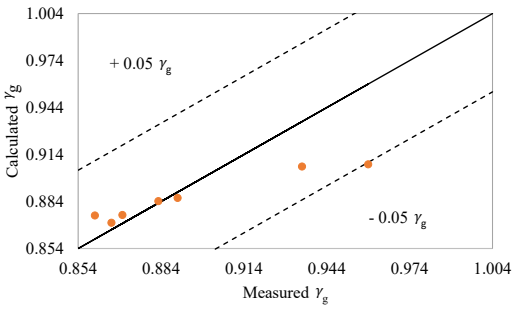

(b) Well 2

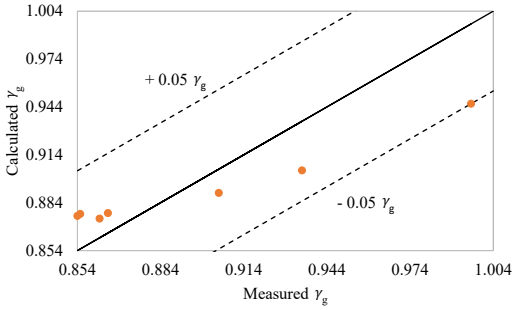

(c) Well 3

Figure 4.5: Comparison of γ_g for Wells 1, 2, and 3: measured vs. calculated using the method proposed in this work.

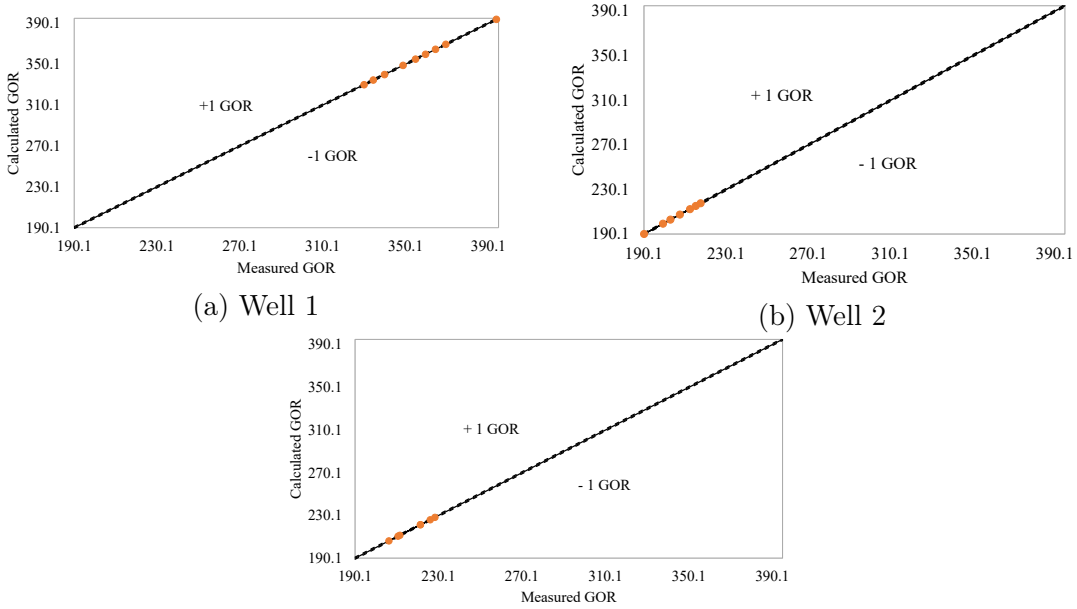

(a) Well 1

(b) Well 2

(c) Well 3

Figure 4.6: Comparison of GOR for Wells 1, 2, and 3: measured vs. calculated using the method proposed in this work.

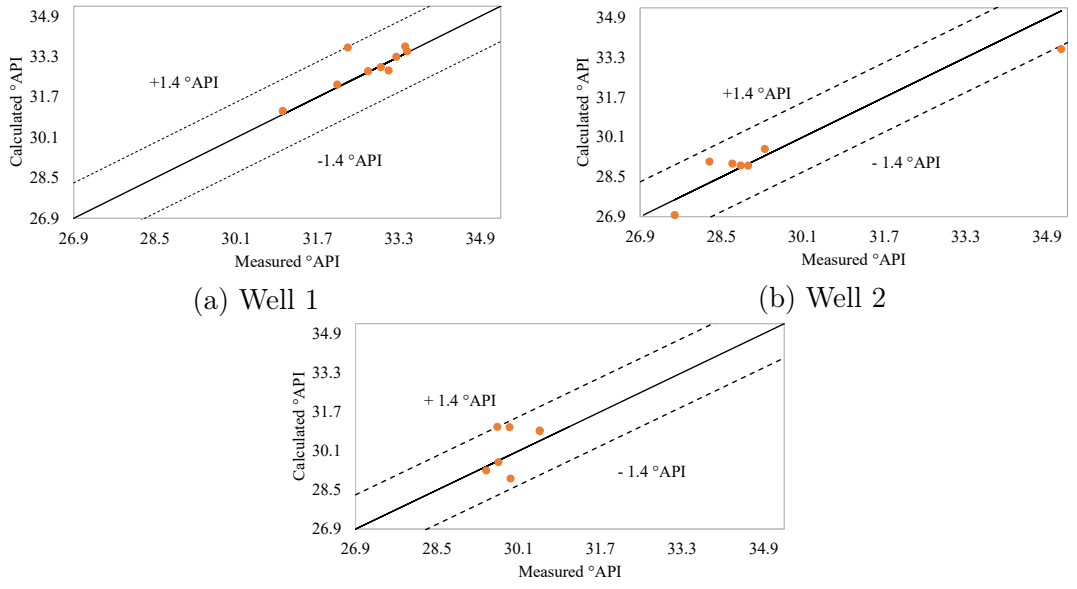

(a) Well 1

(b) Well 2

(c) Well 3

Figure 4.7: Comparison of $^{\circ}API$ for Wells 1, 2, and 3: measured vs. calculated using the method proposed in this work.

In Figures 4.5, 4.6, and 4.7, the deviation from the diagonal indicates of the degree of inaccuracy of the calculated data, showing that the proposed method has a high degree of accuracy. This statement is confirmed when analyzing the maximum absolute difference between the measured and calculated γ_g, GOR, and $^{\circ}API$, equal to 0.05, 0.1, and 1.4, respectively, using the proposed method.

Table G.1, shown in Appendix G, provides the data given in the Well Test Report, PVT Analysis, and Chromatographic Analysis of Well 1. Regarding the results of the method proposed by HODA and WHITSON (2013), the initial estimate of composition and final wellstream composition, and the molar mass of each component of the mixture for Well 1 when using the correlation proposed by STANDING (1974) and LASATER (1958) to calculate $M_{C_{11+}}$ are given. Regarding the methods proposed by HODA *et al.* (2017), the initially estimated composition and the molar mass of each component after applying the Gamma Distribution Model are given. In addition, the optimum initial estimate of composition, final wellstream composition, and molar mass of each component calculated by the method proposed in this work are given.

4.4 Partial Conclusions

This chapter presented an improved method to convert a black oil wellstream into a compositional wellstream. With the volumetric flowrate of each well, black oil data, and an EoS, it was possible to calculate a compositional wellstream.

There are two main differences between the method proposed in this work and the previous methods. Unlike the literature, the proposed method fully describes how to obtain an initially estimated composition. Also, the molar mass of the pseudocomponent of the oil stream as the fitting parameter significantly increased the accuracy of the method.

The efficiency of the proposed method was tested by comparing with measured GOR, °API, and γ_g given in Well Test Reports, PVT Analysis, and Gas Chromatographic Analysis of three well from an offshore oil production field, showing a high degree of accuracy.

Chapter 5

Multiphase Flow Simulation in Offshore Pipelines: An Accurate and Fast Algorithm Applied to Real-Field Data

This chapter proposes an iterative algorithm to fit a multiphase flow model to measured data from offshore fields to be used in real-time applications. Due to the best compromise between accuracy and computational speed, the Drift-Flux Model was used in the proposed procedure to describe the multiphase flow behavior inside a real offshore production pipeline. The predicted temperature and pressure drops were compared to real-time data to verify the efficiency of the proposed algorithm. The relative errors in the outlet temperature and the inlet pressure between the predicted and real-time data were less than 2.5%. Firstly, Two-Fluid and Drift-Flux model validation and comparison with two well-known software programs were carried out using experimental data. Secondly, a hypothetical production pipeline was used to verify the computational cost and the main fluid flow properties. For comparison, the same fluid, pipeline dimensions, and material properties were also implemented into well-known software.

5.1 Introduction

The oil industry requires the development of models that can accurately estimate, with low computational cost, the properties of fluid flow inside gas and oil production pipelines (ISHII and HIBIKI, 2011). The most widely used models for a

two-phase fluid flow system are the Homogeneous Model (HM) (also called Homogeneous Equilibrium Model), the Drift-Flux Model (DFM), and the Two-Fluid Model (TFM). For example, software such as OLGA® and ALFAsim® use the TFM for fluid flow. Nowadays, software OLGA® belongs to the company Schlumberger, but Statoil was the first one to start to develop this software (BENDIKSEN *et al.*, 1991). Software ALFAsim® belongs to the company ESSS and is still under development (ESSS, 2019).

HIBIKI and ISHII (2003) point out that the TFM can describe in detail the interactions between vapor and liquid phases. This model applies separated continuity equations for the gas and oil phases, coupled through interfacial mass transfer equations. The TFM model implemented in OLGA® rigorously considers three phases, the gas phase, the oil phase, and the oil droplets. This model is composed of three momentum and mass conservation equations (one for each phase) and one energy conservation equation, assuming that all phases are at the same temperature. This yields seven conservation equations and one equation of state for the pressure in the pipeline (SCHLUMBERGER, 2017).

In contrast, software ALFAsim® considers separated continuity equations for four phases: oil, gas, oil droplets, and gas bubbles. This yields four momentum and mass conservation equations and one energy conservation equation, assuming that all phases are at the same temperature, resulting in nine conservation equations (ESSS, 2019).

Both the TFM and DFM were implemented in this work. The TFM, as used here, comprises two momentum, mass, and energy conservation equations (one for each phase, i.e., liquid and gas) and one interfacial balance equation for each conservation equation set. It is assumed that both phases are at the same temperature and pressure. This yields six conservation equations and three interfacial balance equations. As for the DFM, it comprises one mixture mass, momentum, and energy conservation equations and one constitutive kinematic equation. This yields four conservation equations and one constitutive equation (TEIXEIRA and SECCHI, 2017).

This work proposes an iterative algorithm to predict the temperature and pressure drops inside a real gas and oil production pipeline. The goal is to estimate the pipe wall roughness to fit the model to the measured data and then apply it to fluid flow monitoring or flow assurance analysis. Thus, the pressure drop along the pipeline in production is properly predicted, for example, since this parameter affects it directly. As previously stated in the literature (TEIXEIRA and SECCHI, 2017) and later addressed in this work, the DFM presents a good compromise between

accuracy and computational cost for the numerical resolution of the multiphase flow model equations for real-time simulations in offshore pipelines, which are very attractive and desired features for pipeline simulations. To attain such beneficial characteristics and as a contribution of this work, the DFM was adjusted to represent single-phase liquid, whenever all the components are dissolved in the liquid phase, by assuming a volumetric gas fraction equal to zero. Consequently, the slip velocity of the vapor phase in relation to the mixture is zero and the frictional pressure loss is calculated as a function of liquid phase properties. Those adjustments were required because some mixture properties are functions of liquid and vapor phase properties. By assuming a volumetric gas fraction equal to zero, the mixture properties will depend only on the liquid phase properties.

In order to use real-time fluid data, the methodologies developed by GÓES *et al.* (2021) and GÓES *et al.* (2022) were adopted here as they both have already proved reliable. Most of the flow meters installed in real oil fields measure the oil platform's total gas and liquid flow rates. In other words, the result represents the sum of the oil and gas flow rates from all the wells of an oil platform. So, GÓES *et al.* (2021) proposed a methodology divided into two steps to predict the individual gas and oil flow rates of each well connected to an oil platform. Besides, the composition models, used in the Two-Fluid and Drift-Flow models, as well as in the software OLGA® and ALFAsim®, require as input data the fluid composition. Then the methodology proposed by GÓES *et al.* (2022) aims to predict the fluid composition that is being produced by each well as a function of data measured during well tests. Since the present work aims to be used as a tool for fluid flow monitoring in the pipelines, the use of real-field data is required to characterize the fluid composition and flow rate of each phase. The combination of these methodologies along with real-field data is the major contribution of this study.

In order to test and analyze the ideas brought in the last two paragraphs, firstly, a model validation was carried out using experimental data from a small-scale facility. Secondly, a hypothetical gas and oil production pipeline was used to compare the computational cost and the main fluid flow properties. Then, due to the best compromise between accuracy and computational speed for real-time applications, the DFM was used to describe both single-phase and two-phase flow behavior inside a real offshore oil and gas production pipeline. The predicted temperature and pressure drops were compared to real-time data to verify the efficiency of the proposed algorithm. The relative errors in the outlet temperature and the inlet pressure between the predicted and real-time data were less than 2.5%. The results are very promising and show that reliable pipeline simulations are possible as far as accuracy is concerned under the framework proposed.

In this work, the DFM results were compared to data collected at a specific time and date. In most real fields, the temperature and pressure are measured only at the inlet and outlet of the pipelines, so the only available information is the temperature and pressure drops during the fluid flow. For flow assurance analysis, the temperature and pressure values at every pipe section, for example, are required to evaluate wax and hydrate precipitation. This last example makes the algorithm useful for monitoring a flowline in real time.

In the next section, the mathematical modeling and implementation details are described. Section 5.3 describes the three case studies used in this work in detail. Section 5.4 shows the implementation details used in the software ALFAsim® and OLGA®. In Section 5.5, the results of the case studies are discussed, summarizing the main achievements in the last section.

5.2 Methodology

5.2.1 Drift-Flux Model

The DFM was used to describe the two-phase flow inside the pipeline, according to the development proposed by TEIXEIRA and SECCHI (2017), based on ISHII and HIBIKI (2011). Compared to the original equations derived from an average application at DFM three-dimensional version, viscous and Reynolds stresses, covariance terms were neglected, and the time derivatives were neglected assuming steady-state conditions. This model is composed of four conservation equations, one for mixture mass (Equation 5.1), one for mixture momentum (Equation 5.2), one for mixture energy (Equation 5.3), and one for vapor mass (Equation 5.4), in addition to one constitutive kinematic equation (Equation 5.5).

$$\frac{d\left(\rho_m v_m\right)}{dx} = 0 \tag{5.1}$$

$$\frac{d\left[\rho_m (v_m)^2\right]}{dx} = -\frac{dP}{dx} - F_{mw} - \rho_m g\, sin(\theta) - \frac{d}{dx}\left(\frac{\alpha_v \rho_l \rho_v}{\alpha_l \rho_m} \hat{v}_v^{dft^2}\right) \tag{5.2}$$

$$\begin{aligned}\frac{d\left(\rho_m v_m h_m\right)}{dx} =& Q_{fn} - \frac{d}{dx}\left[\frac{\alpha_v \rho_v \rho_l}{\rho_m}\left(h_v - h_l\right)\hat{v}_v^{dft}\right] \\ &+ \left[v_m + \frac{\alpha_v\left(\rho_l - \rho_v\right)}{\rho_m}\hat{v}_v^{dft}\right]\frac{dP}{dx}\end{aligned} \tag{5.3}$$

$$\frac{d\left(\alpha_v \rho_v v_m\right)}{dx} = \Gamma_v - \frac{d}{dx}\left(\frac{\alpha_v \rho_v \rho_l}{\rho_m}\hat{v}_v^{dft}\right) \tag{5.4}$$

$$\hat{v}_v^{dft} = \left\langle \hat{v}_v^{dft} \right\rangle_\alpha + (C_0 - 1)\left\langle j \right\rangle \tag{5.5}$$

where ρ_m, ρ_l, and ρ_v are the density of the mixture, liquid, and vapor phases, respectively; F_{mw} is the frictional pressure loss; v_m is the mixture velocity; θ is the pipeline inclination angle; α_v is the vapor void fraction; h_m, h_v, and h_l are the mixture, vapor, and liquid enthalpies, respectively; Q_{fn} is the heat exchange rate between the fluid and the neighborhood; Γ_v is the vapor mass transfer rate, $\hat{v}_v^{dft}$ is the slip velocity of the vapor phase in relation to the mixture, $\langle j \rangle$ is the mixture superficial velocity; $\left\langle \hat{v}_v^{dft} \right\rangle$ and C_0 are model parameters.

Single-phase liquid flow was considered since all the components are dissolved in the liquid phase for high pressure and temperature conditions. Then, assuming the vapor void fraction equal to zero ($\alpha_v = 0$), the DFM turns into a set of three conservation equations composed of one for liquid mass (Equation 5.6), one for liquid momentum (Equation 5.7), and one for liquid energy (Equation 5.7). Given that, no reference was used to obtain those equations. The set of equations for the DFM and TFM are derived from Euler equations after average process and certain simplifications. Therefore, it is reasonable to state that the single-phase flow equations may be compared to the single-phase compressible Euler equations.

$$\frac{d\left(\rho_l v_l\right)}{dx} = 0 \tag{5.6}$$

$$\frac{d\left[\rho_l (v_l)^2\right]}{dx} = -\frac{dP}{dx} - F_{mw} - \rho_l g\, sin(\theta) \tag{5.7}$$

$$\frac{d\left(\rho_l v_l h_l\right)}{dx} = Q_{fn} + v_l \frac{dP}{dx} \tag{5.8}$$

where v_l is the liquid velocity.

A resolution strategy was developed to consider the transition between single-phase and two-phase flow. The variables F_{mw} and $\hat{v}_v^{dft}$, related to the DFM, were adjusted, as shown by Equations 5.9 and 5.10, to represent the single-phase flow conditions whenever the vaporized mass fraction (β_w) given by the flash algorithm is less than or equal to zero.

$$\hat{v}_v^{dft} = \begin{cases} \left\langle \hat{v}_v^{dft} \right\rangle_\alpha + (C_0 - 1)\left\langle j \right\rangle, & \beta_w > 0 \\ 0, & \beta_w \leq 0 \end{cases} \tag{5.9}$$

$$F_{mw} = \begin{cases} \phi_v^2 \left(\frac{dP}{dx}\right)_v, & \beta_w > 0 \\ \left(\frac{dP}{dx}\right)_l, & \beta_w \leq 0 \end{cases} \tag{5.10}$$

5.2.2 Two-Fluid Model

For comparison purposes, TFM was selected to describe the two-phase flow. This model is composed of six differential equations and three algebraic equations regarding the interfacial balance of the phases. The TFM is divided into two mass (Equations 5.11 and 5.12), two momentum (Equations 5.13 and 5.14), and two energy (Equations 5.15 and 5.16) conservation equations, in addition to one interfacial mass (Equation 5.17), momentum (Equation 5.18) and energy balance equation (Equation 5.19) (HIBIKI and ISHII, 2003).

$$\frac{d(\alpha_l \rho_l v_l)}{dx} = -\Gamma_v \tag{5.11}$$

$$\frac{d(\alpha_v \rho_v v_v)}{dx} = \Gamma_v \tag{5.12}$$

$$\frac{d(\alpha_l \rho_l v_l^2)}{dx} = -\alpha_l \frac{dP}{dx} - \alpha_l \rho_l \sin(\theta) - F_{lw} - \Gamma_v v_{li} + F_i - F_{MV} \tag{5.13}$$

$$\frac{d(\alpha_v \rho_v v_v^2)}{dx} = -\alpha_v \frac{dP}{dx} - \alpha_v \rho_v \sin(\theta) - F_{vw} + \Gamma_v v_{vi} - F_i + F_{MV} \tag{5.14}$$

$$\frac{d(\alpha_l \rho_l v_l h_l)}{dx} = -\Gamma_v h_l + Q_{lw}(1-\gamma_l) + \alpha_l v_l \frac{dP}{dx} \tag{5.15}$$

$$\frac{d(\alpha_v \rho_v v_v h_v)}{dx} = \Gamma_v h_v + Q_{vw}(1-\gamma_v) + \alpha_v v_v \frac{dP}{dx} \tag{5.16}$$

where F_{MV} is the virtual mass force; γ_l and γ_v are the fraction of the heat exchanged with the wall that results in heat transfer, Q_{lw} and Q_{vw}, respectively; F_i is the frictional and interfacial drag volumetric force; v_{li} and v_{vi} are the liquid and vapor interfacial velocities; α_l is the liquid void fraction; F_{lw} and F_{vw} are the friction volumetric forces; θ is the inclination angle, and P is the mixture pressure, respectively. The interfacial balance equations are shown in Equations 5.17-5.19.

$$\Gamma_l + \Gamma_v = 0 \tag{5.17}$$

$$-\Gamma_v v_{li} + \Gamma_v v_{vi} = 0 \tag{5.18}$$

$$-\gamma_v Q_{vw} - \gamma_l Q_{lw} + \Gamma_v (h_v - h_l) = 0 \tag{5.19}$$

The heat exchanged between the phases and the wall, Q_{lw} and Q_{vw}, are calculated as shown in Equation 5.20 (ISL, 2001).

$$Q_{fn} = \begin{cases} Q_{lw}, & \Gamma_v > 0 \\ Q_{vw}, & \Gamma_v < 0 \end{cases} \tag{5.20}$$

Variables γ_l and γ_v are calculated based on the value of Γ_v, as shown in Equations 5.21 and 5.22, which use the energy interfacial balance equation (ISL, 2001).

$$\gamma_l = \begin{cases} \frac{\Gamma_v(h_l - h_v)}{Q_{lw}}, & \Gamma_v > 0 \\ 0, & \text{otherwise} \end{cases} \tag{5.21}$$

$$\gamma_v = \begin{cases} \frac{\Gamma_v(h_l - h_v)}{Q_{vw}}, & \Gamma_v < 0 \\ 0, & \text{otherwise} \end{cases} \tag{5.22}$$

The interfacial average velocities, v_{li} and v_{vi}, are described by Equation 5.23 (ISL, 2001).

$$v_{vi} = v_{li} = v_i = \begin{cases} v_l, & \Gamma_v > 0 \\ v_v, & \Gamma_v < 0 \end{cases} \tag{5.23}$$

For this model, a fluid flow regime map (MANDHANE *et al.*, 1974) was used to calculate the frictional and interfacial drag volumetric force, F_i, and the virtual mass force is given by ISL (2001). It should be emphasized that MANDHANE *et al.*'s map is only valid for horizontal flows, and thus, rigorously speaking, would not apply to inclined sections, as the riser. This map was only used in these simulations, with the TFM, for illustration purposes and should be replaced for real applications when applying the proposed algorithm for flow assurance analysis and fluid flow monitoring, for example. Nevertheless, the results obtained using this map agree with experimental data, as shown in the next section.

5.2.3 Complementary Modeling

The heat exchange between the fluid and its neighborhood is described by Equation 5.24.

$$Q_{fn} = 4\frac{U_{heat}(T_{neigh} - T)}{ID} \tag{5.24}$$

where U_{heat} is the overall heat transfer coefficient, ID is the inner diameter of the pipe and T_{neigh} is the neighborhood (seawater) temperature.

The vapor mass generation rate is evaluated by Equation 5.25. The deduction of this expression is shown by GOES *et al.* (2019).

$$\Gamma_v = \rho_m v_m \frac{d\beta_w}{dx} \tag{5.25}$$

where β_w is the vaporized mass fraction.

In the Drift-Flux Model, the model parameters ($\left\langle \hat{v}_v^{dft} \right\rangle$ and C_0) are flow-pattern dependent. BHAGWAT and GHAJAR (2014) developed a set of correlations to calculate these parameters as a function of pipe diameter and inclination angle, fluid properties, liquid, and vapor flow rates, and vapor void fraction. Thus, there is no flow pattern concern regarding the Drift-Flux Model. According to these authors, the set of correlations was tested against 8255 experimental data points from 60 different papers measured over a wide range of pipe inclination angles, pressures, and vapor void fractions. The results showed the applicability of the correlations to the different flow patterns.

Before calculating the vapor and liquid fluid properties, a flash calculation was performed using the Peng-Robinson equation of state (PR EoS) (ROBINSON *et al.*, 1985) to calculate the liquid-vapor equilibrium. This results in an iterative procedure at each discretized point at a given temperature, pressure, and fluid composition. The iterative method uses the Rachford-Rice equation for its resolution (RACHFORD and RICE, 1952). As a result of the flash calculation, the β_w is predicted as a function of the fluid temperature, pressure and global composition, as shown in Equation C.22.

$$\beta_w = \beta_w(T, P, z) \tag{5.26}$$

The calculation of liquid and vapor phase enthalpies was performed using the residual properties via PR EoS, which is recommended by DAUBERT and DANNER (1997). The liquid and vapor densities were also evaluated by the PR EoS (RIAZI, 2005), and the liquid and vapor viscosities were given by LOHRENZ *et al.* (1964).

The properties of the pure components were obtained from the Multiflash Software (INFOCHEM, 2017) for P_c, T_c, and V_c, which are the critical pressure, temperature, and volume, respectively; MM the molar mass; w the acentric factor; and P_{ch} the number of Parachor, used to evaluate the interface tension DAUBERT and DANNER (1997).

The DFM and TFM were implemented in the computational environment MATLAB R2020b, with the differential-algebraic equations approach already discussed (GOES *et al.*, 2019; TEIXEIRA and SECCHI, 2017), and solved by the DASSLC routine extended for MATLAB as provided by SECCHI (2012), which uses a BDF method (Backward Differentiation Formula method) (BRENAN *et al.*, 1987). The absolute and relative tolerances for the numerical resolution of the problem were set to 10^{-8} and 10^{-6}, except for the transition region from single-phase to

two-phase flow where these tolerances were loosened to 10^{-1} to improve convergence.

5.3 Case Studies

5.3.1 Model validation

The DFM and TFM models, and softwares ALFAsim® and OLGA® validations were performed by using experimental data given in MUKHERJEE (1979). For each experiment, liquid superficial velocity, and pipe inclination angle was fixed, and the vapor mass flow rate was varied to cover the entire flow pattern map. The pipe length equals 9.3m. It was considered as liquid and vapor phases, kerosene or lube oil, and air, respectively. At each experiment, temperature, pressure, flow pattern, and vapor void fraction were measured.

For predicting the experimental data using DFM and TFM, and softwares ALFAsim® and OLGA®, isothermal flow was considered. This yields cancellation of the mixture, and liquid and vapor mixture conservation equations from the DFM and TFM, respectively. It was adopted as fluid temperature, the temperature measured in the experiments. Also, correlations to calculate liquid and vapor phases properties are required, as given by MUKHERJEE (1979).

5.3.2 Case study - hypothetical gas and oil production pipeline

The hypothetical offshore oil pipeline evaluated in this study is represented in Figure 5.1. The pipeline starts at the wellhead and is separated into four sections, with dimensions and inclinations shown in Table 5.1.

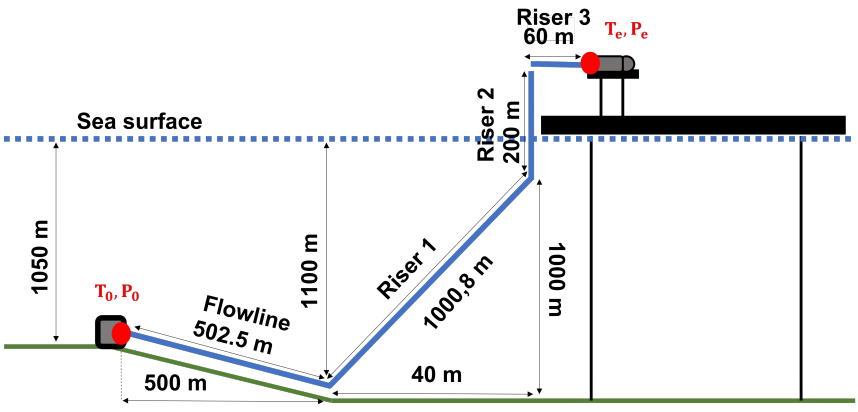

Figure 5.1: Schematic of the hypothetical offshore oil pipeline.

Table 5.1: Pipeline geometry.

Section	**x** [m]	**y** [m]	**Elevation** [m]	**Length** [m]	**Angle** [°]
flowline	500	-1,100	-50	502.494	-5.71
riser - section 1	540	-100	1,000	1,000.8	87.71
riser - section 2	540	100	200	200	90
riser - section 3	600	100	0	60	0

In order to simulate a hypothetical fluid, a volatile oil was adapted from a mixture found in WHITSON and BRULÉ (2000) with composition (in mole fraction) presented in F and a mass flow rate equal to 15 kg/s. The fluid contains ten real components and one pseudocomponent. The pure component properties of the fluid were the same used in Multiflash® Software, and their values are listed in Table F.1 in F.

The pipeline dimensions and properties of its material are given in Tables 5.2 and 5.3, respectively. The wall roughness of the pipe is equal to 2.8×10^{-5} m, the same value used by NEMOTO *et al.* (2010).

Table 5.2: Pipeline section dimensions.

Flowline internal diameter	0.14 m
Flowline and riser thickness	0.0075 m
Riser internal diameter	0.1016 m
Flowline insulation thickness	0.015 m

Table 5.3: Pipeline material properties.

	Density (kg/m^3)	Specific heat ($J/kg/K$)	Thermal conductivity ($W/m/K$)
Flowline and riser	7850	500	50
Insulation	1000	1500	0.135

The parameter U_{heat} was calculated using Fourier Law (INCROPERA *et al.*, 2002). The values of this property are listed in Table 5.4. T_{neigh} was set to $6°C$.

Table 5.4: U_{heat} of the pipeline sections.

Flowline	5.4694 $W/m^2/K$
Riser	6.9763 $W/m^2/K$

5.3.3 Case study - real offshore gas and oil production pipeline

The real offshore gas and oil production pipeline is represented by the geometry given in Figure 5.2. The dimensions of each pipeline section, and U_{heat} and T_{neigh} values of Well 1 are listed in Table F.3 in F. Since information about the pipe material was not available, the pipe wall roughness was used as the same for the hypothetical gas and oil production.

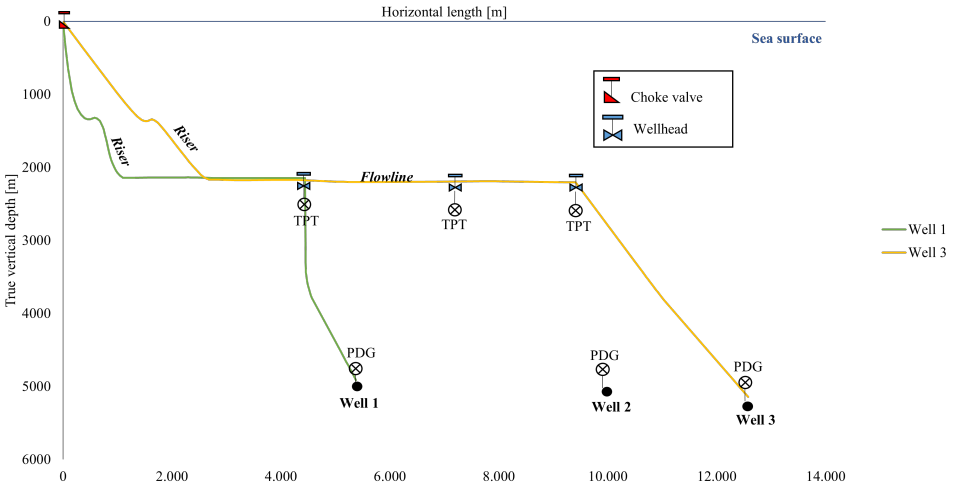

Figure 5.2: Pipeline geometry.

In order to simulate a real fluid, the improvement on the delumping methodology proposed by GÓES *et al.* (2022) was used. The method generates compositional fluid data based on the black-oil data given in the Well Test Report, Gas Chromatographic Analysis, and PVT Analysis. As a result of the delumping procedure, the compositional fluid contains fourteen real components and eight pseudocomponents. The physical properties of the real components were the same used in Multiflash® software, and the properties of the pseudocomponents were calculated. The fluid composition and pure component properties are shown in Table F.2 given in F.

The liquid and gas flow rates that are being produced by each well were predicted using the methodology proposed by GÓES *et al.* (2021). The method consists of predicting the liquid and gas flow rates of each well as a function of real-time data, choke valve specifications, and fluid properties. The mass flow rate that is being produced by each well is given in Table 5.5.

Table 5.5: Mass flow rate produced by Wells 1 and 2.

Well	W_l (kg/s)	W_g ($\times 10^{-5}$) (kg/s)
1	55.28	3.61
2	47.96	4.81

Figure 5.3 describes the algorithm used in this work for the third case study. First, real-field data are collected representing the flowchart's first step. The second step includes the methodology proposed by GÓES *et al.* (2021) used to predict the individual gas and liquid flow rates of each well. In parallel, the third step is the methodology proposed by GÓES *et al.* (2022) used to predict the composition of the fluid produced by each well. As a fourth step, pressure and temperature measured at the choke inlet and wellhead, respectively, are used as boundary conditions in the simulations. In the fifth step, DFM is used to simulate the fluid flow behavior. The TFM may be used in this step, but the computational cost would increase with minor improvement in the accuracy. In the sixth step, pressure and temperature collected at the choke inlet and wellhead, respectively, in real time are used as a source of comparison in the next step. In the seventh step, the algorithm end if the objective function is not satisfied, otherwise the MATLAB tool "fmincon" is used to adjust the pipe wall roughness in the eighth step. The objective function is given in Equation 5.27.

$$F_{obj} = \left|P_{exp}^{wh} - P_{calc}^{wh}\right| + \left|T_{exp}^{choke} - T_{calc}^{choke}\right| \tag{5.27}$$

where P_{exp}^{wh} and P_{calc}^{wh} are the pressures collected in real time and calculated by the DFM, respectively, at the wellhead; and T_{exp}^{choke} and T_{calc}^{choke} are the temperatures collected in real time and calculated by the DFM, respectively, at the inlet of the choke valve.

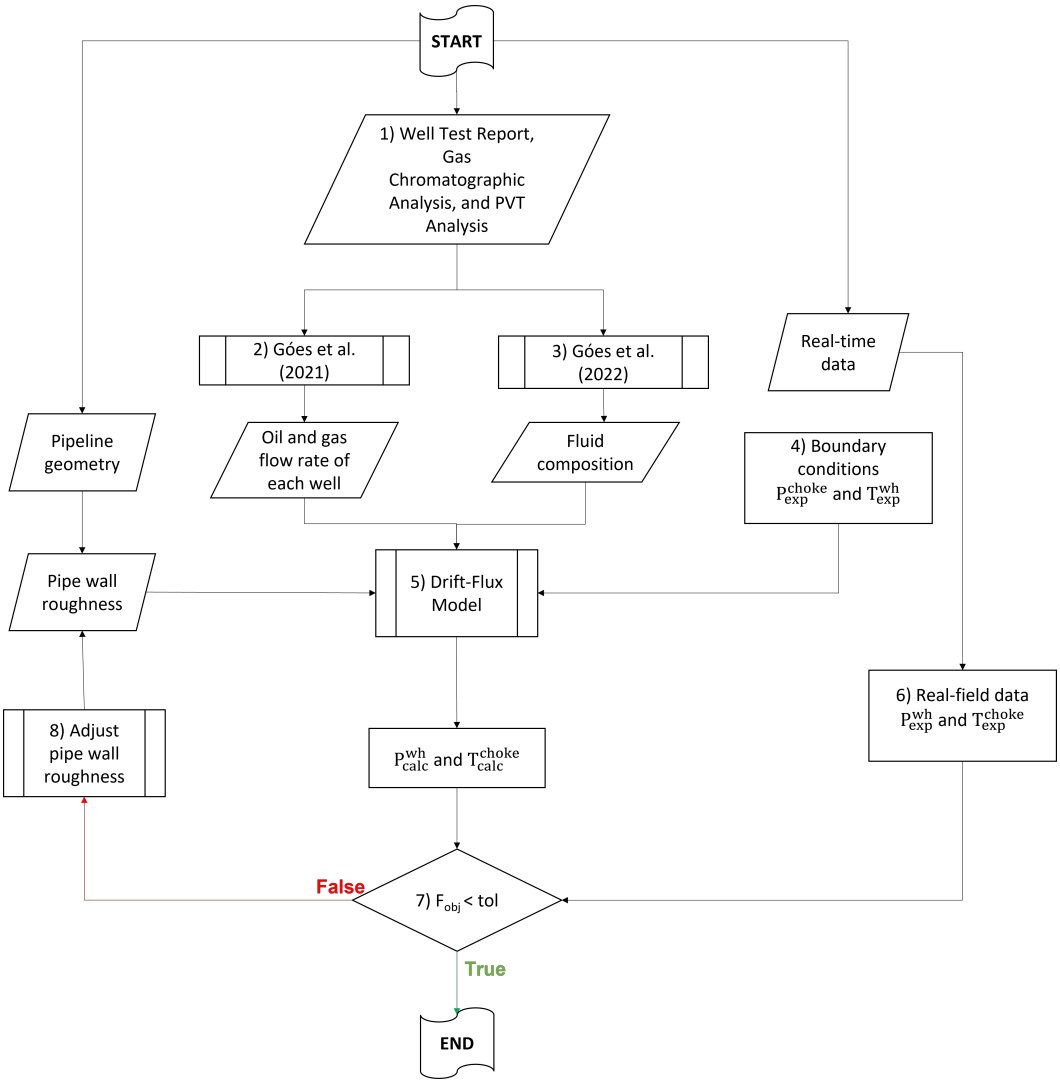

Figure 5.3: Flowchart of the iterative algorithm proposed to first characterize the oil and then to fit a multiphase flow model to measured data from offshore oil field. The pipe wall roughness was used as the fitting parameter.

5.4 Modeling with OLGA® and ALFAsim®

The pipeline dimensions and material properties were implemented in software OLGA® and ALFAsim®. The thermal property, U_{heat} was inserted into these software for each pipeline section.

The software Multiflash® was used to generate the volatile oil and real fluid with the same composition as shown in Appendix F, using the PR EoS as the thermodynamic model, the Lohrenz-Bray-Clark model for viscosity (LOHRENZ *et al.*, 1964), and the two-phase Macleod-Sugden method for the surface tension (DAUBERT and DANNER, 1997). The same methods were used to calculate the liquid surface tension and viscosity required to solve the DFM. The liquid viscosity

is not a direct variable of the DFM, but this transport property is used to calculate the DFM parameters (C_0 and $\left\langle \hat{v}_v^{dft} \right\rangle_\alpha$).

The output of the Software Multiflash® is used in OLGA® and ALFAsim® to evaluate the thermodynamic and transport properties by interpolation. In contrast, in the TFM and DFM models used in this work, these properties are directly assessed with their models.

5.5 Results and Discussion

5.5.1 Model Validation

In this section, the accuracy of the DFM, TFM, OLGA®, and ALFAsim® is tested against a set of experimental data that depends on the liquid used (kerosene or lube oil), pipe inclination (0°, 50°, and 90°), and air flow rate.

Figures 5.4 and 5.5 compare experimental data provided by MUKHERJEE (1979) with simulation results obtained using our approaches (*i.e.*, DFM and TFM), as well as those obtained from OLGA® and ALFAsim®. The experiments were performed on a pipe with a length of 9.3 m, considering the liquid as kerosene or lube oil and the vapor phase as air. It is shown that the behavior of vapor void fraction predicted by the models and software is similar to that observed in the experiments for a wide range of pipe inclinations.

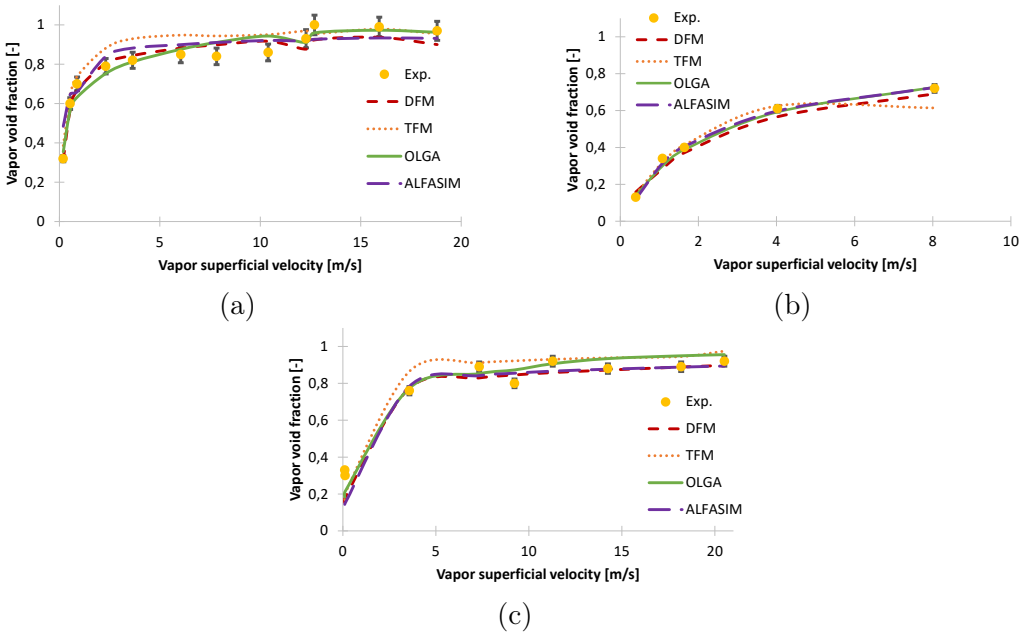

Figure 5.4: Vapor void fraction as a function of the vapor superficial velocities at (a) $\langle j_l \rangle = 0.1074\ m/s$ and $\theta = 50°$, (b) $\langle j_l \rangle = 2.2311\ m/s$ and $\theta = 0°$, and (c) $\langle j_l \rangle = 0.3139\ m/s$ and $\theta = 90°$ for the kerosene as the liquid phase.

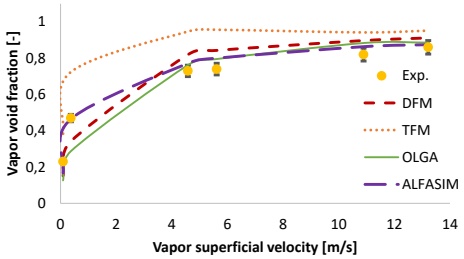

Figure 5.5: Vapor void fraction as a function of the vapor superficial velocities at (a) $\langle j_l \rangle = 0.1097\ m/s$ and $\theta = 0°$ for the lube oil as the liquid phase.

Statistical analyses were performed to analyze the accuracy of the models and software by calculating the mean percentage relative error (MPRE), as shown in Equation 5.28. The results are shown in Table 5.6.

$$MPRE(\%) = \frac{1}{n}\sum_{i=1}^{n}\frac{\alpha_i^{exp} - \alpha_i^{calc}}{\alpha_i^{exp}} \times 100 \tag{5.28}$$

where n is the number of experiments, and α_i^{exp} and α_i^{calc} are the experimental and calculated vapor void fractions, respectively.

Table 5.6: MPRE between the experimental and calculated vapor void fraction for the models and softwares.

	MPRE (%)				**Average**
	Kerosene			**Lube oil**	
	0°	**50°**	**90°**	**0°**	
DFM	11.25	4.97	13.09	17.15	11.62
TFM	7.87	8.58	14.64	34.25	16.34
OLGA®	5.26	5.14	11.82	17.74	9.99
ALFAsim®	3.85	9.06	14.56	8.15	8.91

Table 5.6 shows that DFM is more accurate when compared to the TFM, except for the case in which the pipe inclination equal to zero degrees and kerosene is the liquid phase. As concluded by TEIXEIRA and SECCHI (2017), the fact that the DFM is more accurate than the TFM contrasts the literature, and TFM's exposure to inaccuracies may explain it due to the need for constitutive algebraic equations. Comparing the software OLGA® and ALFAsim® predictions, it is observed that both of them present similar accuracy, as one presents smaller errors in half of the cases and the other in the remaining cases. When comparing the four different approaches, the software ALFAsim® is the most accurate.

5.5.2 Model application to an hypothetical oil pipeline

In this section, a hypothetical fluid at a given flow rate is used to simulate its flow, using DFM and TFM, inside a hypothetical oil and gas production line, and later the results are compared to the results of well-known software proving its capacity of reproducing the steady-state flow behavior inside long production lines. In this specific case, the results are given as a function of axial coordinates to analyze the axial profile of the main fluid properties (fluid temperature and pressure; liquid, and gas densities, etc).

Figures 5.6-5.9 compare the results obtained through DFM and TFM to those obtained from OLGA® and ALFAsim®, showing the axial profiles of temperature and pressure, liquid and gas densities and viscosities, and vapor void fraction, respectively, along the pipeline (Figure 5.1).

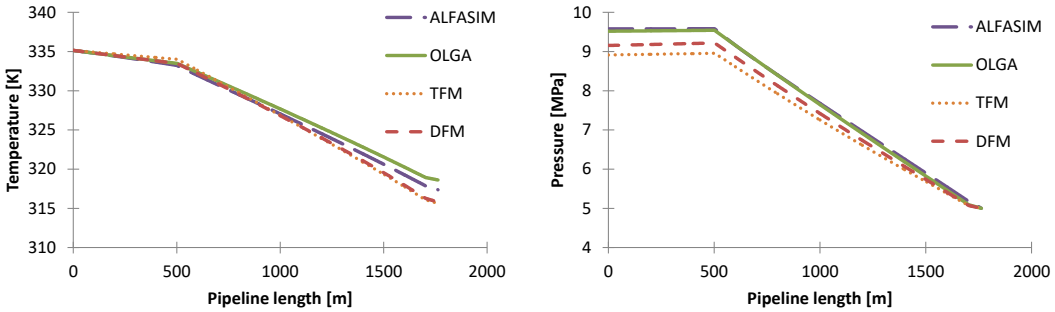

(a) (b)

Figure 5.6: Axial profile of (a) temperature and (b) pressure.

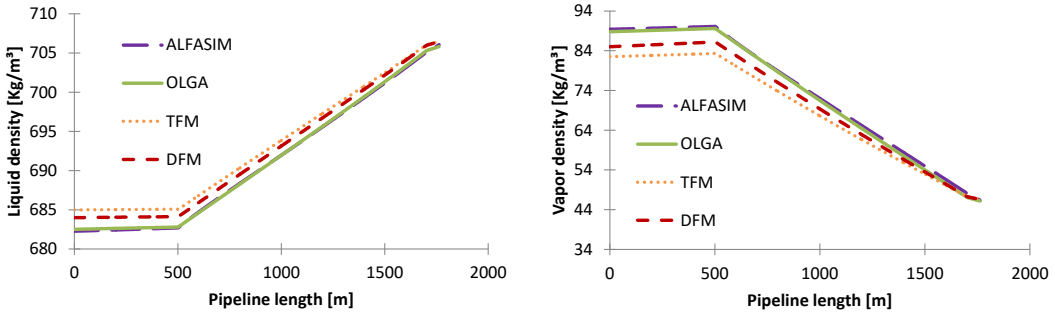

(a) (b)

Figure 5.7: Axial profile of (a) liquid and (b) gas densities.

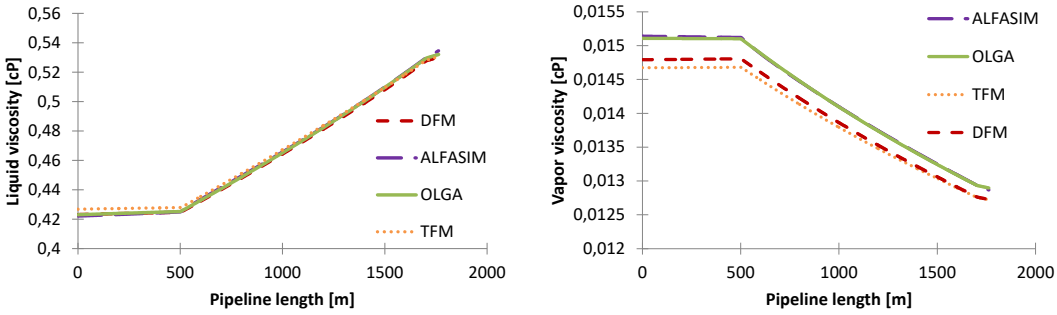

(a) (b)

Figure 5.8: Axial profile of (a) liquid and (b) gas viscosities.

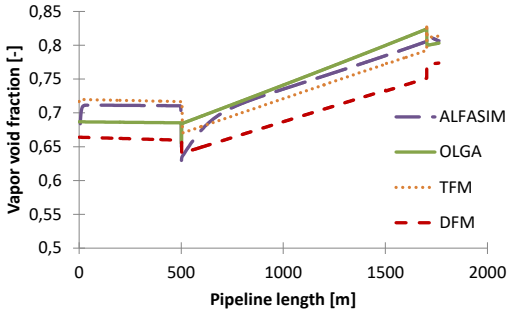

Figure 5.9: Axial profile of vapor void fraction.

Figures 5.6-5.9 show that the results of this work are in good agreement with those provided by OLGA® and ALFAsim®. In Figures 5.6a and 5.6b, the temperature and pressure of the fluid decrease as the fluid flows inside the pipeline. For example, the temperature decreases because of the heat exchange between the fluid and its neighborhood (seawater). The pressure initially increases but decreases mainly due to friction loss and gravitational forces. In the flowline, the pipe is nearly horizontal ($\theta \approx -5^{o}$), the pressure is almost constant, and the temperature drop is low, which causes gas condensation and a slight decrease in vaporized mass fraction. Therefore, other properties remain practically constant, as shown by Figures 5.7-5.9.

In the riser sections (*i.e.*, x > 500m), significant variations in the fluid properties are observed since the pressure and temperature drop are more significant than in the flowline, and these two profiles influence the other variables (i.e., viscosity and density of the liquid and vapor phases and vapor void fraction). Vaporization of light components is characterized by an increase in vapor void fraction (*cf.* Figure 5.9) and the liquid density (*cf.* Figure 5.7a). The gas density decreases (*cf.* Figure 5.7b) due to the pressure drop.

Table 5.7 shows the measured central processing unit (CPU) time of simulation of the DFM and TFM presented in this work. The results show a twice-fold decrease in the simulation time by taking the simulation time of the DFM as a reference. The DFM is computationally less expensive than the TFM because the differential equations in the DFM are based on mixture properties, resulting in a smaller number of differential equations. This shows the superiority of the DFM used in this work implemented in MATLAB as far as the computational time of the simulation is concerned.

Table 5.7: Measured CPU time of simulation

This work - TFM	172 seconds
This work - DFM	67.9 seconds

Merging the conclusion obtained from comparing the experimental data against DFM and TFM, in which the DFM showed to be the most accurate, and the superiority of the DFM regarding the computation time, the DFM was chosen as a fast solver to simulate a real fluid in an offshore pipeline.

5.5.3 DFM simulation in a real offshore gas and oil production pipeline

In this section, the DFM is chosen to simulate a real fluid flow inside a real oil and gas production pipeline. In the end, the results are compared to real-field data from two wells of an oil platform having those two wells' different oil and gas mass flow rates, given in Table 5.5.

Figure 5.10 and Table 5.8 show comparisons between temperature at the inlet of the choke valve and pressure at the wellhead calculated by the DFM and the data collected in real time. In addition, Table 5.8 shows the PRE (percentage relative error), given by Equation 5.29, between the measured and calculated variables. A phase envelope was generated using software Multiflash® to show that at wellhead conditions of temperature and pressure collected in real time the flow is single-phase liquid. The numerical approach used to solve the DAEs of the DFM requires boundary conditions of temperature and pressure to converge the simulation, so the temperature and pressure collected in real time at the wellhead and inlet of the choke valve, respectively, were used as boundary conditions.

$$PRE = \frac{\Omega_i^{meas} - \Omega_i^{calc}}{\Omega_i^{meas}} \times 100 \tag{5.29}$$

where Ω_i^{meas} and Ω_i^{calc} are the measured and calculated values of the variable Ω, respectively.

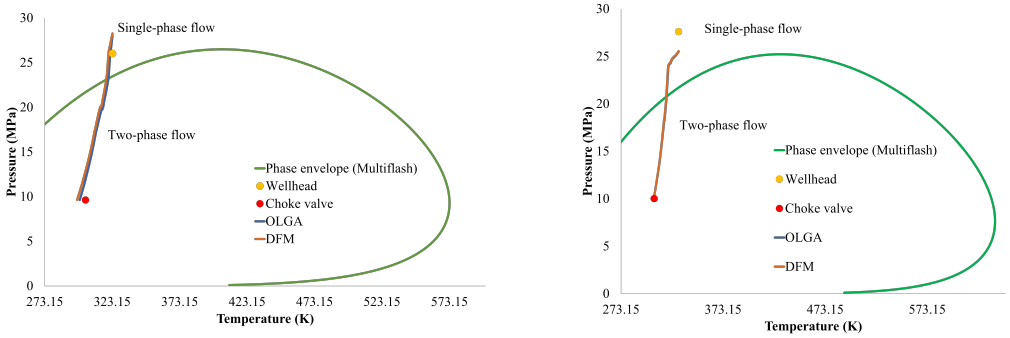

(a) (b)

Figure 5.10: Comparison of the axial temperature and pressure profile calculated by DFM and software OLGA®, and the data measured in real time for Well (a) 1 and (b) 2.

Table 5.8: Comparison between real time data and calculated values at wellhead and inlet of the choke valve.

Well	Temperature (K)				Pressure (MPa)			
	Real time		DFM	PRE (%)	Real time		DFM	PRE (%)
	Wellhead	Choke valve	Choke valve		Wellhead	Choke valve	Wellhead	
1	323.35	303.30	297.08	2.05	26.02	9.62	28.26	-8.61
2	329.55	305.48	305.25	0.07	27.60	10.02	25.54	7.46

It can be observed in Figure 5.10b that the pressure at the wellhead calculated by the DFM is underestimated when compared to real-time data. Concerning Well 1, Figure 5.10a, the DFM overestimates wellhead pressure compared to real-time data. This becomes more evident by analyzing the wellhead pressure collected in real time and the values calculated by the DFM listed in Table 5.8. The difference between the calculated (using the DFM) and real-time pressures at the wellhead are -2.24 and 2.06 MPa for Wells 1 and 2, respectively, resulting in absolute PREs greater than 7%.

The difference in the temperature prediction is not significant. For example, the PRE between the calculated (using the DFM) and real-time temperatures at the inlet of the choke valve are 2.05 and 0.07% for Wells 1 and 2, respectively.

Because the difference in the pressure conditions was more significant than industrial expectation and information about the pipe material was not available, the pipe wall roughness was used as a fitting parameter. The MATLAB function fmincon was used to minimize the objective function given in Equation 5.27.

Figure 5.11 and Table 5.9 show the comparison between the temperature at the inlet of the choke valve and pressure at the wellhead calculated by the DFM using the optimum wall roughness and the data collected in real time. The optimum wall roughness for each well is given in Table 5.10.

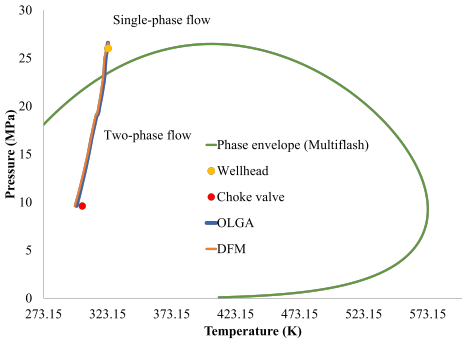

(a)

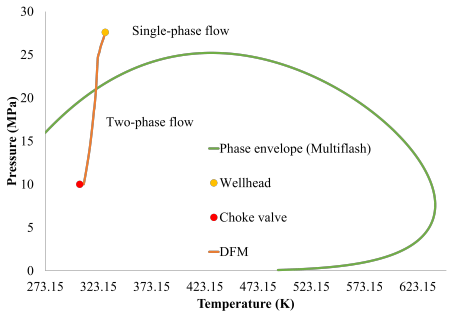

(b)

Figure 5.11: Comparison of the axial temperature and pressure profile calculated by DFM and software OLGA®, and the data measured in real time for Wells (a) 1 and (b) 2 using the optimum wall roughness.

Table 5.9: Comparison between real time data and calculated values at wellhead and inlet of the choke valve using the optimum wall roughness.

Well	Temperature (K)				Pressure (MPa)			
	Real time		DFM	PRE (%)	Real time		DFM	PRE (%)
	Wellhead	Choke valve	Choke valve		Wellhead	Choke valve	Wellhead	
1	323.35	303.30	297.51	1.91	26.02	9.62	26.60	-2.23
2	329.55	305.48	309.24	-1.23	27.60	10.02	27.58	0.07

Table 5.10: Optimum wall roughness for Wells 1 and 2.

Well	Pipe wall roughness (m)
1	2.25×10^{-6}
2	4.37×10^{-4}

Since the pressure drop is proportional to the wall roughness and the pressure calculated by the DFM at the wellhead was overpredicting the real data for Well 1 and underpredicting the real data for Well 2, the optimum wall roughness calculated by the optimization algorithm must be lower for Well 1, and greater for Well 2. This behavior is observed by analyzing the optimum wall roughness for each well given in Table 5.10. Figures 5.10 and 5.11 also present the results of the TFM (from software OLGA®) using the initial pipe wall roughness, $2.8 \times 10^{-5}\ m$ (Figure 5.10), and the estimated value with the DFM (Figure 5.11). As it can be observed in these figures, the results from both models are very close.

It can be observed the improvement of the pressure drop predictions by comparing the PREs given in Tables 5.9 and 5.8. By using the algorithm given in Figure 5.3, the PREs decreased from -8.61% to -2.23% for Well 1. For Well 2, the PRE decreased from 7.46% to 0.07%

5.6 Partial Conclusions

In this work, real-field data are used to validate an innovative iterative algorithm to describe multiphase flow behavior in offshore pipelines. A hypothetical offshore gas and oil production pipeline was used and the results obtained showed very good agreement for the approaches outlined here. Also, it is shown the superiority of the DFM as far as the accuracy and computational speed of the simulation are concerned.

Also, the proposed iterative algorithm, using the pipe wall roughness as a fitting parameter, was applied to a real offshore gas and oil production pipeline. The temperature and pressure drops predicted by the algorithm were compared against real-time data. After adjusting the pipe wall roughness, the results showed a good agreement between the predicted pressure and temperature at the wellhead and choke valve, respectively, and real-time data, and the prediction of the correct number of phases along the pipeline.

The novelty of this work relies on the iterative algorithm proposed to predict the pressure and temperature drop along pipelines which may be later used for flow assurance analysis and fluid flow monitoring, for example. The combination of the methodologies developed by GÓES *et al.* (2021, 2022) and the pipe wall roughness adjustment was essential to the algorithm's success. Also, applying real-case scenarios enhances, even more, the importance of this work.

Chapter 6

General Conclusions and Suggestions for Future Researches

This work proposes procedures for flow assurance analysis, specifically on wax precipitation and fluid flow monitoring. In Chapter 2, a procedure to find the minimum inlet temperature that avoids precipitation was successfully applied to hypothetical gas and oil production pipeline by simulating a hypothetical fluid flow. In order to describe the fluid flow behavior under real-case scenarios, two methodologies were proposed, as described in Chapters 3 and 4. The first methodology proposes a method to predict the individual liquid and gas flow rates of each well. The latter proposes an improvement on the method to convert black oil data into a compositional stream, known as the delumping method. Chapter 5 proposes an iterative algorithm to predict oil behavior during multiphase flow using real-field data, liquid and gas flow rates, and fluid composition from the previous methodologies, under a real-case scenario.

This work successfully provided procedures for flow assurance analysis and fluid flow monitoring that may be applied to real case scenarios. Moreover, it is possible to couple the thermodynamic and multiphase flow models and analyze the effect of different input data on the wax appearance temperature, for example.

6.1 Potential Future Researches

As suggested for future research, firstly, it is recommended to couple the thermodynamic model for wax precipitation modeling, described in Appendix E, with the multiphase flow algorithm under steady-state conditions described in Chapter 5. It is important to emphasize that this procedure is different from the one used in

Chapter 2. Since in the latter, the fluid was composed of only one heavy component; thus the WAT calculated by the thermodynamic model is independent of the model that describes the solid phase. In real-case scenarios, the fluid composition is more complex with many heavy components, so more accurate thermodynamic models describe the solid phase behavior, as the one proposed by COUTINHO *et al.* (2006). As a result of this advice, by coupling the hydrodynamic and thermodynamic models, it is possible to predict the pipeline section where the first wax particle will form in the solution. Given that, flow assurance analysis regarding wax precipitation may be carried out to avoid solid formation in real scenarios.

As an advancement for the algorithm, it is recommended to compare the results of two different models that describe the wax growth, the Equilibrium Model (EM) (SVENDSEN, 1993) and Film Mass Transfer Theory (FMT) (SINGH *et al.*, 2000), against experimental data. Given the most accurate model, the researcher may use the Multiple Solid Solution Model (Appendix E) to predict the solubility curve and input data of the wax growth model. Lastly, by coupling the hydrodynamic model under transient conditions and the wax growth model, the algorithm can inform the wax growth behavior as a function of time.

Bibliography

AIYEJINA, A., PRASAD, D., PILGRIM, A., SASTRY, M. K. S., 2011, "Wax formation in oil pipelines : A critical review", *International Journal of Multiphase Flow*, v. 37, n. 7, pp. 671–694. ISSN: 0301-9322. doi: 10.1016/j.ijmultiphaseflow.2011.02.007.

AMIM, A., 2015, "Evaluation of Commercially Available Virtual Flow Meters". In: *Offshore Technology Conference*, Texas, USA, May. Society of Petroleum Engineers.

BEGGS, D., BRILL, J., 1973, "A Study of Two-Phase Flow in Inclined Pipes", *Journal of Petroleum Technology*, v. 25, n. 05 (Mai), pp. 607–617. ISSN: 0149-2136. doi: 10.2118/4007-PA.

BENDIKSEN, K. H., MAINES, D., MOE, R., NULAND, S., 1991, "The Dynamic Two-Fluid Model OLGA: Theory and Application", *SPE Production Engineering*, v. 6, n. 02, pp. 171–180. doi: 10.2118/19451-pa.

BHAGWAT, S. M., GHAJAR, A. J., 2014, "A flow pattern independent drift flux model based void fraction correlation for a wide range of gas-liquid two phase flow", *International Journal of Multiphase Flow*, v. 59, pp. 186–205. ISSN: 03019322. doi: 10.1016/j.ijmultiphaseflow.2013.11.001.

BIKMUKHAMETOV, T., JASCHKE, J., 2020, "First Principles and Machine Learning Virtual Flow Metering: A Literature Review", *Journal of Petroleum Science and Engineering*, v. 184, pp. 1–26.

BRENAN, K. E., CAMPBELL, S. L., PETZOLD, L. R., 1987, *Numerical Solution of Initial-Value Problems in Differential-Algebraic Equations*. Philadelphia, Society for Industrial and Applied Mathematics. ISBN: 0898713536.

BRILL, J. P., MUKHERJEE, H., 1999, *Multiphase Flow in Wells*. Richardson, Texas, Society of Petroleum Engineering.

CARBONE, L. C., 2007, "Methodology for virtual flow measurement and production optimization". In: *III Seminar on Artificial Elevation and Flow (In portuguese)*, Búzios - RJ.

CARLSEN, M. L., WHITSON, C. H., DAHOUK, M. M., et al., 2019, "Compositional Tracking of a Huff-n-Puff Project in the Eagle Ford". In: *Unconventional Resources Technology Conference*, Denver, Colorado, USA. Society of Petroleum Engineers/American Association of Petroleum Geologists/Society of Exploration Geophysicists. doi: 10.15530/urtec-2019-539.

CARLSEN, M. L., WHITSON, C. H., 2020, "Quantifying Separator Oil Shrinkage". In: *International Petroleum Technology Conference*, Dhahran, Saudi Arabia, Jan. Society of Petroleum Engineers. doi: 10.2523/IPTC-19775-MS.

CARLSEN, M. L., DAHOUK, M. M., HOFFMANN, A., WHITSON, C. H., 2020a, "CGR Normalization-Convert Rates to a Common Surface Process". In: *SPE Canada Unconventional Resources Conference*. SPE, sepa. doi: 10.2118/199982-MS.

CARLSEN, M. L., DAHOUK, M. M., MYDLAND, S., WHITSON, C. H., 2020b, "Compositional Tracking: Predicting Wellstream Compositions in Tight Unconventionals". In: *International Petroleum Technology Conference*, Dhahran, Saudi Arabia, Janb. Society of Petroleum Engineers. doi: 10.2523/IPTC-19596-MS.

CHU, J., SU, H., GAO, F., WU, J., 1998, "Process Control: Art or Practice", *Annual Reviews in Control*, v. 22, pp. 59–72.

COUTINHO, J. A. P., ANDERSEN, S. I., STENBY, E. H., 1995, "Evaluation of Activity Coefficient Models in Prediction of Alkane Solid-Liquid Equilibria", *Fluid Phase Equilibria*, v. 103, pp. 23–39.

COUTINHO, J. A. P., MIRANTE, F., PAULY, J., 2006, "A new predictive UNIQUAC for modeling of wax formation in hydrocarbon fluids", *Fluid Phase Equilibria*, v. 247, n. 1-2, pp. 8–17. doi: 10.1016/j.fluid.2006.06.002.

COUTINHO, J. A., 1998, "Predictive UNIQUAC: A new model for the description of multiphase solid-liquid equilibria in complex hydrocarbon mixtures", *Industrial and Engineering Chemistry Research*, v. 37, n. 12, pp. 4870–4875. ISSN: 08885885. doi: 10.1021/ie980340h.

CRAGOE, C. S., 1929, *Thermodynamic Properties of Petroleum Products*. Washington, DC, U.S. Dept. Commerce.

DAUBERT, T. E., DANNER, R. P., 1997, *API Technical Data Book- Petroleum Refining*. American Petroleum Institute.

DAUPHIN, C., DARIDON, J. L., COUTINHO, J., BAYLÈRE, P., POTIN-GAUTIER, M., 1999, "Wax Content Measurements in Partially Frozen Paraffinic Systems", pp. 135–151.

EDMISTER, W. C., 1958, "Applied Hydrocarbon Thermodynamics, Part 4: Compressibility Factors and Equations of State", *Pet. Ref.*, v. 37, n. 173 (Apr).

EILERTS, C. K., 1947, "Gas-condensate reservoir engineering. 1. The reservoir fluid, its composition and phase behavior", *Oil and Gas J.*

ESSS, 2019, *ALFA SIM: Artificial Lift and Flow Assurance Simulator*. ESSS, Florianópolis, Santa Catarina.

FIROOZABADI, A., 1999, *Thermodynamics of Hydrocarbon Reservoirs*. McGraw-Hill.

FORTUNA, L., GRAZIANI, S., RIZZO, A., XIBILIA, M. G., 2007, *Soft Sensors for Monitoring and Control of Industrial Processes*. Springer. ISBN: 9781846284793.

FRASHAD, F., LEBLANC, J., GARBER, J., OSORIO, J., 1996, "Empirical PVT Correlations For Colombian Crude Oils". In: *SPE Latin America/Caribbean Petroleum Engineering Conference*, pp. 311–320, Port of Spain, Trinidad & Tobago, April. Society of Petroleum Engineers. doi: 10.2118/36105-MS.

GARCÍA, A., ALMEIDA, I., SINGH, G., PURWAR, S., MONTEIRO, M., CARBONE, L., HERDEIRO, M., 2010, "An Implementation of On-line Well Virtual Metering of Oil Production". In: *SPE Intelligent Energy Conference and Exhibition*, Utrecht, Netherlands, March. Society of Petroleum Engineers.

GHORAYEB, K., HOLMES, J. A., 2005, "Black Oil Delumping". In: *SPE Annual Technical Conference and Exhibition*, pp. 2971–2983, Dallas, Texas, Oct. Society of Petroleum Engineers. doi: 10.2118/96571-MS.

GOES, M. R. R., TEIXEIRA, R. G., TAVARES, F. W., SECCHI, A. R., 2019, "Wax appearance and prevention in two-phase flow using the multi-solid and drift-flux model", *Journal of Petroleum Science and Engineering*, v. 177 (jun), pp. 374–383. doi: 10.1016/j.petrol.2019.02.057.

GÓES, M. R. R., GUEDES, T. A., D'AVILA, T. C., VIEIRA, B. F., RIBEIRO, L. D., DE CAMPOS, M. C., SECCHI, A. R., 2021, "Virtual flow metering of oil wells for a pre-salt field", *Journal of Petroleum Science and Engineering*, v. 203. doi: 10.1016/j.petrol.2021.108586.

GÓES, M. R. R., GUEDES, T. A., D'AVILA, T., RIBEIRO, L. D., DE CAMPOS, M. C. M., SECCHI, A. R., TAVARES, F. W., 2022, "Improvement of black oil delumping method applied to an offshore oil field", *Journal of Petroleum Science and Engineering*, v. 214. doi: 10.1016/j.petrol.2022.110514.

GRAHAM, E., 2015, "The future of flow", *Offshore Engineer*, v. 40, pp. 44–45.

GÓES, M. R. R., GUEDES, T. A., TEIXEIRA, R. G., MELO, P. A., TAVARES, F. W., SECCHI, A. R., 2023, "Multiphase flow simulation in offshore pipelines: An accurate and fast algorithm applied to real-field data", *Chemical Engineering Science*, v. 268. ISSN: 00092509. doi: 10.1016/j.ces.2022.118438.

HALL, K. R., YARBOROUGH, L., 1971, "New, Simple Correlation for Predicting Critical Volume", *Chem Eng.*, , n. 76 (Nov).

HANKINSON, R. W., THOMSON, G. H., 1979, "A New Correlation for Saturated Densities of Liquids and Their Mixtures", *AIChE Journal*, v. 25, n. 4, pp. 653–663.

HIBIKI, T., ISHII, M., 2003, "One-dimensional drift-flux model and constitutive equations for relative motion between phases in various two-phase flow regimes", *International Journal of Heat and Mass Transfer*, v. 46, n. 25, pp. 4935–4948. ISSN: 00179310. doi: 10.1016/S0017-9310(03)00322-3.

HODA, M. F., HOFFMANN, A., KUNTADI, A., 2017, "Advances in Molar Wellstream Computation from Well Test Measurements". In: *SPE Reservoir Characterisation and Simulation Conference and Exhibition*, pp. 937–954, Abu Dhabi, UAE, May. Society of Petroleum Engineers. doi: 10.2118/185988-MS.

HODA, M. F., WHITSON, C. H., 2013, "Well Test Rate Conversion to Compositional Wellstream". In: *SPE Middle East Oil and Gas Show and Exhibition*, v. 2, Manama, Bahrain, Mar. Society of Petroleum Engineers. doi: 10.2118/164334-MS.

HOFFMANN, A., TAEGER, J. P., WHITSON, C. H., 2017, "Application of Well Test Rate Conversion to Gas Condensate Reservoirs in the Nile Delta Complex". In: *SPE Europec featured at 79th EAGE Conference and Exhibition*, Paris, FRance, Jun. Society of Petroleum Engineers. doi: 10.2118/185849-MS.

HUANG, Z., ZHENG, S., FOGLER, H. S., 2015, *Wax Deposition: Experimental Characterizations, Theoretical Modeling, and Field Practices*. CRC Press. ISBN: 9781466567672. doi: 10.1201/b18482.

INCROPERA, F. P., DEWITT, D. P., BERGMAN, T. L., LAVINE, A. S., 2002, *Fundamentos de Transferência de Calor e Massa*, v. 6. LTC. ISBN: 9780471457282.

INFOCHEM, 2017, *User Guide for Multiflash for Windows*.

ISHII, M., HIBIKI, T., 2011, *Thermo-Fluid Dynamics of Two-Phase Flow*. Nova Iorque, Springer Science+Business Media. ISBN: 9781441979841.

ISL, 2001, *RELAP5/MOD3.3 Code Manual Volume I: Code Structure, System Models, and Solution Methods*. Information Systems Laboratories, Idaho Falls.

JHAVERI, B. S., YOUNGREN, G. K., 1988, "Three-Parameter Modification of the Peng-Robinson Equation of State to Improve Volumetric Predictions", *SPE Reservoir Engineering*, v. 3, n. 03 (Aug), pp. 1033–1040. doi: 10.2118/13118-PA.

KESLER, M. G., LEE, B. I., 1976, "Improve Prediction of Enthalpy Fractions", v. 55 (03), pp. 153–158.

LASATER, J., 1958, "Bubble Point Pressure Correlation", *Journal of Petroleum Technology*, v. 10, n. 05 (May), pp. 65–67. doi: 10.2118/957-G.

LEE, A. L., GONZALEZ, M. H., EAKIN, B. E., 1966, "The Viscosity of Natural Gases", *Journal of Petroleum Technology*, pp. 997–1000.

LESKENS, M., KRUIF, B., BELFROID, S., SMEULERS, J., GRYZLOV, A., 2008, "Downhole Multiphase Metering in Wells by Means of Soft-Sensing". In: *SPE Intelligent Energy Conference and Exhibition*, Amsterdam, Netherlands, February. Society of Petroleum Engineers.

LIRA-GALEANA, C., FIROOZABADI, A., PRAUSNITZ, J. M., 1996, "Thermodynamics of Wax Precipitation in Petroleum Mixtures", *AIChE Journal*, v. 42, n. 1.

LOHRENZ, J., BRAY, B. G., CLARK, C. R., 1964, "Calculating Viscosities of Reservoir Fluids From Their Compositions". In: *SPE Anuual Fall Meeting*, pp. 1171–1176, Houston, Texas.

MANDHANE, J. M., GREGORY, G. A., AZIZ, K., 1974, "A Flow Pattern Map for Gas-Liquid Flow in Horizontal Pipes", *International Journal of Multiphase Flow*, v. 1, pp. 537–553.

MARTIN, J. J., 1979, "Cubic Equations of State-Which?" *Industrial Engineering Chemistry Fundamentals*, v. 18, n. 2 (may), pp. 81–97. ISSN: 0196-4313. doi: 10.1021/i160070a001.

MCCAIN, W., 1990, *The Properties of Petroleum Fluids*. PennWell Books. ISBN: 9780878143351.

MEEHAN, D. N., 1980, "A Correlation for Water Compressibility", *Pet. Eng. Intl.*, v. 125 (November).

MUKHERJEE, H., 1979, *An experimental study of inclined two-phase flow*. Tese de Doutorado, University of Tulsa.

MULTIFLASH, 2014, *User Guide for Multiflash for Windows*.

NEMOTO, R. H., BALIÑO, J. L., TANAKA, R. L., GODINHO, C. A., 2010, "A Case of Study in Flow Assurance of a Pipeline-Rise System Using Olga". In: *13th Brazilian Congress of Thermal Sciences and Engineering*, Uberlandia, Minas Gerais, Brasil.

NICHITA, D. V., GOUAL, L., COLLEGE, I., FIROOZABADI, A., 2001, "Wax Precipitation in Gas Condensate Mixtures", *SPE Production & Facilities*, , n. November.

PASO, K., BRAATHEN, B., VIITALA, T., ASKE, N., RØNNINGSEN, H. P., SJÖBLOM, J., 2009, "Wax Deposition Investigations with Thermal Gradient Quartz Crystal Microbalance". In: *Handbook of Surface and Colloid Chemistry*, cap. 13.

PEDERSEN, K. S., SKOVBORG, P., RONNINGSEN, H. P., 1991, "Wax Precipitation for North Sea Crude Oils. 4. Thermodynamic Modeling", *Energy & Fuels*, , n. 5, pp. 924–932.

PRAUSNITZ, J. M., LICHTENTHALER, R. N., DE AZEVEDO, E. G., 1986, *Molecular Thermodynamics of Fluid Phase Equilibria*. Prentice Hall PTR.

QUAYLE, O. R., 1953, *The Parachor of Organic Compounds*. Relatório técnico, Emory University, Georgia.

QUTAMI, T. A., IBRAHIM, R., ISMAIL, I., ISHAK, M. A., 2017, "Development of Soft Sensor to Estimate Multiphase Flow Rates Using Neural Networks and Early Stopping", *International Journal on Smart Sensing and Intelligent Systems*, v. 10, pp. 199–222.

RACHFORD, H., RICE, J., 1952, "Procedure for Use of Electronic Digital Computers in Calculating Flash Vaporization Hydrocarbon Equilibrium", *Journal of Petroleum Technology*, v. 195. doi: 10.2118/952327-g.

REID, R. C., PRAUSNITZ, J. M., POLING, B. E., 1987, *The properties of gases and liquids*. McGraw-Hill. ISBN: 0070517991,9780070517998.

RIAZI, M. R., 2005, *Characterization and Properties of Petroleum Fractions*. 1 ed. Philadelphia, International Standards Worldwide. ISBN: 0803133618.

ROBINSON, D. B., PENG, D.-Y., CHUNG, S. Y.-K., 1985, "The Development of The Peng - Robinson Equation and Its Application to Phase Equilibrium in a System Containing Methanol", *Fluid Phase Equilibria*, v. 24, pp. 25–41.

RONNINGSEN, H. P., SOMME, B. F., PEDERSEN, K. S., 1997, "An Improved Thermodynamic Model for Wax Precipitation: Experimental Foundation and Application". In: *8th International Conference on Multiphase'97*, pp. 18–20, Cannes, France.

SANZO, S., MONTINI, M., CADEI, L., GIULIANI, M., BIANCO, A., 2020, "Virtual Metering and Allocation using Machine Learning Algorithms". In: *International Petroleum Technology Conference*, Dhahran, Saudi Arabia, January. International Petroleum Technology Conference.

SCHLUMBERGER, 2017, *OLGA User Manual*.

SECCHI, A. R., 2012. "Differential Algebraic System Solver in C". http://www.enq.ufrgs.br/enqlib/numeric.

SILVA, V. M., CARMO, R. P., FLEMING, F. P., DARIDON, J. L., PAULY, J., TAVARES, F. W., 2017, "Paraffin solubility and calorimetric data calculation using Peng-Robinson EoS and modified UNIQUAC models", *Journal of Petroleum Science and Engineering*, v. 156, n. June, pp. 945–957. doi: 10.1016/j.petrol.2017.06.064.

SINGH, P., VENKATESAN, R., FOGLER, H. S., NAGARAJAN, N., 2000, "Formation and aging of incipient thin film wax-oil gels", *AIChE Journal*, v. 46, n. 5, pp. 1059–1074. doi: 10.1002/aic.690460517.

SMITH, J. M., VAN NESS, H. C., ABBOTT, M. M., 2007, *Introdução à Termodinâmica da Engenharia Química*. 7 ed. Rio de Janeiro, LTC.

SOAVE, G., 1972, "Equilibrium Constants from a Modified Redlich-Kwong Equation of State", *Chemical Engineering Science*, v. 27, n. 6, pp. 1197–1203.

SOREIDE, I., 1989, *Improved Phase Behavior Predictions of Petroleum Reservoir Fluids From a Cubic Equation of State*. Tese de Doutorado, Norwegian Inst. of Technology.

SPENCER, C. F., DANNER, R. P., 1972, "Improved Equation for Prediction of Saturated Liquid Density", *Journal of Chemical Engineering Data*, v. 17, n. 2.

STANDING, M. B., 1974, *Petroleum Engineering Data Book*. Trondheim, Norway, Norwegian Institute of Technology.

STANDING, M. B., 1981, *Volumetric and Phase Behavior of Oil Field Hydrocarbon Systems*. 9 ed. Dallas, Texas.

STEVENS, W. F., THODOS, G., 1963, "Estimation of enthalpies: Multicomponent hydrocarbon mixtures at their saturated vapor and liquid states", *AIChE Journal*, v. 9, n. 3 (may), pp. 293–296. ISSN: 0001-1541. doi: 10.1002/aic.690090304.

SVENDSEN, J. A., 1993, "Mathematical Modeling of Wax Deposition in Oil Pipeline Systems", *AIChE Journal*, v. 39, n. 8, pp. 1377–1388.

TEIXEIRA, R. G., SECCHI, A. R., 2017, "Assessment of the Accuracy and Dynamic Simulation Capabilities of Liquid-Vapour Two-Phase Flow Separated and Mixture Models", *Computer Aided Chemical Engineering*, v. 40, pp. 2095–2100. doi: 10.1016/B978-0-444-63965-3.50351-2.

THOMAS, J. E., 2001, *Fundamentos da Engenharia de Petróleo*. Rio de Janeiro, Editora Interciência.

THOMSON, G. H., BROBST, K. R., HANKINSON, W., 1982, "An Improved Correlation for Densities of Compressed Liquids and Liquid Mixtures", *AIChE Journal*, v. 28, n. 4, pp. 671–676.

URSINI, F., ROSSI, R., CASTELNUOVO, L., PERRONE, A., BENDARI, A., POLLERO, M., 2019, "The Benefits of Virtual Meter Applications on Production Monitoring andReservoir Management". In: *SPE Reservoir Characterisation and Simulation Conference and Exhibition*, Abu Dhabi, UAE, September. Society of Petroleum Engineers.

VALENTE, A. C., NUNES, R., LUCAS, E., 2022, "Influence of Refinery Asphalt Residue Addition on Flow: A Study Using Waxy Model-System", *Journal of the Brazilian Chemical Society*, pp. 1–9. ISSN: 01035053. doi: 10.21577/0103-5053.20220090.

VENKATESAN, R., 2004, *The Deposition and Rheology of Organic Gels*. Tese de Doutorado, University of Michigan.

WHITSON, C. H., BRULÉ, M. R., 2000, *Phase Behavior*, v. 20. Society of Petroleum Engineering. ISBN: 1555630871.

WHITSON, C. H., SUNJERGA, S., 2012, "PVT in Liquid-Rich Shale Reservoirs". In: *SPE Annual Technical Conference and Exhibition*, v. 1, pp. 151–175, Texas, USA, Apr. Society of Petroleum Engineers. doi: 10.2118/155499-MS.

WON, K. W., 1986, "Thermodynamics for Solid Solution Liquid-Vapor Equilibria: Wax Phase Formation from Heavy Hydrocarbon Mixtures", *Fluid Phase Equilibria*, v. 30, pp. 265–279.

Appendix A

Complementary Material

The mass flow of a phase k is equal to the product of the void fraction, density and velocity of this phase as shown by Eq. A.1.

$$G^k = \alpha^k \rho^k v^k \tag{A.1}$$

TEIXEIRA and SECCHI (2017) deduced an equation that relates v^V, v^m and $\hat{v}_v^{des}$ as shown by Eq. A.2.

$$v^m = v^V - \frac{\rho^L}{\rho^m} \hat{v}_v^{des} \tag{A.2}$$

Then, substituting the Eqs. A.1 and A.2 in continuity equation of the vapor phase, Eq. 5.4, this may be rewritten as shown in Eq. A.3.

$$\frac{dG^V}{dx} = \Gamma^V \tag{A.3}$$

Besides, the definition of the vaporized mass fraction is shown in Eq. A.4.

$$\beta_W = \frac{W^V}{W^L + W^V} = \frac{W^V/A}{(W^L + W^V)/A} = \frac{G^V}{\rho^m v^m} \tag{A.4}$$

where W^V and W^L are the vapor and liquid mass flow rate, respectively.

Therefore, the mass flow of the vapor phase can be described by Eq. A.5.

$$G^V = \beta_W \rho^m v^m \tag{A.5}$$

Substituting Eq. A.5 in Eq. A.3 a new expression for the Γ^V is obtained, Eq. A.6.

$$\Gamma^V = \frac{d(\beta_W \rho^m v^m)}{dx} \tag{A.6}$$

Then, applying the chain rule on Eq. A.6 and taking into account the continuity equation of the mixture, Eq. 5.25 is obtained.

Table A.1: Global composition of the mixtures available in DAUPHIN *et al.* (1999).

	BIM 0	**BIM 3**	**BIM 5**	**BIM 9**	**BIM 13**
n-Decane	0.8010924	0.7999289	0.8000209	0.8004388	0.7983136
n-Octadecane	0.0300333	0.0342603	0.0370963	0.0475053	0.0713504
n-Nonadecane	0.0255350	0.0291523	0.0319587	0.0406423	0.0614821
n-Eicosane	0.0219252	0.0247271	0.0273437	0.0349090	0.0527752
n-Heneicosane	0.0187411	0.0212042	0.0241744	0.0298584	
n-Docontane	0.0160168	0.0183246	0.0200727	0.0257054	
n-Tricosane	0.0137753	0.0157321	0.0172040		
n-Tetracosane	0.0118721	0.0138931	0.0146822		
n-Pentacosane	0.0101204	0.0117383			
n-Hexacosane	0.0097576				
n-Heptacosane	0.0074726				
n-Octacosane	0.0065157				
n-Nonacosane	0.0055111	0.0062228			
n-Triacontane	0.0047250	0.0053502	0.0060048		
n-Heneitriacontane	0.0040465	0.0046431	0.0050301		
n-Dotriacontane	0.0034696	0.0039290	0.0043542	0.0055577	
n-Tritriacontane	0.0030772	0.0033799	0.0037949	0.0047741	
n-Tetratriacontane	0.0025848	0.0029110	0.0031801	0.0040872	0.0061543
n-Pentatriacontane	0.0018635	0.0024472	0.0027145	0.0035097	0.0052782
n-Hexatriacontane	0.0018648	0.0021559	0.0023685	0.0030121	0.0046463

Table A.2: Global composition of the mixture (Oil 10) available in RONNINGSEN *et al.* (1997).

	Oil 10A	**Oil 10B**	**Oil 10C**	**Oil 10D**	**Oil 10E**
Nitrogen	0.0048	0.0025	0.0008	0.0001	
Carbon dioxide	0.0404	0.0365	0.0287	0.0128	0.0003
Methane	0.5741	0.4176	0.2388	0.0521	0.0005
Ethane	0.0928	0.0934	0.0875	0.0589	0.0024
Propane	0.0562	0.0665	0.0768	0.0775	0.0082
i-Butane	0.01	0.0129	0.0163	0.0191	0.0038
n-Butane	0.0222	0.0297	0.0389	0.0478	0.0122
i-Pentane	0.0083	0.0119	0.0164	0.0217	0.0098
n-Pentane	0.0105	0.0153	0.0215	0.0289	0.0150
n-Hexane	0.0135	0.0208	0.0302	0.0422	0.0362
n-Heptane	0.0221	0.0362	0.0538	0.0764	0.0852
n-Octane	0.0259	0.0435	0.0654	0.0936	0.1211
n-Nonane	0.0149	0.0255	0.0386	0.0555	0.0788
Pseudocomponent	0.1043	0.1878	0.2863	0.4134	0.6264

Table A.3: Physical properties of the pseudocomponent from "Oil 10" available in RONNINGSEN *et al.* (1997).

Molar mass (g/mol)	**Density** (g/cm^3)
252	0.860

Table A.4: Global composition of the mixture ("Oil 11") available in RONNINGSEN *et al.* (1997).

	Oil 11A	**Oil 11B**	**Oil 11C**	**Oil 11D**	**Oil 11E**
Nitrogen	0.0029	0.0013	0.0004	0.0001	0.0002
Carbon dioxide	0.0557	0.0492	0.0389	0.0276	0.0177
Methane	0.5562	0.3823	0.2197	0.1099	0.0481
Ethane	0.0906	0.0900	0.0838	0.0717	0.0565
Propane	0.0508	0.0603	0.0682	0.0706	0.0681
i-Butane	0.0091	0.0118	0.0145	0.0161	0.0167
n-Butane	0.0187	0.0253	0.0321	0.0365	0.0387
i-Pentane	0.0070	0.0102	0.0135	0.0159	0.0174
n-Pentane	0.0080	0.0118	0.0158	0.0188	0.0207
Hexane	0.0107	0.0168	0.0233	0.0283	0.0316
Heptane	0.0195	0.0326	0.0460	0.0564	0.0635
Octane	0.0227	0.0389	0.0555	0.0682	0.0771
Nonane	0.0139	0.0242	0.0347	0.0428	0.0484
Pseudocomponent	0.1342	0.2453	0.3538	0.4372	0.4956

Table A.5: Physical properties of the pseudocomponent from "Oil 11" available in RONNINGSEN *et al.* (1997).

Molar mass (g/mol)	**Density** (g/cm^3)
290	0.876

Table A.6: Global composition of the mixture available in WHITSON and BRULÉ (2000).

Nitrogen	0.21
Carbon dioxide	0.93
Methane	0.5877
Ethane	0.0757
Propane	0.0409
i-Butane	0.0091
n-Butane	0.0209
i-Pentane	0.0077
n-Pentane	0.0115
Hexane	0.0175
Pseudocomponent	0.2176

Table A.7: Physical properties of the pseudocomponent from volate oil available in WHITSON and BRULÉ (2000).

Molar mass (g/mol)	**Density** (g/cm^3)
228	0.858

Appendix B

Thermodynamic Modeling

In this work, the cubic equation of state Peng-Robinson (EOS PR) was used to calculate the vapor-liquid equilibrium (VLE). In this step, the molar fractions of each component i in the liquid and vapor phases, equilibrium constant, vaporized molar fraction of the mixture, and enthalpy of liquid and vapor phases are calculated.

B.1 Vapor-liquid Equilibrium (VLE)

As a model simplification, it was considered that the system is at equilibrium at each discretized point of the pipeline. This results in an iterative procedure of flash algorithm at each discretized point at a given temperature, pressure, and fluid composition. This iterative method uses the Rachford-Rice equation for its resolution (RACHFORD and RICE, 1952; RIAZI, 2005).

Before starting the iterative procedure, the initial estimate of the equilibrium constant of the component i ($K_i^{initial}$) is calculated using the Wilson equation (WHITSON and BRULÉ, 2000), given by Eq. B.1.

$$K_i^{initial} = \frac{P_{ci}}{P} \exp\left[5.37\,(1+\omega_i)\left(1-\frac{T_{ci}}{T}\right)\right] \tag{B.1}$$

where P_{ci} is the critical pressure, T_{ci} is the critical temperature, and ω_i is the acentric factor of component i.

Then, the iterative procedure for calculating the equilibrium constant starts. Within this procedure, there is another iterative algorithm for calculating the vaporized molar fraction (β) using the Rachford-Rice equation, given by Eq. B.2

(RACHFORD and RICE, 1952). The initial estimate for the value of β used in this work is equal to 0.5.

$$f(\beta) = \sum_{i=1}^{n} \frac{z_i \left(K_i^{initial} - 1\right)}{1 + \beta \left(K_i^{initial} - 1\right)} \tag{B.2}$$

where z_i is the global molar composition of the component i and n is the number of components of the mixture.

Deriving Eq. B.2 with respect to β, we obtain Eq. B.3.

$$\frac{df\left(\beta\right)}{d\beta} = -\sum_{i=1}^{n} \frac{z_i \left(K_i^{initial} - 1\right)^2}{\left[1 + \beta \left(K_i^{initial} - 1\right)\right]^2} \tag{B.3}$$

A new estimate for the value of β is calculated using Newton's Method, as shown in Eq. B.4.

$$\beta_{new} = \beta - \frac{f(\beta)}{\frac{df(\beta)}{d\beta}} \tag{B.4}$$

The iterative procedure for calculating β is repeated until the absolute difference between the values of β and β_{new} is less than a given tolerance, as described in Eq. B.5. If the difference between these values does not satisfy the tolerance, the value of β_{new} is assigned to β and the iterative procedure for calculating β starts again. The tolerance value used in this work is equal to 10^{-6}.

$$\mid \beta_{new} - \beta \mid < \varepsilon_\beta \tag{B.5}$$

Given the convergence of β calculation, the algorithm returns to the iterative procedure to calculate the equilibrium constant of each component. Therefore, the molar fractions of each component in the liquid and vapor phases, x_i and y_i, are calculated using the values of β and $K_i^{initial}$, as shown in Eqs. B.6 and B.7.

$$x_i = \frac{z_i}{1 + \beta(K_i^{initial} - 1)} \tag{B.6}$$

$$y_i = K_i^{initial} x_i \tag{B.7}$$

where x_i and y_i are the molar fractions of the component i in the liquid and vapor phases, respectively.

Then, the EOS PR parameters of each pure component i of the mixture are calculated using the equations described in Table B.1.

Table B.1: EOS PR parameters.

u_1	2
u_2	-1
a_i	$0.457236R^2T_{ci}^2\alpha_i/P_{ci}$
α_i	$[1+(0.37464+1.54226\omega_i-0.26992\omega_i^2)(1-\sqrt{T_{ri}})]^2$
b_i	$0.077796RT_{ci}/P_{ci}$

where T_{ri} is the reduced temperature of component i, given by Eq. B.8, and R is the real gases constant. In this work, R equals to 8.314 $m^3Pa/mol/K$.

$$T_{ri} = \frac{T_{ci}}{T} \tag{B.8}$$

After calculating the EOS PR parameters of each component, the EOS PR parameters of the liquid and vapor phases are calculated using the quadratic mixing rule, as shown in Eqs. B.9 - B.10. This mixing rule is used for mixtures of petroleum and hydrocarbons (RIAZI, 2005).

$$a_f^{mist} = \sum_{i=1}^{n}\sum_{j=1}^{n} phase_i phase_j a_i a_j (1-k_{ij}) \tag{B.9}$$

$$b_f^{mist} = \sum_{i=1}^{n} phase_i b_i \tag{B.10}$$

where a_j and b_j are the EOS PR parameters of the component j; $phase_i$ and $phase_j$ are the molar fractions of the components i and j, respectively, in phase f; and k_{ij} is the binary interaction parameter between the components of the mixture.

The values of k_{ij}, given in Tables B.2 and B.3, used in this work were obtained from the software Multiflash (MULTIFLASH, 2014).

Table B.2: Binary interaction parameter (k_{ij}).

	CO_2	**N_2**	**Methane**	**Ethane**	**Propane**	**i-Butane**
CO_2	0	-0.017	0.092	0.11337	0.11203	0.11056
N_2	-0.017	0	0.031	0.0577999	0.07248	0.0885824
Methane	0.092	0.031	0	0.0154511	0.0203843	0.0247469
Ethane	0.11337	0.0577999	0.0154511	0	0	0.024297
Propane	0.11203	0.07248	0.0203843	0	0	0
i-Butane	0.11056	0.0885824	0.0247469	0.0247469	0	0
n-Butane	0.11075	0.0864354	0.0247469	0.024297	0	0
i-Pentane	0.1095	0.10012	0.0286086	0.0281586	0.0271865	0
n-Pentane	0.10955	0.0995857	0.0286086	0.0281586	0.0271865	0
n-Hexane	0.107948	0.117182	0.03203	0.0315799	0.0306075	0.0278318
C_{7+}	0.0947779	0.19	0.0512819	0.0508318	0.0498594	0.0470837

Table B.3: Binary interaction parameter (k_{ij}).

	n-Butane	**i-Pentane**	**n-Pentane**	**n-Hexane**	**C_{7+}**
CO_2	0.11075	0.1095	0.10955	0.107948	0.0947779
N_2	0.0864354	0.10012	0.0995857	0.117182	0.19
Methane	0.0247469	0.0286086	0.0286086	0.03203	0.0512819
Ethane	0.024297	0.0281586	0.0281586	0.0315799	0.0508318
Propane	0	0.0271865	0.0271865	0.0306075	0.0498594
i-Butane	0	0	0	0.0278318	0.0470837
n-Butane	0	0	0	0.0278318	0.0470837
i-Pentane	0	0	0	0	0.0320895
n-Pentane	0	0	0	0	0.0320895
n-Hexane	0.0278318	0	0	0	0
C_{7+}	0.0470837	0.0320895	0.0320895	0	0

According to REID *et al.* (1987), the cubic equations of state may be written as shown by Eq. B.11.

$$P = \frac{RT}{V-b} - \frac{a}{V^2 + u_1 bV + u_2 b^2} \tag{B.11}$$

where V is the mixture molar volume of a certain phase.

Eq. B.11 can be rewritten to make it cubic with respect to the variable Z (compressibility factor), as shown in Eq. B.12 (REID *et al.*, 1987).

$$Z_f^3 - (1 + B_f - u_1 B_f) Z_f^2 + (A_f + u_2 B_f^2 - u_1 B_f - u_1 B_f^2) Z_f - A_f B_f - u_2 B_f^2 - u_2 B_f^3 = 0 \tag{B.12}$$

where

$$A_f = \frac{a_f^{mist} P}{R^2 T^2} \tag{B.13}$$

$$B_f = \frac{b_f^{mist} P}{RT} \tag{B.14}$$

where A_f and B_f are the EOS PR parameters of phase f.

The above equations are used in both phases (liquid and vapor) at a given temperature, pressure, and molar composition of the mixture. The subscript f refers to the liquid or vapor phases.

From the result of the cubic equation of state, Eq. B.12, three real and different roots are obtained, so the roots with the lowest and highest values correspond to the compressibility factor of the liquid and vapor phases, respectively.

After calculating the compressibility factor of the phases, the fugacity coefficient of the component i in the phase f, ϕ_{fi}, is calculated, as shown in Eq. B.15 (REID *et al.*, 1987).

$$\ln \phi_{fi} = \frac{T_{ci}/P_{ci}}{\sum_{i=1}^{n} y_i T_{cj}/P_{cj}} (Z_f - 1) - \ln (Z_f - B_f) + \frac{A_f}{B_f \sqrt{u_1^2 - u_2^2}} \left(\frac{b_i}{b_f^{mist}} - \frac{2\sqrt{a_i}}{A_f} \sum_{i=1}^{n} x_j \sqrt{a_j} (1 - k_{ij}) \right) \times \ln \frac{2Z_f + B_f \left(u_1 + \sqrt{u_1^2 - 4u_2} \right)}{2Z_f + B_f \left(u_1 - \sqrt{u_1^2 - 4u_2} \right)} \tag{B.15}$$

where T_{cj} and P_{cj} are the critical temperature and pressure, respectively, of component j.

Given the values of the fugacity coefficients of all components in both phases, a new estimate for the equilibrium constant is calculated, as shown by Eq. B.16.

$$K_i^{new} = \frac{\phi_{li}}{\phi_{vi}} \tag{B.16}$$

where ϕ_{li} and ϕ_{vi} are fugacity coefficients of the component i in the liquid and vapor phases, respectively.

This iterative procedure for calculating the equilibrium constant is repeated until the tolerance described in Eq. B.17 is satisfied. If the tolerance is not satisfied, the iterative procedure starts again, and the value of $K_i^{inicial}$ is assigned the value of K_i^{new}. In this work, ε_K equals 0.0001.

$$\sum_{i=1}^{n} \frac{K_i^{new}}{K_i^{initial}} < \varepsilon_K \tag{B.17}$$

As a result of the convergence of the iterative procedure, the molar fractions of each component i in the liquid and vapor phases are used to calculate the physical properties of the phases, for example. The vaporized molar fraction of the mixture is converted into vaporized mass fraction, an important variable of the DFM. The compressibility factor of both phases is used to calculate the density of the liquid and vapor phases and the enthalpy of the two phases.

B.2 Enthalpy

The enthalpy of the liquid and vapor phases is given by Eq. B.18 (SMITH *et al.*, 2007).

$$h_f = h_f^R + h_f^{gi} \tag{B.18}$$

where h_f^R is the residual enthalpy of phase f and h_f^{gi} is the enthalpy in the ideal gas state of phase f at the same temperature and pressure.

B.2.1 Enthalpy in the Ideal Gas State

According to SMITH *et al.* (2007), in the ideal gas state, the enthalpy of the liquid and vapor phases (in J/mol) is given by Eq. B.19.

$$h_f^{gi} = \left[\sum_{i=1, i \neq C_{7+}}^{n} \int_{T_0}^{T} C_{pfi} dT \right] + h_{fC_{7+}}^{gi} \tag{B.19}$$

where T_0 is the reference temperature, which equals to $273K$; and C_{pfi} and $h_{fC_{7+}}^{gi}$ are the heat capacity of component i and enthalpy of pseudocomponent, respectively,

in phase f, in J/mol, in the ideal gas state.

To calculate the heat capacity integral (in $J/mol/K$), the correlation proposed by DAUBERT and DANNER (1997) was used, as shown in Eq. B.20. T and T_0 must be in $^\circ R$ and MM_i in g/mol to use this correlation.

$$\int_{T_0}^{T} C_{pfi}dT = [A_i + B_i(T - T_0) + C_i(T^2 - {T_0}^2) + D_i(T^3 - {T_0}^3) + E_i(T^4 - {T_0}^4) + F_i(T^5 - {T_0}^5)] \times \frac{2326 fase_i}{MM_i} \tag{B.20}$$

where A_i, B_i, C_i, D_i, E_i, and F_i are the parameters related to each component of the mixture, given in Table B.4.

Table B.4: Parameters to calculate the enthalpy in the ideal gas state.

	A	B	$C \times 10^3$	$D \times 10^6$	$E \times 10^{10}$	$F \times 10^{14}$
CO_2	0.096880	0.158843	-0.033712	0.148105	-0.966203	2.073832
N_2	-0.656650	0.254098	-0.016624	0.015302	-0.030995	0.015167
Methane	-2.838570	0.538285	-0.211409	0.339276	-1.164322	1.389612
Ethane	-0.014220	0.264612	-0.024568	0.291402	-1.281033	1.813482
Propane	0.687150	0.160304	0.126084	0.181430	-0.918913	1.354850
i-Butane	1.459560	0.099070	0.238736	0.091593	-0.594050	0.909645
n-Butane	7.228140	0.099687	0.266548	0.054073	-0.429269	0.669580
i-Pentane	17.694120	0.015946	0.382449	-0.027557	-0.143035	0.295677
n-Pentane	9.042090	0.111829	0.228515	0.086331	-0.544649	0.818450
n-Hexane	12.991820	0.089705	0.265348	0.057782	-0.452211	0.702597

To calculate the enthalpy of the pseudocomponent in the ideal gas state in the liquid and vapor phases (in J/mol), the correlation proposed by STEVENS and THODOS (1963), described in Eq. B.21, was used. T and $MM_{C_{7+}}$ must be in $^\circ F$ and g/mol, respectively, to use this correlation.

$$h^{gi}_{fC_{7+}} = \left\{ \left(100MM_{C_{7+}} + 800\right) + \left[\left(32.15MM_{C_{7+}} + 186.5\right)\frac{T}{100}\right] + \left[\left(3.708MM_{C_{7+}} - 26.42\right)\left(\frac{T}{100}\right)^2\right] + \left[\left(-0.0859MM_{C_{7+}} + 0.40\right)\left(\frac{T}{100}\right)^3\right]\right\} \times 2.3260 \times phase_{C_{7+}} \tag{B.21}$$

where $MM_{C_{7+}}$ is the molar mass of the pseudocomponent and $phase_{C_{7+}}$ is the molar composition of the pseudocomponent in liquid or vapor phase.

B.2.2 Residual Enthalpy

The residual enthalpy of the liquid and vapor phases is calculated using Eq. B.22, where the residual enthalpy is the difference between the enthalpy in the real and ideal gas state.

$$h^R_f = A^R_f + Ts^R_f + RT(Z_f - 1) \tag{B.22}$$

where A^R_f and s^R_f are the Helmholtz residual energy and residual entropy of phase f.

According to REID *et al.* (1987), the residual properties may be defined using the data calculated in the VLE, as explained in Section B.1. Therefore, the correlations that calculate the residual properties are derived from any cubic equation of state explicit in P. The correlations used in this work are described in the Eqs. B.23 - B.25.

$$s^R_f = R\ln\frac{Z_f - B_f}{Z_f} - \frac{1}{b^{mist}_f\sqrt{u_1^2 - 4u_2}}\frac{\partial a^{mist}_f}{\partial T} + \ln\frac{2Z_f + B_f\left(u_1 - \sqrt{u_1^2 - 4u_2}\right)}{2Z_f + B_f\left(u_1 + \sqrt{u_1^2 - 4u_2}\right)} \tag{B.23}$$

$$A^R_f = \frac{a^{mist}_f}{b^{mist}_f\sqrt{u_1^2 - 4u_2}}\ln\frac{2Z_f + B_f\left(u_1 - \sqrt{u_1^2 - 4u_2}\right)}{2Z_f + B_f\left(u_1 + \sqrt{u_1^2 - 4u_2}\right)} - RT\ln\frac{Z_f - B_f}{B_f} \tag{B.24}$$

where

$$\frac{\partial a_f^{mist}}{\partial T} = -\frac{R}{2}\sqrt{\frac{0.45724}{T}}\sum_{i=1}^{n}\sum_{j=1}^{n} y_i y_j \left(1-k_{ij}\right)\left[\left(0.37464+1.54226\omega_j-0.26992\omega_j^2\right)\left(\frac{a_i T_{cj}}{P_{cj}}\right)^{1/2}+\left(0.37464+1.54226\omega_i-0.26992\omega_i^2\right)\left(\frac{a_j T_{ci}}{P_{ci}}\right)^{1/2}\right] \tag{B.25}$$

where ω_j is the acentric factor of component j.

Therefore, the enthalpies of the liquid and vapor phases were calculated following the procedure described in this section.

Appendix C

Physical Properties

This section describes the correlations used to calculate the physical properties of the liquid and vapor phases of the mixture: density, viscosity and surface tension.

C.1 Liquid Phase

To calculate the physical properties of the liquid phase, the molar mass of the this phase (MM_l in kg/mol) is calculated, as shown by Eq. C.1.

$$MM_l = \sum_{i=1}^{n} x_i MM_i \tag{C.1}$$

where MM_i is the molar mass of component i.

C.1.1 Density

THOMSON *et al.* (1982) used Eq. C.2 to calculate the density of the liquid phase.

$$\rho_l = \frac{MM_l}{V_m} \tag{C.2}$$

RIAZI (2005) commented that when the system is flowing at pressures above 50 bar, the effect of pressure on the volume of liquids may not be ignored. Therefore, there is a need for a correlation that takes into account the effect of pressure on the volume of liquids. THOMSON *et al.* (1982) had recommended the use of the Tait Equation, shown in Eq. C.3, to calculate the molar volume of the mixture, V_m.

These authors also developed a correlation to calculate the parameters B, C, and $\hat{e}$, as shown in Eqs. C.4, C.6, and C.5, respectively. According to THOMSON *et al.* (1982), part of the prediction ability of Eq. C.3 is due to the correlation used to calculate the $\hat{e}$ parameter.

$$V_m = V_{sat_m}\left(1 - C\ln\frac{B+P}{B+P_{sm}}\right) \tag{C.3}$$

$$\frac{B}{P_{cm}} = -1 + \hat{a}(1-T_{rm})^{1/3} + \hat{b}(1-T_{rm})^{2/3} + \hat{d}(1-T_{rm}) + \hat{e}(1-T_{rm})^{4/3} \tag{C.4}$$

$$\hat{e} = \exp(\hat{f} + \hat{g}w_{SRK\,m} + \hat{h}w_{SRK\,m}^2) \tag{C.5}$$

$$C = \hat{j} + \hat{k}w_{SRK\,m} \tag{C.6}$$

where the values of the parameters ($\hat{a}$, $\hat{b}$, $\hat{d}$, $\hat{f}$, $\hat{g}$, $\hat{h}$, $\hat{j}$ e $\hat{k}$) are described in Table C.1; $w_{SRK\,m}$ is the acentric factor of the mixture, Eq. C.9; P_{cm} is the critical pressure of the mixture, Eq. C.7; T_{rm} is the reduced temperature of the mixture, Eq. C.10; P_{sm} is the vapor or saturation pressure given in DAUBERT and DANNER (1997), Eq.C.17.

Table C.1: Values of the parameters

$\hat{a}$	-9.070217
$\hat{b}$	62.45326
$\hat{d}$	-135.1102
$\hat{f}$	4.79594
$\hat{g}$	0.250047
$\hat{h}$	1.14188
$\hat{j}$	0.0861488
$\hat{k}$	0.0344483

The parameters, given in Table C.1, are valid for mixtures that contain one or some of the 18 different components listed in THOMSON *et al.* (1982), with reduced temperature, and acentric factor ranging from 0.36 to 0.99, and 0 to 0.8124, respectively.

The Mixing Rules to calculate the critical and physical properties of the liquid phase are described below.

$$P_{cm} = \frac{Z_{RA\,m}RT}{V_m{}^{\circ}} \tag{C.7}$$

where $Z_{RA\,m}$ is the compressibility factor of the mxiture given by Eq. C.8 and $V_m{}^\circ$ is the characteristic volume of the mixture given by Eq. C.13.

$$Z_{RA\,m} = 0.29056 - 0.08775 w_{SRK\,m} \tag{C.8}$$

$$w_{SRK\,m} = \sum_{i=1}^{N} x_i^L w_{SRK\,i} \tag{C.9}$$

$$T_{rm} = \frac{T}{T_{cm}} \tag{C.10}$$

where T_{cm} is the critical temperature of the mixture given by Eq. C.11.

$$T_{cm} = \frac{\sum_{i=1}^{N}\sum_{j=1}^{N} x_i^L x_j^L V_{ij}{}^\circ T_{cij}}{V_m{}^\circ} \tag{C.11}$$

where the term $V_{ij}{}^\circ T_{cij}$ is calculated as shown by Eq. C.12.

$$V_{ij}{}^\circ T_{cij} = \sqrt{V_i{}^\circ T_{ci} V_j{}^\circ T_{cj}} \tag{C.12}$$

where $V_i{}^\circ$ is the COSTALD characteristic volume of component i. The values are found in HANKINSON and THOMSON (1979).

Eq. C.13 was used to calculate the characteristic volume of the mixture, $V_m{}^\circ$.

$$V_m{}^\circ = \frac{1}{4}\left(\sum_{i=1}^{N} x_i^L V_i{}^\circ + 3\left(\sum_{i=1}^{N} V_i{}^{\circ 2/3}\right)\left(\sum_{i=1}^{N} x_i^L V_i{}^{\circ 1/3}\right)\right) \tag{C.13}$$

According to HANKINSON and THOMSON (1979), the acentric factor with subscript SRK due to the fact that these values were calculated using the equation developed by SOAVE (1972). HANKINSON and THOMSON (1979) calculated the acentric factor of more than 200 compounds, among them the paraffinic compounds that will be studied in this work.

For a mixture in the liquid phase, V_{sat_m} in Eq. C.3 was calculated according to the correlation developed by HANKINSON and THOMSON (1979), described in Eq. C.14.

$$V_{sat_m} = V_m{}^\circ V_R^{(0)}\left[1 - w_{SRK\,m} V_R^{(1)}\right] \tag{C.14}$$

$$\begin{aligned} V_R^{(0)} =& 1 + \hat{a}(1 - T_{rm})^{1/3} + \hat{b}(1 - T_{rm})^{2/3} + \hat{d}(1 - T_{rm}) \\ &+ \hat{e}(1 - T_{rm})^{4/3} \quad (0.25 < T_{rm} < 1) \end{aligned} \tag{C.15}$$

$$V_R^{(1)} = \frac{\hat{e} + \hat{f}T_{rm} + \hat{g}T_{rm}^2 + \hat{h}T_{rm}^3}{T_{rm} - 1.00001} \quad (0.25 < T_{rm} < 0.95) \tag{C.16}$$

The saturation pressure of the mixture, P_{sm}, is given by Eq. C.17. The reduced pressure of the mixture, P_{rm}, is calculated by using Eq. C.18. The parameters $P_{rm}^{(0)}$, $P_{rm}^{(1)}$, $\hat{\alpha}$, and $\hat{\beta}$ are calculated by using Eqs.C.19, C.20, C.21, and C.22, respectively.

$$P_{sm} = P_{cm}P_{rm} \tag{C.17}$$

$$\log(P_{rm}) = Prm^{(0)} + w_{SRK\,m}P_{rm}^{(1)} \tag{C.18}$$

$$Prm^{(0)} = 5.8031817\log(T_{rm}) + 0.07608141\hat{\alpha} \tag{C.19}$$

$$P_{rm}^{(1)} = 4.86601\hat{\beta} \tag{C.20}$$

$$\hat{\alpha} = 35 - \frac{36}{T_{rm}} - 96.736\log T_{rm} + T_{rm}^6 \tag{C.21}$$

$$\hat{\beta} = \log(T_{rm}) + 0.0372175\hat{\alpha} \tag{C.22}$$

According to BRILL and MUKHERJEE (1999), if nitrogen or hydrogen is present in the fluid, Eqs. C.23 and C.24 must be used to calculate T_{cm} and $w_{SRK\,m}$, respectively.

$$T_{cm} = \frac{\sum_{i=1}^{N} x_i^L V_i^{\circ} T_{ci}}{\sum_{i=1}^{N} x_i^L V_i^{\circ}} \tag{C.23}$$

$$w_{SRK\,m} = \frac{\sum_{i=1}^{N} x_i^L V_i^{\circ} w_{SRK\,i}}{\sum_{i=1}^{N} x_i^L V_i^{\circ}} \tag{C.24}$$

C.1.2 Viscosity

In this work, the correlation proposed by LOHRENZ *et al.* (1964) was used to calculate the viscosity of the liquid phase (μ_l in $Pa.s$), shown in Eq. C.25.

$$\begin{aligned} \mu_l =& 10^{-3} \times \{\mu_{ol} + {\epsilon_m}^{-1}[(0.1023 + 0.023364\rho_{rl} + 0.058533{\rho_{rl}}^2 - 0.040758{\rho_{rl}}^3 + \\ & 0.0093724{\rho_{rl}}^4)^4 - 0.0001]\} \end{aligned} \tag{C.25}$$

where ϵ_m is the mixture viscosity parameter in the liquid phase, shown in Eq.C.26; ρ_{rl} is the reduced density of the liquid phase, shown in Eq. C.27, and μ_{ol} liquid mixture viscosity at atmospheric pressure, shown in Eq. C.28.

$$\epsilon_m = \frac{2173.5{T_{cl}}^{1/6}}{\sqrt{MM_l}{P_{cl}}^{2/3}} \tag{C.26}$$

$$\rho_{rl} = \frac{\rho_l V_{cl}}{MM_l} \tag{C.27}$$

$$\mu_{ol} = \frac{\sum_{i=1}^{n} x_i \mu_{oi} \sqrt{MM_i}}{\sum_{i=1}^{n} x_i \sqrt{MM_i}} \tag{C.28}$$

where μ_{oi} is the viscosity of component i at atmospheric pressure, given in Eq. C.29;and T_{cl}, P_{cl}, and V_{cl} are the critical temperature, pressure, and volume , respectively, of the liquid phase, given by the mixing rule given in Eqs. C.31 - C.33.

$$\mu_{oi} = \begin{cases} \frac{34\times10^{-5}{T_{ri}}^{0.94}}{\epsilon_i}, & T_{ri} \leq 1.5 \\ \frac{17.78\times10^{-5}(T_{ri}-1.67)^{0.625}}{\epsilon_i}, & T_{ri} > 1.5 \end{cases} \tag{C.29}$$

where ϵ_i is the mixture viscosity parameter of component i, given by Eq. C.30.

$$\epsilon_i = \frac{2173.5{T_{ci}}^{1/6}}{MM_i{P_{ci}}^{2/3}} \tag{C.30}$$

$$T_{cl} = \sum_{i=1}^{n} x_i T_{ci} \tag{C.31}$$

$$P_{cl} = \sum_{i=1}^{n} x_i P_{ci} \tag{C.32}$$

$$V_{cl} = \sum_{i=1, i\neq C_{7+}}^{n} x_i V_{ci} MM_i + V_{cC_{7+}} \tag{C.33}$$

where

$$V_{cC_{7+}} = \left(21.573 + 0.015122 MM_{C_{7+}} - 27.656 SG_{C_{7+}} + 0.070615 SG_{C_{7+}} MM_{C_{7+}}\right) \times \frac{0.0624279606}{MM_{C_{7+}}} \tag{C.34}$$

where V_{ci} e $V_{cC_{7+}}$ are the critical volume of the component i and pseudocomponent, respectively, and $SG_{C_{7+}}$ is the specific gravity of the pseudocomponent, shown by

Eq. C.35.

$$SG_{C_{7+}} = \frac{\rho_{C_{7+}}}{\rho_{H_2O}} \tag{C.35}$$

where $\rho_{C_{7+}}$ and ρ_{H_2O} are the density of the pseudocomponent and water, respectively. In this work, ρ_{H_2O} equals to 997 kg/m^3.

The variables MM_l and MM_i must be in g/mol to calculate the viscosity of the liquid phase.

The viscosity of the liquid and vapor phases are not a direct variable of the DFM, however, this variable is used as an input parameter of DFM parameters algorithm proposed by BHAGWAT and GHAJAR (2014). Also, it is used to calculate F_{mw}.

C.1.3 Superficial Tension

To calculate the surface tension of the liquid phase (σ_l in kg/s^2) of a a hydrocarbon mixture, DAUBERT and DANNER (1997) suggests the use of Eq. C.36.

$$\sigma_l = \left\{ \sum_{i=1}^{n} \left[PAR_i \left(\frac{\rho_l}{MM_l} x_i - \frac{\rho_v}{MM_v} y_i \right) \right] \right\}^4 \times 10^{-3} \tag{C.36}$$

where PAR_i is the Parachor value of component i available in QUAYLE (1953).

To calculate the surface tension of the liquid phase in kg/s^2, ρ_l and ρ_v must be in g/cm^3 and the molar mass of the phases, MM_l and MM_v, in g/mol.

C.2 Vapor Phase

To calculate the physical properties of the vapor phase, the molar mass of the this phase (MM_v in kg/mol) is calculated, as shown by Eq. C.37.

$$MM_v = \sum_{i=1}^{n} y_i MM_i \tag{C.37}$$

C.2.1 Density

As a result of the VLE, the compressibility factor of the vapor phase is known, Z_v. Then, the density of the vapor phase is calculated using Eq. C.38.

$$\rho_v = \frac{PMM_v}{Z_v RT} \tag{C.38}$$

C.2.2 Viscosity

According to RIAZI (2005), the correlation proposed by LEE *et al.* (1966) for the calculation of the vapor phase viscosity (μ_v in $Pa.s$), as shown by Eqs. C.39 - C.42, is widely used.

$$\mu_v = 10^{-7} \times \left\{ K \exp\left[\left(10^{-3}\rho_v\right)^Y X \right] \right\} \tag{C.39}$$

where

$$K = \frac{(9.4 + 0.02MM_v)\, 9/5T^{1.5}}{209 + 19MM_v + (9.5)T} \tag{C.40}$$

$$Y = 2.4 - 0.2X \tag{C.41}$$

$$X = 3.5 + \frac{248}{T} + 0.01MM_v \tag{C.42}$$

where X, K, and Y are parameters used to calculate the viscosity of the vapor phase.

To calculate the viscosity of the vapor phase, the density of this phase (MM_v) must be in g/mol.

C.2.3 Velocity

The velocity of the vapor phase in the DFM, (v_v in m/s), is calculated using Eq. C.43.

$$v_v = v_m - \frac{\rho_l \hat{v}_v^{des}}{\rho_m} \tag{C.43}$$

C.3 Mixture

Since the DFM, also known as the Mixture Model, is based on mixture balance equations, there is a need to calculate the properties of the mixture given the physical properties of each phase calculated in Sections C.1 and C.2.

C.3.1 Density

The mixture density (ρ_m in kg/m^3) is calculated as shown by Eq. C.44.

$$\rho_m = \alpha_v \rho_v + (1 - \alpha_v)\rho_l \tag{C.44}$$

C.3.2 Enthalpy

The mixture enthalpy (h_m in J/kg) is given by Eq. C.45.

$$h_m = \frac{\alpha_v \rho_v h_v + (1 - \alpha_v)\rho_l h_l}{\rho_m} \tag{C.45}$$

Appendix D

Drift-Flux Model Parameters

The parameters of the Drift-Flux Model, $\left\langle \hat{v}_v^{des} \right\rangle$ and C_0, are calculated as a function of the fluid flow regime. BHAGWAT and GHAJAR (2014) stated that the model accuracy is low and developed a set of correlations independent of the flow regime, as shown by the procedure described in this section.

The dimensionless parameter, C_0, is calculated as shown by Eq. D.1.

$$C_0 = \frac{2 - (\rho_v/\rho_l)^2}{1 + (Re_{tp}/1000)^2} + \frac{\left\{ \left(\sqrt{\left[1 + (\rho_v/\rho_l)^2 \cos\theta\right] / \left[1 + \cos\theta\right]} \right)^{1-\alpha_v} \right\}^{2/5} + C_{0,1}}{1 + (1000/Re_{tp})^2} \tag{D.1}$$

where Re_{tp} is the Reynolds Number of the two-phase fluid, Eq. D.2, and $C_{0,1}$ is a parameter given by Eq. D.3.

$$Re_{tp} = \frac{\langle j_m \rangle \, \rho_l d_i}{\mu_l} \tag{D.2}$$

where $\langle j_m \rangle$ is the mixture superficial velocity, sum of the superficial velocities of the liquid and vapor phases, $\langle j_l \rangle$ and $\langle j_v \rangle$, respectively.

$$C_{0,1} = \begin{cases} 0, & \begin{array}{l} 0^\circ \geq \theta \geq -50^\circ \\ \text{e } Fr_{sg} \leq 0,1 \end{array} \\ \left(0,2 - 0,2\sqrt{\rho_v/\rho_l}\right)\left[(2,6-\beta_{tp})^{0,15} - \sqrt{f_{tp}}\right], & \text{otherwise} \\ \times\left(1-\chi_{tp}\right) & \end{cases} \tag{D.3}$$

where β_{tp} is the volumetric flow fraction of the vapor phase, χ_{tp} is the two phase flow quality, f_{tp} is the two phase friction factor, and Fr_{sg} is the Froude number.

The variables β_{tp}, χ_{tp}, f_{tp} e Fr_{sg} are calculated as shown by Eqs. D.4, D.5, D.6, and D.7, respectively.

$$\beta_{tp} = \frac{\langle j_v \rangle}{\langle j_v \rangle + \langle j_l \rangle} \tag{D.4}$$

$$\chi_{tp} = \frac{\rho_v \langle j_v \rangle}{\rho_v \langle j_v \rangle + \rho_l \langle j_l \rangle} \tag{D.5}$$

$$f_{tp} = \left\{ -2 \times \log_{10}\left\{ \frac{\kappa}{3,7065 d_i} - \frac{5,0452}{Re_{tp}} \log_{10}\left[\frac{(\kappa/d_i)^{1,1098}}{2,8257} + \left(\frac{7,149}{Re_{tp}}\right)^{0,8981} \right] \right\} \right\}^{-2} \tag{D.6}$$

$$Fr_{sg} = \sqrt{\frac{\rho_v}{\rho_l - \rho_v}} \frac{\langle j_v \rangle}{\sqrt{g d_i \cos\theta}} \tag{D.7}$$

The parameter $\left\langle \hat{v}_v^{des} \right\rangle$, in m/s, is calculated as shown by Eq. D.8.

$$\left\langle \hat{v}_v^{des} \right\rangle = (0,35 \sin\theta + 0,45\cos\theta) \times \sqrt{\frac{g d_i (\rho_l - \rho_v)}{\rho_l}} (1-\alpha_v)^{0,5} C_2 C_3 C_4 \tag{D.8}$$

where C_2, C_3 e C_4 are variables defined by Eqs. D.9, D.10 e D.11, respectively.

$$C_2 = \begin{cases} \left(\frac{0,434}{\log_{10}(\mu_l/0,001)}\right)^{0,15}, & (\mu_l/0,001) > 10 \\ 1, & \text{caso contrário} \end{cases} \tag{D.9}$$

$$C_3 = \begin{cases} (La/0,025)^{0,9}, & La < 0,025 \\ 1, & \text{caso contrário} \end{cases} \tag{D.10}$$

$$C_4 = \begin{cases} -1, & 0^\circ \geq \theta \geq -50^\circ \text{e } Fr_{sg} \leq 0,1 \\ 1, & \text{caso contrário} \end{cases} \tag{D.11}$$

where La is defined by Eq. D.12.

$$La = \frac{\sqrt{\sigma_l / g\left(\rho_l - \rho_v\right)}}{d_i} \tag{D.12}$$

The procedure described in this section was used in this work to calculate the parameters of the Drift-Flux Model.

Appendix E

Multiple Solid Solutions Model

From the thermodynamic point of view, the liquid and solid phases are in equilibrium conditions if the fugacities of each component i are the same, as shown by Eq. E.1 (PRAUSNITZ *et al.*, 1986).

$$\hat{f}_i^L\left(T, P, \underline{x}^L\right) = \hat{f}_i^S\left(T, P, \underline{x}^S\right) \tag{E.1}$$

where T and P are the system pressure and temperature, respectively; $\hat{f}_i^S$ and $\hat{f}_i^L$ are the fugacities of component i in the solid and liquid phases, respectively; and $\underline{x}^L$ and $\underline{x}^S$ are vectors of the compositions of components in the liquid and solid phases, respectively.

According to PRAUSNITZ *et al.* (1986), the solid phase may be described by an activity coefficient model, and the liquid phase can be described by an equation of state, as shown by Eqs. E.2 and E.3.

$$\hat{f}_i^L\left(T, P, \underline{x}^L\right) = x_i^L \hat{\varphi}_i^L P \tag{E.2}$$

$$\hat{f}_i^S\left(T, P, \underline{x}^S\right) = x_i^S \gamma_i^S f_{i,pure}^S \tag{E.3}$$

where x_i^L and x_i^S are the composition of component i in the liquid and solid phase, respectively; $\hat{\varphi}_i^L$ is the fugacity coefficient of component i in the liquid phase; and γ_i^S and $f_{i,pure}^S$ are the activity coefficient and fugacity of pure component i, respectively, in the solid phase.

The fugacity of component i in the solid phase may be calculated using Eq. E.4.

$$f_{i,pure}^{S} = \varphi_i^L P \times \exp\left[\frac{\Delta h_i^f}{RT}\left(1 - \frac{T}{T_i^f}\right) + \frac{\Delta h_i^{tr}}{RT}\left(\frac{T}{T_i^{tr}} - 1\right)\right] \tag{E.4}$$

where φ_i^L is the fugacity coefficient of pure component i in the liquid phase, R is the real gases constant, T_i^f and T_i^{tr} are the fusion and solid-solid transition temperature of component i, Δh_i^f and Δh_i^{tr} are the fusion and solid-solid transition variation of enthalpy.

The solid-liquid equilibrium is represented in terms of K values, as shown by Eq. E.5, by combining Eqs. E.1-E.4.

$$K_i^{SL} = \frac{x_i^S}{x_i^L} = \frac{\hat{\varphi}_i^L}{\varphi_i^L \gamma_i^S} \times \exp\left[\frac{\Delta h_i^f}{RT}\left(1 - \frac{T}{T_i^f}\right) + \frac{\Delta h_i^{tr}}{RT}\left(\frac{T}{T_i^{tr}} - 1\right)\right] \tag{E.5}$$

In this work, it was used the correlations suggested by Goes et al. (2022). These authors conducted experiments to measure a new set of thermophysical properties for pure n-alkanes with carbon number ranging from 17 to 50 and compared it with the existing correlations in the literature. Goes et al. (2022) suggested the use of Won's correlation (WON, 1986) to calculate T_i^f, the correlation proposed by **?** to calculate Δh_i^f, and the correlation proposed by **?** to calculate T_i^{tr}. Regarding Δh_i^{tr} predictions, these authors suggested a new set of correlations. The use of this group of correlations may enhance the accuracy of the thermodynamic model, since previous works (COUTINHO *et al.*, 2006; **?**; **?**) used inaccurate correlations to calculate thermophysical properties.

The activity coefficient of the liquid phase was calculated using modified UNIQUAC model.

$$\begin{aligned} \ln \gamma_i^S = & \ln\left(\frac{\Phi_i}{x_i^S}\right) + 1 - \frac{\Phi_i}{x_i^S} - \frac{Z}{2} q_i \left[\ln\left(\frac{\Phi_i}{\theta_i}\right) + 1 - \frac{\Phi_i}{\theta_i}\right] + q_i \\ & - q_i \ln\left(\sum_{j=1}^{N_c} \theta_j \tau_{ji}\right) - q_i \sum_{j=1}^{N_c} \frac{\theta_j \tau_{ij}}{\sum_{w=1}^{N_c} \theta_w \tau_{wj}} \end{aligned} \tag{E.6}$$

where Φ_i and θ_i are the surface and volume fraction, respectively, of component i, given by Eqs. E.7 and E.8, τ_{ji} is a model parameter given by Eq. E.9.

$$\Phi_i = \frac{x_i r_i}{\sum_{j=1}^{N_c} x_j r_j} \tag{E.7}$$

$$\theta_i = \frac{x_i q_i}{\sum_{j=1}^{N_c} x_j q_j} \tag{E.8}$$

$$\tau_{ji} = \exp\left(-\frac{\lambda_{ji} - \lambda_{ii}}{q_i RT}\right) \tag{E.9}$$

where q_i and r_i are the structural parameters of the modified UNIQUAC model (COUTINHO *et al.*, 2006), given by Eqs. E.10 and E.11.

$$r_i = 0.1Cn_i + 0.0672 \tag{E.10}$$

$$q_i = 0.1Cn_i + 0.1141 \tag{E.11}$$

This model requires the estimation of the interaction energies, λ_{ii}, as defined by COUTINHO *et al.* (2006).

$$\lambda_{ii} = -\frac{2}{Z}\left(\Delta H^{sub}_{i\,pure} - RT\right) \tag{E.12}$$

Appendix F

Complementary Material

Table F.1: Global composition of the volate oil adapted from WHITSON and BRULÉ (2000) and pure component properties.

Component	Global comp. (%mole)	MW (g/mol)	Tc (K)	Pc (Pa)	ω (-)	V_c $\times 10^{-3}$ (m^3/kg)	P_{ch} (-)
Nitrogen	0.21	28.01	126.19	3395800	0.0372	3.1918	60.1
Carbon dioxide	5.93	44.00	304.13	7377300	0.223	2.1386	72.2
Methane	58.77	16.04	190.56	4599200	0.0104	6.1478	72.60
Ethane	7.57	30.07	305.33	4871800	0.0991	4.8407	110
Propane	4.09	44.10	369.85	4247660	0.152	4.5356	150.8
i-Butane	0.91	58.12	407.85	3640000	0.1844	4.4573	191.7
n-Butane	2.09	58.12	425.16	3796000	0.1985	4.3891	190.3
i-Pentane	0.77	72.15	460.45	3377000	0.227	4.2412	229.4
n-Pentane	1.15	72.15	469.7	3366500	0.2513	4.3103	231
Hexane	1.75	86.17	507.82	3018100	0.2979	4.2885	271
C_{7+}	16.76	228	732.07	1668194	0.6740	3.9791	575.984

Table F.2: Global composition of the oil obtained from GÓES *et al.* (2022) and its pure component properties.

Component	Global comp. (%mole)	MW (g/mol)	Tc (K)	Pc (Pa)	ω (-)	V_c $\times 10^{-3}$ (m^3/kg)	P_{ch} (-)
Nitrogen	0.8053	28.01	126.19	3395800	0.0372	3.1918	60.10
Carbon dioxide	14.3506	44.01	304.13	7377300	0.223	2.1386	72.20
Methane	44.5009	16.04	190.56	4599200	0.0104	6.1478	72.60
Ethane	5.9700	30.07	305.33	4871800	0.0991	4.8407	110.00
Propane	3.3363	44.10	369.85	4247660	0.152	4.5356	150.80
i-Butane	0.7291	58.12	407.85	3640000	0.1844	4.4573	191.70
n-Butane	1.1084	58.12	425.16	3796000	0.1985	4.3891	190.30
i-Pentane	0.4426	72.15	460.45	3377000	0.227	4.2412	229.40
n-Pentane	0.5064	72.15	469.70	3366500	0.2513	4.3103	231.00
Hexane	0.4519	86.18	507.82	3018100	0.2979	4.2885	271.00
n-Heptane	0.4532	100.20	540.13	1668194	0.6740	4.3103	311.00
n-Octane	0.4111	114.23	569.32	2497000	0.3960	4.2571	351.40
n-Nonane	0.3615	128.26	594.60	2288000	0.4450	4.2726	390.00
n-Decane	0.2977	142.28	617.70	2120000	0.4890	4.2380	431.00
Pseudo1	25.1328	145.99	645.90	2570264	0.4494	3.8722	396.91
Pseudo2	0.9954	161.93	668.96	2384934	0.4907	3.8843	435.19
Pseudo3	0.1002	176.09	688.21	2236105	0.5274	3.8967	470.92
Pseudo4	0.0169	190.15	705.83	2105310	0.5625	3.9096	506.93
Pseudo5	0.0082	204.19	722.12	1989462	0.5964	3.9227	543.26
Pseudo6	0.0072	218.21	737.26	1886256	0.6290	3.9357	579.88
Pseudo7	0.0071	232.23	751.42	1793727	0.6604	3.9486	616.83
Pseudo8	0.0071	255.93	768.81	1685505	0.7001	3.9652	666.01

Table F.3: Dimensions and thermal properties of Well 1 for the real offshore gas and oil production pipeline.

Section	Length (m)	ID (m)	Inclination (°)	U_{heat} $W/m^2/K$	T_{neigh} $(°C)$
1	299.80	0.152	-0.21	3.91	2.9
2	500.00	0.152	-0.06	3.91	2.9
3	399.40	0.152	0.00	3.91	2.9
4	100.00	0.152	0.52	3.91	2.9
5	200.10	0.152	0.23	3.91	2.9
6	99.91	0.152	0.63	3.91	2.9
7	99.91	0.152	0.80	3.91	2.9
8	99.96	0.152	1.95	3.91	2.9
9	200.31	0.152	0.60	3.91	2.9

Section	Length (m)	ID (m)	Inclination (°)	U_{heat} $(W/m^2/K)$	T_{neigh} $(°C)$
10	100.00	0.152	0.34	4.08	2.9
11	50.80	0.152	-0.45	4.08	2.9
12	51.32	0.152	-1.67	4.08	2.9
13	250.60	0.152	-0.18	4.08	2.9
14	192.80	0.152	-0.24	4.08	2.9
15	199.80	0.152	-0.23	4.08	2.9
16	299.70	0.152	-0.04	4.08	2.9
17	203.83	0.152	7.90	4.08	2.9
18	70.30	0.152	35.68	4.08	2.9
19	71.49	0.152	25.17	4.08	3.3
20	59.33	0.152	45.75	4.08	3.4
21	71.52	0.152	43.24	4.08	3.5
22	78.88	0.119	43.20	4.08	3.6
23	85.49	0.119	45.52	4.08	3.7
24	110.18	0.147	53.01	22.61	3.8
25	137.96	0.147	47.61	18.47	3.8
26	119.29	0.147	27.51	23.59	3.8
27	79.79	0.147	43.58	23.56	3.8
28	76.50	0.147	40.81	28.53	3.7
29	66.61	0.147	37.99	28.51	3.6
30	92.95	0.119	60.62	28.51	3.6
31	103.97	0.147	19.67	34.53	3.4
32	61.98	0.147	10.22	28.46	3.4
33	52.15	0.147	-27.40	28.44	3.4
34	83.51	0.147	0.69	28.41	3.4
35	52.20	0.147	16.70	28.39	3.4
36	70.91	0.147	42.60	28.56	3.4
37	114.62	0.147	42.21	28.50	3.3
38	143.76	0.147	46.92	28.45	3.3
39	186.42	0.147	50.33	27.37	3.4
40	334.31	0.119	62.78	27.70	3.8
41	425.71	0.119	44.30	33.10	6.3
42	417.71	0.119	43.82	28.78	11.7
43	299.18	0.119	13.10	17.63	20
44	72.64	0.217	20.13	22.82	22.5
45	25.00	0.217	0.23	22.82	23

Appendix G

Supplementary Material

The data given in the Well Test Reports, Gas Chromatographic Analysis, and PVT Analysis for Well 1 are given in Tables G.1 and G.2, respectively.

Table G.1: Data given in the Well Test Reports of Well 1.

Well	γ_o	Q_o^{SC}	Q_g^{SC}	$1/B_o$	γ_g	T^{sep}	P^{sep}	Rs
Test	kg/m^3	Nm^3/d	Nm^3/d	-	-	K	kPa	-
1	860.5	4321.00	1445509	0.945	0.891	299.15	1625.0	18.43
2	870.7	4211.59	1389916	0.941	0.922	312.15	1850.0	21.70
3	858.9	4137.58	1406570	0.955	0.904	317.25	1792.4	18.34
4	858.0	4053.12	1413977	0.945	0.917	312.65	1780.0	19.56
5	861.8	3994.3	1417713	0.944	0.901	318.15	1750.0	17.26
6	857.8	3997.83	1438122	0.940	0.905	317.35	1760.0	18.90
7	859.7	3972.78	1448270	0.940	1.013	317.15	1770.0	15.95
8	863.9	3996.45	1476676	0.932	0.900	316.75	1735.0	19.56
9	865.0	3932.49	1549271	0.932	0.892	315.55	1758.0	20.75

Table G.2: Data given in the Gas Chromatographic Analysis of Well 1.

	Well Test								
	1	2	3	4	5	6	7	8	9
Carbon dioxide	21.41	18.88	20.92	19.90	20.11	20.11	19.88	20.48	20.50
Nitrogen	0.74	0.65	0.75	0.74	0.74	0.78	0.68	0.76	0.77
Methane	63.79	61.83	62.53	62.72	63.14	63.14	57.52	62.93	63.29
Ethane	7.63	9.01	8.11	8.15	8.19	8.15	8	8.12	8.11
Propane	3.79	5.48	4.52	4.54	4.53	4.39	5.54	4.51	4.44
i-Butane	0.55	0.84	0.69	0.71	0.69	0.67	1.19	0.69	0.67
n-Butane	0.99	1.60	1.30	1.31	1.25	1.21	2.64	1.26	1.21
i-Pentane	0.22	0.32	0.25	0.31	0.27	0.26	0.79	0.28	0.25
n-Pentane	0.27	0.39	0.34	0.42	0.35	0.35	1.29	0.36	0.32
n-Hexane	0.2	0.22	0.2	0.35	0.23	0.27	1.05	0.24	0.19
n-Heptane	0.17	0.18	0.15	0.34	0.17	0.27	0.79	0.18	0.12
n-Octane	0.12	0.23	0.12	0.28	0.13	0.21	0.41	0.11	0.06
n-Nonane	0.08	0.26	0.09	0.16	0.11	0.14	0.14	0.06	0.04
n-Decane	0.04	0.11	0.03	0.07	0.09	0.05	0.08	0.02	0.03

The initial estimate for the wellstream composition and molar mass of each component are showed in Tables G.3 and G.4, respectively, when calculating $M_{C_{11+}}$ using the correlation given by LASATER (1958).

Table G.3: Initial estimate for the wellstream composition of the mixture when using correlation given by LASATER (1958) for calculating $M_{C_{11+}}$ of Well 1.

	Global composition (%)								
	1	2	3	4	5	6	7	8	9
Nitrogen	0.77	0.70	0.78	0.77	0.77	0.80	0.72	0.78	0.79
Carbon dioxide	17.43	15.43	17.07	16.31	16.57	16.57	16.44	17.00	17.20
Methane	51.58	50.14	50.67	51.05	51.67	51.67	47.27	51.92	52.80
Ethane	6.32	7.45	6.72	6.78	6.84	6.81	6.71	6.84	6.90
Propane	3.23	4.60	3.82	3.85	3.86	3.74	4.70	3.87	3.84
i-Butane	0.62	0.85	0.73	0.74	0.73	0.71	1.13	0.72	0.71
n-Butane	0.97	1.46	1.22	1.23	1.18	1.15	2.32	1.19	1.16
i-Pentane	0.35	0.43	0.37	0.42	0.38	0.37	0.81	0.39	0.36
n-Pentane	0.39	0.49	0.44	0.51	0.45	0.45	1.22	0.45	0.42
n-Hexane	0.33	0.35	0.33	0.45	0.35	0.38	1.02	0.35	0.31
n-Heptane	0.31	0.32	0.29	0.44	0.30	0.38	0.81	0.31	0.25
n-Octane	0.27	0.36	0.27	0.39	0.27	0.33	0.50	0.25	0.20
n-Nonane	0.24	0.38	0.24	0.30	0.25	0.28	0.27	0.21	0.18
n-Decane	0.20	0.26	0.19	0.22	0.24	0.20	0.23	0.17	0.17
Pseudo1	4.02	3.78	4.02	3.97	3.80	3.88	3.77	3.62	3.40
Pseudo2	1.59	1.50	1.59	1.56	1.50	1.53	1.49	1.43	1.35
Pseudo3	1.17	1.11	1.17	1.15	1.10	1.12	1.09	1.05	0.99
Pseudo4	0.94	0.90	0.94	0.93	0.89	0.91	0.88	0.85	0.81
Pseudo5	0.80	0.76	0.79	0.78	0.75	0.76	0.75	0.72	0.68
Pseudo6	0.69	0.67	0.69	0.68	0.65	0.66	0.65	0.63	0.59
Pseudo7	0.61	0.59	0.60	0.59	0.58	0.58	0.57	0.55	0.52
Pseudo8	7.18	7.48	7.05	6.88	6.87	6.70	6.66	6.69	6.37

Table G.4: Molar mass of the mixture components when using correlation given by LASATER (1958) for calculating $M_{C_{11+}}$ of Well 1.

	Molar mass (g/mol)								
	1	2	3	4	5	6	7	8	9
Nitrogen	28.01	28.01	28.01	28.01	28.01	28.01	28.01	28.01	28.01
Carbon dioxide	44.01	44.01	44.01	44.01	44.01	44.01	44.01	44.01	44.01
Methane	16.04	16.04	16.04	16.04	16.04	16.04	16.04	16.04	16.04
Ethane	30.07	30.07	30.07	30.07	30.07	30.07	30.07	30.07	30.07
Propane	44.10	44.10	44.10	44.10	44.10	44.10	44.10	44.10	44.10
i-Butane	58.12	58.12	58.12	58.12	58.12	58.12	58.12	58.12	58.12
n-Butane	58.12	58.12	58.12	58.12	58.12	58.12	58.12	58.12	58.12
i-Pentane	72.15	72.15	72.15	72.15	72.15	72.15	72.15	72.15	72.15
n-Pentane	72.15	72.15	72.15	72.15	72.15	72.15	72.15	72.15	72.15
n-Hexane	86.18	86.18	86.18	86.18	86.18	86.18	86.18	86.18	86.18
n-Heptane	100.20	100.20	100.20	100.20	100.20	100.20	100.20	100.20	100.20
n-Octane	114.23	114.23	114.23	114.23	114.23	114.23	114.23	114.23	114.23
n-Nonane	128.26	128.26	128.26	128.26	128.26	128.26	128.26	128.26	128.26
n-Decane	142.28	142.28	142.28	142.28	142.28	142.28	142.28	142.28	142.28
Pseudo1	146.89	146.90	146.89	146.89	146.89	146.89	146.89	146.90	146.90
Pseudo2	162.83	162.84	162.83	162.83	162.83	162.83	162.83	162.83	162.83
Pseudo3	176.99	177.00	176.99	176.99	177.00	176.99	176.99	177.00	177.00
Pseudo4	191.06	191.07	191.06	191.06	191.06	191.06	191.06	191.06	191.07
Pseudo5	205.10	205.11	205.10	205.10	205.10	205.10	205.10	205.10	205.10
Pseudo6	219.12	219.13	219.12	219.12	219.12	219.12	219.12	219.13	219.13
Pseudo7	233.14	233.15	233.14	233.14	233.14	233.14	233.14	233.14	233.14
Pseudo8	439.14	451.77	436.95	435.69	440.87	435.41	438.05	443.59	444.98

The initial estimate for the wellstream composition and molar mass of each component are showed in Tables G.5 and G.6, respectively, when calculating $M_{C_{11+}}$ using the correlation given by STANDING (1974).

Table G.5: Initial estimate for the wellstream composition of the mixture when using correlation given by STANDING (1974) for calculating $M_{C_{11+}}$ of Well 1.

	Global composition (%)								
	1	2	3	4	5	6	7	8	9
Nitrogen	0.78	0.71	0.79	0.78	0.78	0.81	0.73	0.79	0.80
Carbon dioxide	15.53	13.73	15.24	14.61	14.85	14.88	14.78	15.28	15.54
Methane	45.79	44.38	45.07	45.52	46.10	46.20	42.31	46.46	47.50
Ethane	5.70	6.68	6.06	6.13	6.19	6.17	6.09	6.20	6.28
Propane	2.96	4.16	3.49	3.52	3.53	3.43	4.29	3.55	3.54
i-Butane	0.64	0.85	0.74	0.76	0.74	0.73	1.11	0.74	0.72
n-Butane	0.96	1.39	1.18	1.19	1.15	1.12	2.17	1.16	1.13
i-Pentane	0.41	0.48	0.43	0.47	0.44	0.43	0.81	0.44	0.41
n-Pentane	0.44	0.53	0.49	0.55	0.49	0.49	1.18	0.50	0.46
n-Hexane	0.39	0.41	0.39	0.50	0.41	0.43	1.00	0.41	0.36
n-Heptane	0.37	0.38	0.36	0.49	0.36	0.43	0.81	0.36	0.31
n-Octane	0.34	0.41	0.33	0.45	0.33	0.39	0.53	0.31	0.27
n-Nonane	0.31	0.44	0.31	0.36	0.32	0.34	0.34	0.28	0.25
n-Decane	0.28	0.33	0.27	0.29	0.30	0.27	0.29	0.25	0.24
Pseudo1	13.77	12.88	13.79	13.63	13.05	13.35	13.00	12.47	11.80
Pseudo2	4.13	4.05	4.10	4.03	3.94	3.94	3.88	3.81	3.62
Pseudo3	2.38	2.44	2.34	2.29	2.29	2.24	2.23	2.23	2.13
Pseudo4	1.51	1.61	1.47	1.43	1.46	1.40	1.41	1.44	1.38
Pseudo5	1.00	1.12	0.97	0.94	0.97	0.92	0.93	0.97	0.94
Pseudo6	0.68	0.79	0.66	0.63	0.67	0.62	0.63	0.67	0.65
Pseudo7	0.47	0.57	0.45	0.43	0.47	0.42	0.44	0.47	0.46
Pseudo8	1.16	1.65	1.07	1.01	1.17	0.98	1.05	1.22	1.21

Table G.6: Molar mass of the mixture components when using correlation given by STANDING (1974) for calculating $M_{C_{11+}}$ of Well 1.

	Molar mass (g/mol)								
	1	2	3	4	5	6	7	8	9
Nitrogen	28.01	28.01	28.01	28.01	28.01	28.01	28.01	28.01	28.01
Carbon dioxide	44.01	44.01	44.01	44.01	44.01	44.01	44.01	44.01	44.01
Methane	16.04	16.04	16.04	16.04	16.04	16.04	16.04	16.04	16.04
Ethane	30.07	30.07	30.07	30.07	30.07	30.07	30.07	30.07	30.07
Propane	44.10	44.10	44.10	44.10	44.10	44.10	44.10	44.10	44.10
i-Butane	58.12	58.12	58.12	58.12	58.12	58.12	58.12	58.12	58.12
n-Butane	58.12	58.12	58.12	58.12	58.12	58.12	58.12	58.12	58.12
i-Pentane	72.15	72.15	72.15	72.15	72.15	72.15	72.15	72.15	72.15
n-Pentane	72.15	72.15	72.15	72.15	72.15	72.15	72.15	72.15	72.15
n-Hexane	86.18	86.18	86.18	86.18	86.18	86.18	86.18	86.18	86.18
n-Heptane	100.20	100.20	100.20	100.20	100.20	100.20	100.20	100.20	100.20
n-Octane	114.23	114.23	114.23	114.23	114.23	114.23	114.23	114.23	114.23
n-Nonane	128.26	128.26	128.26	128.26	128.26	128.26	128.26	128.26	128.26
n-Decane	142.28	142.28	142.28	142.28	142.28	142.28	142.28	142.28	142.28
Pseudo1	146.60	146.65	146.59	146.59	146.61	146.59	146.60	146.62	146.63
Pseudo2	162.55	162.60	162.54	162.54	162.56	162.53	162.55	162.57	162.57
Pseudo3	176.72	176.76	176.71	176.70	176.72	176.70	176.71	176.73	176.74
Pseudo4	190.78	190.83	190.77	190.77	190.79	190.77	190.78	190.80	190.81
Pseudo5	204.82	204.87	204.81	204.81	204.83	204.80	204.82	204.84	204.84
Pseudo6	218.84	218.89	218.83	218.83	218.85	218.83	218.84	218.86	218.87
Pseudo7	232.86	232.91	232.85	232.85	232.87	232.84	232.86	232.88	232.88
Pseudo8	283.22	290.00	282.13	281.51	284.10	281.37	282.67	285.51	286.25

The wellstream compositions given by HODA and WHITSON (2013)'s method when using the correlation proposed by LASATER (1958) and STANDING (1974) to calculate $M_{C_{11+}}$ of Well 1 are shown in Tables G.7 and G.8, respectively.

Table G.7: Wellstream composition of the mixture when using correlation proposed by LASATER (1958) for calculating $M_{C_{11+}}$ of Well 1 given by HODA and WHITSON's method

	Global composition (%)								
	1	2	3	4	5	6	7	8	9
Nitrogen	0.75	0.68	0.76	0.75	0.75	0.78	0.71	0.77	0.77
Carbon dioxide	17.00	15.10	16.65	15.97	16.20	16.21	16.20	16.63	16.84
Methane	50.31	49.07	49.43	49.97	50.50	50.55	46.56	50.76	51.68
Ethane	6.17	7.30	6.56	6.64	6.69	6.67	6.61	6.69	6.75
Propane	3.15	4.51	3.73	3.77	3.78	3.67	4.63	3.78	3.76
i-Butane	0.60	0.83	0.71	0.73	0.71	0.70	1.12	0.71	0.69
n-Butane	0.95	1.44	1.20	1.21	1.16	1.13	2.29	1.17	1.14
i-Pentane	0.34	0.42	0.37	0.41	0.38	0.37	0.80	0.38	0.35
n-Pentane	0.39	0.48	0.44	0.50	0.45	0.44	1.21	0.45	0.41
n-Hexane	0.34	0.35	0.34	0.46	0.36	0.39	1.03	0.36	0.31
n-Heptane	0.34	0.34	0.32	0.48	0.33	0.41	0.85	0.33	0.27
n-Octane	0.30	0.39	0.29	0.43	0.30	0.37	0.53	0.27	0.22
n-Nonane	0.26	0.42	0.27	0.32	0.28	0.30	0.29	0.23	0.20
n-Decane	0.23	0.28	0.22	0.24	0.26	0.22	0.24	0.19	0.19
Pseudo1	4.47	4.14	4.47	4.34	4.20	4.27	4.02	4.02	3.79
Pseudo2	1.77	1.65	1.76	1.71	1.66	1.69	1.59	1.59	1.50
Pseudo3	1.30	1.22	1.30	1.26	1.22	1.24	1.17	1.17	1.11
Pseudo4	1.05	0.99	1.05	1.02	0.99	1.00	0.94	0.95	0.90
Pseudo5	0.89	0.84	0.88	0.86	0.83	0.84	0.80	0.80	0.76
Pseudo6	0.77	0.73	0.76	0.74	0.72	0.73	0.69	0.70	0.66
Pseudo7	0.68	0.65	0.67	0.65	0.64	0.64	0.61	0.61	0.58
Pseudo8	7.98	8.18	7.83	7.54	7.60	7.39	7.11	7.43	7.10

Table G.8: Wellstream composition of the mixture when using correlation proposed by STANDING (1974) for calculating $M_{C_{11+}}$ of Well 1 given by HODA and WHITSON's method

	Global composition (%)								
	1	2	3	4	5	6	7	8	9
Nitrogen	0.77	0.71	0.78	0.77	0.77	0.80	0.74	0.78	0.79
Carbon dioxide	15.35	13.66	15.07	14.51	14.71	14.75	14.87	15.13	15.39
Methane	45.24	44.15	44.55	45.22	45.67	45.81	42.59	46.02	47.04
Ethane	5.63	6.65	5.99	6.09	6.13	6.12	6.13	6.14	6.22
Propane	2.92	4.14	3.45	3.50	3.50	3.41	4.31	3.52	3.51
i-Butane	0.64	0.85	0.74	0.75	0.74	0.72	1.11	0.73	0.72
n-Butane	0.95	1.39	1.17	1.18	1.14	1.11	2.17	1.15	1.12
i-Pentane	0.41	0.48	0.43	0.47	0.44	0.43	0.81	0.44	0.41
n-Pentane	0.44	0.53	0.49	0.55	0.49	0.49	1.18	0.50	0.46
n-Hexane	0.40	0.41	0.40	0.50	0.41	0.44	0.99	0.41	0.37
n-Heptane	0.38	0.38	0.36	0.50	0.37	0.44	0.80	0.37	0.32
n-Octane	0.35	0.42	0.34	0.45	0.34	0.40	0.53	0.32	0.27
n-Nonane	0.32	0.44	0.32	0.37	0.33	0.35	0.33	0.28	0.26
n-Decane	0.29	0.33	0.28	0.30	0.31	0.28	0.29	0.25	0.25
Pseudo1	14.21	13.06	14.22	13.87	13.39	13.67	12.76	12.82	12.16
Pseudo2	4.26	4.11	4.23	4.10	4.05	4.04	3.81	3.92	3.73
Pseudo3	2.46	2.47	2.41	2.33	2.35	2.29	2.19	2.29	2.20
Pseudo4	1.56	1.63	1.52	1.46	1.50	1.43	1.38	1.48	1.42
Pseudo5	1.03	1.13	1.00	0.96	1.00	0.94	0.91	1.00	0.96
Pseudo6	0.71	0.80	0.68	0.64	0.69	0.63	0.62	0.69	0.67
Pseudo7	0.49	0.58	0.47	0.44	0.48	0.43	0.43	0.49	0.48
Pseudo8	1.19	1.67	1.11	1.03	1.20	1.00	1.03	1.26	1.25

After applying the Gamma Distribution Function on the initial estimate of composition when using LASATER's correlation, the initial wellstream composition and the molar mass of each component are calculated, as shown in Tables G.9 and G.10, respectively. The final composition of this case is given in Table G.11.

Table G.9: Wellstream composition of the mixture when using correlation proposed by LASATER (1958) for calculating $M_{C_{11+}}$ of Well 1 given by HODA *et al.*'s method after applying the Gamma Distribution Function

	Global composition (%)								
	1	2	3	4	5	6	7	8	9
Nitrogen	0.80	0.72	0.81	0.80	0.80	0.83	0.75	0.81	0.82
Carbon dioxide	18.16	16.04	17.78	16.99	17.22	17.24	17.09	17.64	17.81
Methane	53.75	52.11	52.80	53.16	53.70	53.76	49.12	53.86	54.67
Ethane	6.59	7.75	7.00	7.06	7.11	7.09	6.98	7.09	7.14
Propane	3.36	4.78	3.98	4.01	4.01	3.90	4.88	4.01	3.98
i-Butane	0.64	0.88	0.76	0.77	0.75	0.74	1.18	0.75	0.73
n-Butane	1.01	1.52	1.27	1.28	1.23	1.20	2.41	1.24	1.20
i-Pentane	0.36	0.45	0.39	0.44	0.40	0.39	0.84	0.40	0.37
n-Pentane	0.41	0.51	0.46	0.53	0.47	0.47	1.26	0.47	0.43
n-Hexane	0.35	0.36	0.35	0.47	0.36	0.40	1.06	0.37	0.32
n-Heptane	0.32	0.33	0.30	0.46	0.31	0.40	0.84	0.32	0.26
n-Octane	0.28	0.37	0.28	0.41	0.28	0.35	0.52	0.26	0.21
n-Nonane	0.25	0.40	0.25	0.31	0.26	0.29	0.29	0.21	0.19
n-Decane	0.21	0.27	0.20	0.23	0.25	0.21	0.23	0.18	0.18
Pseudo1	0.00	0.00	0.00	0.00	0.00	0.00	0.00	0.00	0.00
Pseudo2	1.66	1.56	1.65	1.63	1.56	1.59	1.55	1.49	1.40
Pseudo3	1.22	1.15	1.22	1.20	1.15	1.17	1.14	1.09	1.03
Pseudo4	0.98	0.94	0.98	0.96	0.93	0.94	0.92	0.89	0.83
Pseudo5	0.83	0.79	0.83	0.81	0.78	0.79	0.77	0.75	0.71
Pseudo6	0.72	0.69	0.72	0.70	0.68	0.69	0.67	0.65	0.61
Pseudo7	0.63	0.61	0.63	0.62	0.60	0.60	0.59	0.57	0.54
Pseudo8	7.48	7.77	7.34	7.16	7.14	6.97	6.92	6.94	6.59

Table G.10: Mass molar of the components when using correlation proposed by LASATER (1958) for calculating $M_{C_{11+}}$ of Well 1 given by HODA *et al.*'s method after applying the Gamma Distribution Function

	Molar mass (g/mol)								
	1	2	3	4	5	6	7	8	9
Nitrogen	28.01	28.01	28.01	28.01	28.01	28.01	28.01	28.01	28.01
Carbon dioxide	44.01	44.01	44.01	44.01	44.01	44.01	44.01	44.01	44.01
Methane	16.04	16.04	16.04	16.04	16.04	16.04	16.04	16.04	16.04
Ethane	30.07	30.07	30.07	30.07	30.07	30.07	30.07	30.07	30.07
Propane	44.10	44.10	44.10	44.10	44.10	44.10	44.10	44.10	44.10
i-Butane	58.12	58.12	58.12	58.12	58.12	58.12	58.12	58.12	58.12
n-Butane	58.12	58.12	58.12	58.12	58.12	58.12	58.12	58.12	58.12
i-Pentane	72.15	72.15	72.15	72.15	72.15	72.15	72.15	72.15	72.15
n-Pentane	72.15	72.15	72.15	72.15	72.15	72.15	72.15	72.15	72.15
n-Hexane	86.18	86.18	86.18	86.18	86.18	86.18	86.18	86.18	86.18
n-Heptane	100.20	100.20	100.20	100.20	100.20	100.20	100.20	100.20	100.20
n-Octane	114.23	114.23	114.23	114.23	114.23	114.23	114.23	114.23	114.23
n-Nonane	128.26	128.26	128.26	128.26	128.26	128.26	128.26	128.26	128.26
n-Decane	142.28	142.28	142.28	142.28	142.28	142.28	142.28	142.28	142.28
Pseudo1	148.85	148.84	148.84	148.84	148.84	148.84	148.84	148.84	148.84
Pseudo2	164.33	164.33	164.33	164.33	164.33	164.33	164.33	164.33	164.33
Pseudo3	178.44	178.43	178.44	178.43	178.43	178.43	178.43	178.43	178.43
Pseudo4	192.48	192.48	192.48	192.48	192.48	192.48	192.48	192.48	192.48
Pseudo5	206.51	206.50	206.50	206.50	206.50	206.50	206.50	206.50	206.50
Pseudo6	220.52	220.52	220.52	220.52	220.52	220.52	220.52	220.52	220.52
Pseudo7	234.53	234.53	234.53	234.53	234.53	234.53	234.53	234.53	234.53
Pseudo8	249.01	249.01	249.00	249.03	249.02	249.03	249.02	249.01	249.03

Table G.11: Final wellstream composition of the mixture when using correlation proposed by LASATER (1958) for calculating $M_{C_{11+}}$ of Well 1 given by HODA *et al.*'s method

	Global composition (%)								
	1	2	3	4	5	6	7	8	9
Nitrogen	0.72	0.65	0.73	0.72	0.72	0.75	0.68	0.73	0.74
Carbon dioxide	16.32	14.42	16.00	15.36	15.56	15.62	15.58	15.98	16.21
Methane	48.25	46.81	47.48	48.04	48.50	48.66	44.77	48.76	49.72
Ethane	5.92	6.97	6.31	6.39	6.43	6.42	6.37	6.43	6.50
Propane	3.04	4.33	3.61	3.65	3.65	3.55	4.48	3.66	3.64
i-Butane	0.59	0.81	0.70	0.71	0.70	0.68	1.10	0.69	0.68
n-Butane	0.94	1.41	1.18	1.19	1.14	1.11	2.26	1.15	1.12
i-Pentane	0.35	0.43	0.38	0.42	0.39	0.38	0.82	0.39	0.36
n-Pentane	0.40	0.50	0.46	0.53	0.47	0.47	1.26	0.47	0.43
n-Hexane	0.40	0.42	0.40	0.54	0.42	0.46	1.22	0.43	0.37
n-Heptane	0.46	0.47	0.43	0.65	0.45	0.56	1.15	0.45	0.37
n-Octane	0.43	0.56	0.43	0.62	0.43	0.53	0.75	0.40	0.32
n-Nonane	0.39	0.61	0.40	0.47	0.41	0.45	0.42	0.34	0.30
n-Decane	0.34	0.42	0.32	0.36	0.39	0.33	0.35	0.29	0.29
Pseudo1	0.00	0.00	0.00	0.00	0.00	0.00	0.00	0.00	0.00
Pseudo2	2.63	2.45	2.62	2.53	2.47	2.50	2.31	2.38	2.26
Pseudo3	1.93	1.81	1.93	1.86	1.82	1.83	1.70	1.75	1.67
Pseudo4	1.56	1.47	1.55	1.50	1.47	1.48	1.37	1.42	1.35
Pseudo5	1.32	1.25	1.31	1.26	1.24	1.25	1.16	1.20	1.14
Pseudo6	1.14	1.08	1.13	1.09	1.08	1.08	1.00	1.04	0.99
Pseudo7	1.01	0.96	1.00	0.96	0.95	0.95	0.88	0.92	0.88
Pseudo8	11.87	12.17	11.64	11.12	11.31	10.95	10.36	11.12	10.67

After applying the Gamma Distribution Function on the initial estimate of composition when using STANDING's correlation, the initial wellstream composition and the molar mass of each component are calculated, as shown in Tables G.12 and G.13, respectively. The final composition of this case is given in Table G.14.

Table G.12: Wellstream composition of the mixture when using correlation proposed by STANDING (1974) for calculating $M_{C_{11+}}$ of Well 1 given by HODA *et al.*'s method after applying the Gamma Distribution Function

	Global composition (%)								
	1	2	3	4	5	6	7	8	9
Nitrogen	0.90	0.82	0.91	0.90	0.89	0.93	0.84	0.90	0.90
Carbon dioxide	18.02	15.76	17.68	16.91	17.07	17.17	16.98	17.45	17.61
Methane	53.10	50.94	52.27	52.70	53.02	53.32	48.63	53.08	53.86
Ethane	6.61	7.67	7.03	7.09	7.12	7.12	7.00	7.08	7.12
Propane	3.43	4.78	4.05	4.08	4.06	3.96	4.93	4.05	4.01
i-Butane	0.75	0.98	0.86	0.88	0.85	0.84	1.27	0.84	0.82
n-Butane	1.11	1.60	1.37	1.38	1.32	1.29	2.49	1.32	1.28
i-Pentane	0.47	0.55	0.50	0.54	0.50	0.49	0.93	0.50	0.46
n-Pentane	0.51	0.61	0.57	0.63	0.57	0.57	1.35	0.57	0.52
n-Hexane	0.46	0.47	0.45	0.57	0.47	0.50	1.15	0.47	0.41
n-Heptane	0.43	0.44	0.41	0.57	0.42	0.50	0.93	0.42	0.35
n-Octane	0.39	0.48	0.39	0.52	0.38	0.45	0.61	0.36	0.30
n-Nonane	0.36	0.50	0.36	0.42	0.37	0.39	0.39	0.32	0.28
n-Decane	0.32	0.38	0.31	0.34	0.35	0.32	0.34	0.28	0.28
Pseudo1	0.00	0.00	0.00	0.00	0.00	0.00	0.00	0.00	0.00
Pseudo2	4.79	4.65	4.75	4.66	4.53	4.55	4.46	4.35	4.11
Pseudo3	2.76	2.80	2.72	2.65	2.63	2.58	2.56	2.55	2.42
Pseudo4	1.75	1.85	1.71	1.66	1.68	1.62	1.62	1.64	1.56
Pseudo5	1.16	1.28	1.13	1.09	1.12	1.06	1.07	1.11	1.06
Pseudo6	0.79	0.91	0.76	0.73	0.77	0.71	0.73	0.77	0.74
Pseudo7	0.55	0.66	0.53	0.50	0.54	0.49	0.50	0.54	0.52
Pseudo8	1.34	1.89	1.24	1.17	1.34	1.13	1.21	1.40	1.37

Table G.13: Mass molar of the components when using correlation proposed by STANDING (1974) for calculating $M_{C_{11+}}$ of Well 1 given by HODA *et al.*'s method after applying the Gamma Distribution Function

	Mass molar (g/mol)								
	1	2	3	4	5	6	7	8	9
Nitrogen	28.01	28.01	28.01	28.01	28.01	28.01	28.01	28.01	28.01
Carbon dioxide	44.01	44.01	44.01	44.01	44.01	44.01	44.01	44.01	44.01
Methane	16.04	16.04	16.04	16.04	16.04	16.04	16.04	16.04	16.04
Ethane	30.07	30.07	30.07	30.07	30.07	30.07	30.07	30.07	30.07
Propane	44.10	44.10	44.10	44.10	44.10	44.10	44.10	44.10	44.10
i-Butane	58.12	58.12	58.12	58.12	58.12	58.12	58.12	58.12	58.12
n-Butane	58.12	58.12	58.12	58.12	58.12	58.12	58.12	58.12	58.12
i-Pentane	72.15	72.15	72.15	72.15	72.15	72.15	72.15	72.15	72.15
n-Pentane	72.15	72.15	72.15	72.15	72.15	72.15	72.15	72.15	72.15
n-Hexane	86.18	86.18	86.18	86.18	86.18	86.18	86.18	86.18	86.18
n-Heptane	100.20	100.20	100.20	100.20	100.20	100.20	100.20	100.20	100.20
n-Octane	114.23	114.23	114.23	114.23	114.23	114.23	114.23	114.23	114.23
n-Nonane	128.26	128.26	128.26	128.26	128.26	128.26	128.26	128.26	128.26
n-Decane	142.28	142.28	142.28	142.28	142.28	142.28	142.28	142.28	142.28
Pseudo1	148.75	148.77	148.74	148.74	148.75	148.74	148.75	148.75	148.76
Pseudo2	164.32	164.32	164.32	164.32	164.32	164.32	164.32	164.32	164.32
Pseudo3	178.44	178.44	178.43	178.43	178.44	178.43	178.43	178.44	178.44
Pseudo4	192.48	192.49	192.48	192.48	192.48	192.48	192.48	192.48	192.48
Pseudo5	206.51	206.51	206.51	206.51	206.51	206.51	206.51	206.51	206.51
Pseudo6	220.53	220.53	220.53	220.53	220.53	220.53	220.53	220.53	220.53
Pseudo7	234.54	234.54	234.54	234.54	234.54	234.54	234.54	234.54	234.54
Pseudo8	249.29	249.24	249.30	249.30	249.28	249.31	249.30	249.27	249.27

Table G.14: Final wellstream composition of the mixture when using correlation proposed by STANDING (1974) for calculating $M_{C_{11+}}$ of Well 1 given by HODA *et al.*'s method

	Global composition (%)								
	1	2	3	4	5	6	7	8	9
Nitrogen	0.78	0.72	0.79	0.79	0.78	0.81	0.74	0.80	0.80
Carbon dioxide	15.67	13.90	15.38	14.78	14.99	15.03	15.04	15.42	15.67
Methane	46.13	44.90	45.40	45.99	46.49	46.62	43.00	46.83	47.85
Ethane	5.75	6.78	6.12	6.21	6.26	6.24	6.20	6.26	6.34
Propane	3.01	4.26	3.56	3.60	3.60	3.50	4.40	3.61	3.60
i-Butane	0.67	0.89	0.77	0.79	0.77	0.76	1.16	0.77	0.75
n-Butane	1.01	1.47	1.25	1.26	1.21	1.18	2.30	1.22	1.18
i-Pentane	0.46	0.54	0.49	0.53	0.49	0.48	0.92	0.49	0.45
n-Pentane	0.52	0.62	0.58	0.64	0.58	0.58	1.38	0.58	0.53
n-Hexane	0.57	0.57	0.57	0.71	0.58	0.62	1.41	0.57	0.50
n-Heptane	0.67	0.63	0.64	0.87	0.64	0.78	1.38	0.63	0.54
n-Octane	0.65	0.74	0.65	0.86	0.64	0.76	0.97	0.59	0.50
n-Nonane	0.61	0.80	0.63	0.71	0.62	0.68	0.63	0.53	0.48
n-Decane	0.56	0.61	0.55	0.59	0.60	0.56	0.55	0.48	0.47
Pseudo1	0.00	0.00	0.00	0.00	0.00	0.00	0.00	0.00	0.00
Pseudo2	8.34	7.48	8.38	8.10	7.82	8.01	7.31	7.47	7.08
Pseudo3	4.81	4.50	4.79	4.61	4.53	4.55	4.20	4.38	4.17
Pseudo4	3.05	2.98	3.01	2.89	2.89	2.85	2.65	2.82	2.70
Pseudo5	2.03	2.06	1.99	1.89	1.93	1.87	1.76	1.90	1.83
Pseudo6	1.38	1.47	1.34	1.27	1.33	1.26	1.19	1.32	1.27
Pseudo7	0.96	1.06	0.93	0.87	0.93	0.86	0.83	0.93	0.90
Pseudo8	2.34	3.04	2.19	2.04	2.31	2.00	1.98	2.40	2.37

Table G.15 shows the results of PRE between the measured and calculated γ_g, GOR, and $^\circ API$ for Well 1 when using the method presented in HODA and WHITSON (2013) and HODA *et al.* (2017) when calculating $M_{C_{11+}}$ using the correlation given by LASATER (1958).

Table G.15: PRE for the results of Well 1 using the method proposed in HODA and WHITSON (2013) and HODA *et al.* (2017) when calculating $M_{C_{11+}}$ given by LASATER (1958)

	HODA and WHITSON (2013)			HODA *et al.* (2017)		
	LASATER (1958)					
	γ_g	GOR	$^\circ API$	γ_g	GOR	$^\circ API$
1	-0.52	-7.42×10^{-6}	55.86	-0.39	-2.12×10^{-5}	30.66
2	1.01	-1.08×10^{-5}	55.55	1.19	-3.62×10^{-5}	24.80
3	-0.46	-9.08×10^{-6}	55.59	-0.33	-2.68×10^{-5}	31.12
4	1.14	-1.40×10^{-5}	53.95	1.26	-4.17×10^{-5}	29.36
5	-0.02	-9.40×10^{-6}	55.54	0.12	-2.81×10^{-5}	29.51
6	0.50	-1.04×10^{-5}	54.52	0.61	-3.05×10^{-5}	30.27
7	3.16	-8.74×10^{-5}	51.11	3.41	-3.11×10^{4}	24.25
8	-0.46	-9.87×10^{-6}	56.21	-0.32	-2.94×10^{-5}	29.29
9	-0.80	-7.45×10^{-6}	56.75	-0.66	-2.25×10^{-5}	29.48

Regarding the results for Well 1, the degree of accuracy was low for all cases when analyzing the data for $^\circ API$, showing PREs higher than 10%, except for the Well Test Reports 2, 5, and 7 when using the correlation given by LASATER (1958), and the method proposed by HODA and WHITSON (2013).

When comparing the results between the method proposed by HODA and WHITSON (2013) and HODA *et al.* (2017) using the correlation given by LASATER (1958), HODA *et al.*'s method was capable to significantly decrease the PREs between the measured and calculated $^\circ API$. The indirect method proposed by HODA *et al.* (2017) includes in its methodology an iterative method called bisection algorithm to adjust the average molar mass of the pseudocomponents to match the measured $^\circ API$, since the results from the methodology proposed by HODA and WHITSON (2013) showed a significant systematic deviation from experimental data. In contrast, for the results related to the correlation given by STANDING (1974), the method proposed by HODA *et al.* (2017) showed higher PREs than HODA and WHITSON's model. In this last case, the adjustment required by the HODA *et al.*'s model was inefficient.

When comparing the results of Well 1, 2, and 3 with those using the methodology presented in HODA and WHITSON (2013) and HODA *et al.* (2017), it can be noticed an improvement of the °API predictions, especially when comparing the results using correlation proposed by LASATER (1958) to calculate the average molar mass of the pseudocomponents, which showed PREs greater than 50%.

The optimum initial estimate of composition, final wellstream composition, and molar mass of each component are showed in Tables G.16, G.17, and G.18, respectively.

Table G.16: Optimum initial wellstream composition of the mixture of Well 1 predicted using the method proposed in this work

	Global composition (%)								
	1	2	3	4	5	6	7	8	9
Nitrogen	0.78	0.72	0.79	0.78	0.78	0.81	0.74	0.79	0.80
Carbon dioxide	15.12	13.27	14.86	14.26	14.46	14.53	14.42	14.87	15.13
Methane	44.53	42.85	43.89	44.38	44.84	45.07	41.24	45.17	46.21
Ethane	5.56	6.48	5.92	5.99	6.04	6.04	5.95	6.05	6.13
Propane	2.90	4.05	3.42	3.45	3.46	3.37	4.20	3.47	3.46
i-Butane	0.65	0.85	0.75	0.76	0.74	0.73	1.10	0.74	0.73
n-Butane	0.95	1.37	1.17	1.18	1.14	1.11	2.13	1.15	1.12
i-Pentane	0.42	0.49	0.44	0.48	0.45	0.44	0.81	0.45	0.42
n-Pentane	0.46	0.54	0.50	0.56	0.50	0.50	1.17	0.51	0.47
n-Hexane	0.41	0.42	0.40	0.51	0.42	0.45	1.00	0.42	0.38
n-Heptane	0.39	0.40	0.37	0.50	0.38	0.45	0.81	0.38	0.33
n-Octane	0.35	0.43	0.35	0.46	0.35	0.40	0.54	0.33	0.28
n-Nonane	0.32	0.45	0.33	0.37	0.33	0.35	0.35	0.29	0.27
n-Decane	0.30	0.35	0.29	0.31	0.32	0.29	0.31	0.26	0.26
Pseudo1	21.58	21.95	21.31	20.91	20.71	20.45	20.26	20.17	19.28
Pseudo2	3.44	3.50	3.40	3.34	3.31	3.26	3.23	3.22	3.08
Pseudo3	1.14	1.15	1.12	1.10	1.09	1.08	1.07	1.06	1.02
Pseudo4	0.42	0.42	0.41	0.40	0.40	0.40	0.39	0.39	0.37
Pseudo5	0.16	0.17	0.16	0.16	0.16	0.15	0.15	0.15	0.15
Pseudo6	0.07	0.07	0.07	0.07	0.07	0.06	0.06	0.06	0.06
Pseudo7	0.03	0.03	0.03	0.03	0.03	0.03	0.03	0.03	0.03
Pseudo8	0.02	0.02	0.02	0.02	0.02	0.02	0.02	0.02	0.02

Table G.17: Final wellstream composition of the mixture of Well 1 calculated using the method proposed in this work

	Global composition (%)								
	1	2	3	4	5	6	7	8	9
Nitrogen	0.78	0.72	0.78	0.78	0.78	0.81	0.74	0.79	0.79
Carbon dioxide	14.92	13.44	14.63	14.11	14.34	14.35	14.71	14.64	15.04
Methane	43.92	43.41	43.18	43.91	44.48	44.50	42.11	44.46	45.94
Ethane	5.49	6.55	5.84	5.94	5.99	5.97	6.07	5.96	6.09
Propane	2.87	4.09	3.37	3.42	3.43	3.34	4.27	3.43	3.45
i-Butane	0.65	0.85	0.74	0.76	0.74	0.73	1.11	0.74	0.72
n-Butane	0.95	1.38	1.16	1.18	1.14	1.11	2.16	1.14	1.11
i-Pentane	0.42	0.49	0.44	0.48	0.45	0.44	0.81	0.46	0.42
n-Pentane	0.46	0.54	0.51	0.56	0.51	0.51	1.17	0.51	0.47
n-Hexane	0.41	0.42	0.41	0.51	0.42	0.45	0.99	0.43	0.38
n-Heptane	0.40	0.39	0.38	0.50	0.38	0.45	0.80	0.39	0.33
n-Octane	0.36	0.43	0.36	0.46	0.35	0.41	0.53	0.34	0.29
n-Nonane	0.33	0.45	0.34	0.38	0.34	0.36	0.34	0.30	0.27
n-Decane	0.30	0.34	0.30	0.32	0.33	0.30	0.29	0.27	0.27
Pseudo1	25.06	16.98	26.36	25.53	22.37	25.13	15.90	25.97	19.61
Pseudo2	2.13	4.36	1.04	1.01	2.82	1.00	3.87	0.12	3.13
Pseudo3	0.41	2.19	0.10	0.10	0.76	0.10	1.85	0.01	1.03
Pseudo4	0.09	1.21	0.02	0.02	0.23	0.02	0.98	0.01	0.38
Pseudo5	0.03	0.70	0.01	0.01	0.08	0.01	0.54	0.01	0.15
Pseudo6	0.01	0.42	0.01	0.01	0.03	0.01	0.31	0.01	0.06
Pseudo7	0.01	0.26	0.01	0.01	0.01	0.01	0.18	0.01	0.03
Pseudo8	0.01	0.41	0.01	0.01	0.01	0.01	0.26	0.01	0.02

Table G.18: Molar mass of the components calculated using the method proposed in this work

	Molar mass (g/mol)								
	1	2	3	4	5	6	7	8	9
Nitrogen	28.01	28.01	28.01	28.01	28.01	28.01	28.01	28.01	28.01
Carbon dioxide	44.01	44.01	44.01	44.01	44.01	44.01	44.01	44.01	44.01
Methane	16.04	16.04	16.04	16.04	16.04	16.04	16.04	16.04	16.04
Ethane	30.07	30.07	30.07	30.07	30.07	30.07	30.07	30.07	30.07
Propane	44.10	44.10	44.10	44.10	44.10	44.10	44.10	44.10	44.10
i-Butane	58.12	58.12	58.12	58.12	58.12	58.12	58.12	58.12	58.12
n-Butane	58.12	58.12	58.12	58.12	58.12	58.12	58.12	58.12	58.12
i-Pentane	72.15	72.15	72.15	72.15	72.15	72.15	72.15	72.15	72.15
n-Pentane	72.15	72.15	72.15	72.15	72.15	72.15	72.15	72.15	72.15
n-Hexane	86.18	86.18	86.18	86.18	86.18	86.18	86.18	86.18	86.18
n-Heptane	100.20	100.20	100.20	100.20	100.20	100.20	100.20	100.20	100.20
n-Octane	114.23	114.23	114.23	114.23	114.23	114.23	114.23	114.23	114.23
n-Nonane	128.26	128.26	128.26	128.26	128.26	128.26	128.26	128.26	128.26
n-Decane	142.28	142.28	142.28	142.28	142.28	142.28	142.28	142.28	142.28
Pseudo1	145.99	145.99	145.99	145.99	145.99	145.99	145.99	145.99	145.99
Pseudo2	161.93	161.93	161.93	161.93	161.93	161.93	161.93	161.93	161.93
Pseudo3	176.09	176.09	176.09	176.09	176.09	176.09	176.09	176.09	176.09
Pseudo4	190.15	190.15	190.15	190.15	190.15	190.15	190.15	190.15	190.15
Pseudo5	204.19	204.19	204.19	204.19	204.19	204.19	204.19	204.19	204.19
Pseudo6	218.21	218.21	218.21	218.21	218.21	218.21	218.21	218.21	218.21
Pseudo7	232.23	232.23	232.23	232.23	232.23	232.23	232.23	232.23	232.23
Pseudo8	255.93	255.93	255.93	255.93	255.93	255.93	255.93	255.93	255.93